Hydrothermal Synthesis of Shape/Size-Controlled Cerium-Based Oxides

By Samuel Itumo Mutinda

Submitted in Partial Fulfillment of the Requirements

For the Degree of

Master of Science in Chemistry

Advisor: Dr. Ruigang Wang

Chemistry Department

Youngstown State University

August, 2013

Signature and Declaration

I hereby release this thesis to the public. I understand that this thesis will be made available from the OhioLINK ETD Center and the Maag Library Circulation Desk for public access. I also authorize the University or other individuals to make copies of this thesis as needed for scholarly research.

Signature:

Samuel Mutinda, Student Date

Approvals:

Dr. Ruigang Wang, Thesis Advisor Date

Dr. Timothy R. Wagner, Committee Member Date

Dr. Sherri Lovelace-Cameron, Committee Member Date

Dr. Sal Sanders, Associate Dean of Graduate Studies Date

ABSTRACT

A low energy band gap between Ce^{3+} and Ce^{4+} states in cerium oxide along with its high oxygen mobility and high oxygen storage capacity are properties that qualify it as one of the most widely used heterogeneous catalysts and catalyst oxide supports. This thesis report is an account of studies that were carried out on the synthesis and catalytic properties of pure, metal-doped and noble-metal impregnated cerium oxide nanoparticles.

Our results revealed that synthesis temperature, during hydrothermal reactions, plays a critical role in controlling the shape, size, oxygen vacancy concentration, and low temperature reducibility in CeO_2 nanoparticles. In addition, OH^- ion concentration was found to play an important role in engineering the lattice constants and oxygen vacancy concentrations of ceria nanoparticles within the same particle morphology and synthesis temperature.

Secondly, our studies demonstrated that hydrothermal synthesis is a facile one-step approach to the preparation of compositionally homogeneous $Ce_xZr_{1-x}O_2$ ($0 \leq x \leq 1$) nanocrystals, in which CeO_2-ZrO_2 mixed oxides present a superior low-temperature oxygen release capability compared to pure CeO_2. The $Ce_{0.5}Zr_{0.5}O_2$ system proved to have good thermal stability up to 1000^oC under reducing and oxidizing atmosphere. We have also seen that at above 1000^oC, phase transformation occurs from psudocubic to cation ordered pyrochlore or tetragonal phase under reducing and oxidizing atmosphere, respectively. This method may be easily extended to other cerium-based mixed oxides or synthesis of analogous mixed oxides.

Lastly, our results established that the impregnation of 1 wt. % platinum and gold on CeO_2 nanorods and on nanocubes causes an enhanced reduction on their surface

reduction temperatures with negligible effect on their bulk reducibility. It was also shown that both pure and impregnated CeO_2 nanorods have a lower surface reduction temperature compared to that of pure and impregnated CeO_2 nanocubes. We have also demonstrated that gold nanoparticles proved to have a higher catalytic performance in oxidizing molecular hydrogen at low temperatures as compared to platinum nanoparticles.

ACKNOWLEDGEMENTS

I would first like to thank my thesis advisor Dr. Wang for his immeasurable patience and mentorship on me. I especially want to thank him for helping me realize that I have the potential to execute high notch research assignments in nanotechnology, and for allowing me to learn from his as much as I could. I will never forget the many times that both of us sat in his office to discuss on our research results and publications. This was an intriguing experience for me particularly because I was able to learn numerous characterization techniques in material science and engineering.

I would like to thank my committee members Dr. Timothy R. Wagner and Dr. Sherri Lovelace-Cameron for their time and valuable suggestions on my thesis, and Ray Hoff and Dr. Dingqiang Li for his help on instrument usages.

I also want to thank Dr. Allen Hunter, Dr. Matthias Zeller, Shadrack Mule, Aemable Ngendahimana and Dr. Lovelace-Cameron for facilitating my admission to YSU. in 2011. In this regard, I also want to thank the YSU graduate school for offering financial support to me during my stay at YSU.

I also want to thank Jacob Chevlen and Beth Roach for their helpful critique and suggestions in the writing this thesis. Lastly, I want to acknowledge my research group mates and everybody else that contributed positively to the success of this report.

Table of Contents

List of figures

Chapter 1

Chapter 2

Chapter 3

Chapter 4

Chapter 5

Chapter 1 Introduction

1.1 Project Background

Cerium is a rare earth metal that is soft, silvery, and ductile. It easily oxidizes in air to form ceria (CeO_{2-X}) that may assume a yellow to white color depending on its particle size, and morphology. Reportedly, cerium accounts for about 0.0046% of the Earth's Crust by weight, hence qualifying cerium oxide or ceria as the most abundant rare earth metal oxide. Ceria crystalizes in a face centered cubic (FCC) structure with a space group of Fm-3m, shown in Figure 1, and has a lattice constant of 5.410 Å at room temperature. It is insoluble in water, moderately soluble in strong mineral acids, and it is slightly hygroscopic and able to absorb low amounts of moisture and CO_2 from the atmosphere. Stoichiometric cerium (IV) oxide has a molar mass of 172.11 g and a density of 7.65 g/cm^3. It is odorless and melts and boils at 2500 ^oC and 3500 ^oC respectively [1-5].

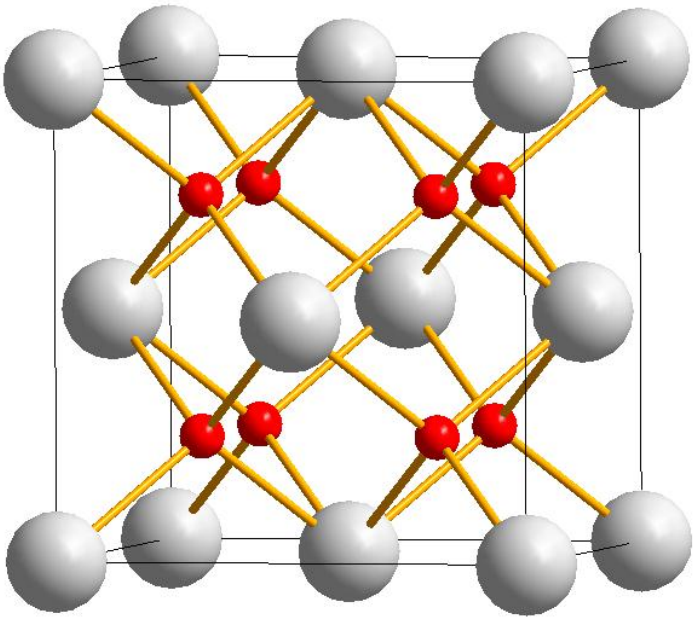

Figure 1: Unit cell of CeO_2. White and red balls represent cerium and oxygen atoms respectively.

In the recent past, ceria has received much attention in the field of material science and engineering due to its excellent electronic and catalytic properties. On a practical basis, ceria is found to have unique properties in ultraviolet radiation absorbing ability, high temperature stability and high hardness index hence becoming of great use in applications such as glass polishing, solid ionic conductors, gas sensors, ultraviolet radiation screening, semiconductors and most importantly in oxygen storage materials [1-5].

These excellent properties emerge from the fact that the ionic and charge ratio between Ce^{4+} and O^{2-} ions allow for changes in the CeO_{2-x} structure in such a way that X could vary between 0-0.5 depending on the partial pressure of oxygen. Stoichiometric CeO_{2-x} could be reduced to an unstable $CeO_{1.5}$ formula while still retaining the cubic fluorite structure in a highly reducing atmosphere and then re-oxidize back to stoichiometric CeO_{2-x} in oxidizing conditions. These electronic transitions occur with ease because each transition requires only a single electron [1-5]. The redox functionality of ceria is therefore well founded on the fact that Ce^{4+} ions could easily be converted to Ce^{3+} and vice vasa with reasonably low potential energy barriers. Theoretical simulations have indicated that a simultaneous condensation of two electrons into the localized f-level orbitals of two cerium (IV) ions can occur hence rapidly reducing those Ce^{4+} to Ce^{3+} ions. This condensation in essence favors the structural transformations of Ce (IV) oxide to Ce(III) oxide through the gamma-alpha isosructural transitions in which the volume of the unit cell of ceria suddenly shrinks at a given specific critical oxygen partial pressure so that the reduction process can occur while simultaneously retaining a FCC structure. According to theoretical physics, this lattice shrinking occurs in such a way that the alpha

phase the 4f states become parts of the conduction band. In a typical oxygen vacancy formation process, an oxygen ion transfers its two p-orbital electrons to a pair of electron deficient Ce^{4+} ions before it exits the unit cell as shown in Figure 2 [1-6].

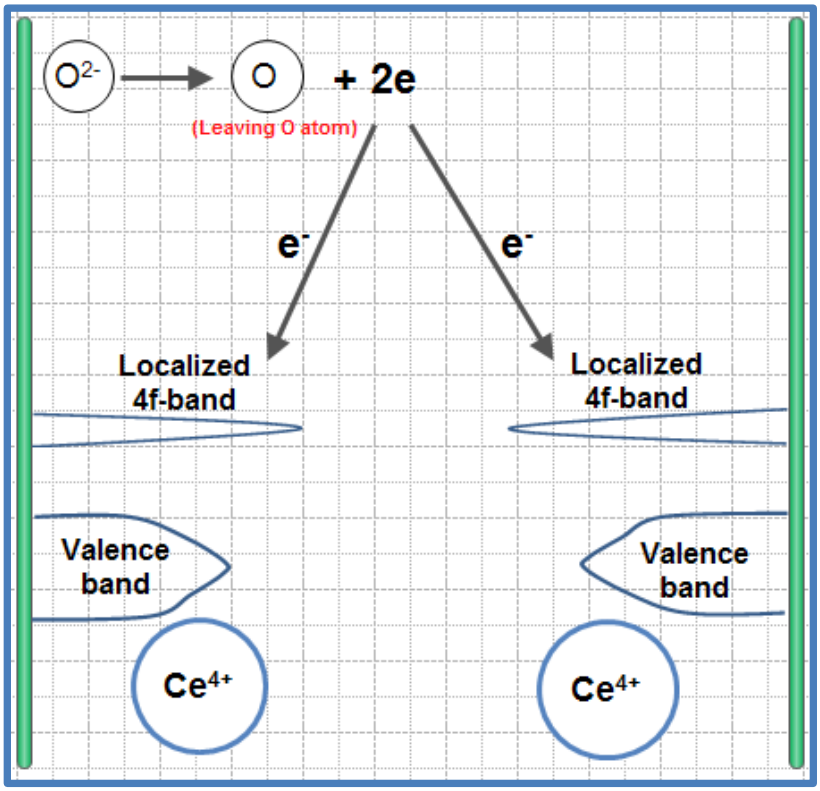

Figure 2: Oxygen vacancy formation process. The leaving oxygen atom donates its valence electrons to two Ce^{4+} ions, hence converting them to Ce^{3+} ions.

The reversibility of the above outlined process constitutes the oxygen storage capacity of cerium oxide as shown in Figure 3 below. As mentioned before, this process occurs with ease; specifically as only one electron is needed to participate in the process. Theoretical calculations have reported that ceria band gaps could go as low as close to 2.5 eV implying that this process encounters very low potential energy barriers [6-8].

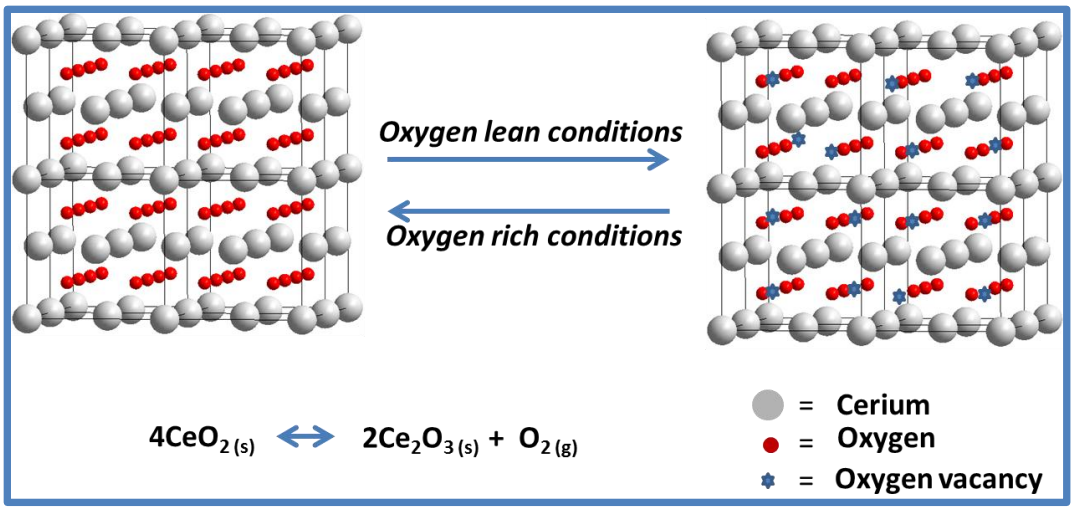

Figure 3: Redox functionality of CeO_2. Used here are 2 ×2 × 2 unit cells for CeO_2.

The increasing need for a global green economy in the energy and transportation sectors have progressively necessitated the enforcement of strict environmental regulations that are geared towards the reduction of greenhouse effects, hence requiring the use of modern technologies and devices that efficiently lower the levels of pollutant gases and/or convert them to environmentally harmless products . One of the ways of controlling pollution in the transportation sector is by installing vehicle emission control devices such as the three-way catalytic convertors on automobiles in order to rapidly convert CO and C_xH_y to H_2O and CO_2 while at the same time reducing NO_x to molecular nitrogen in highly fluctuating emission concentrations. Figure 4 below is a schematic of how a commercial automobile catalytic convertor works [1-8].

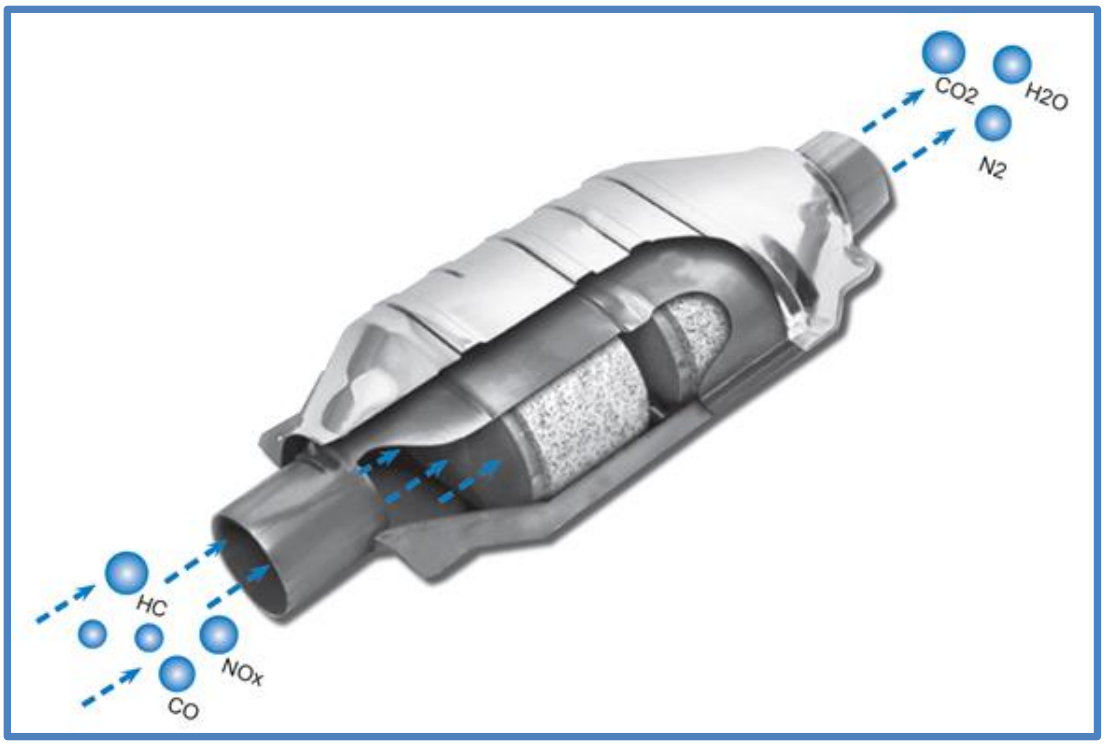

Figure 4: Commercial catalytic convertor. (Schematic derived from http://www.thecleanaircompany.co.nz/catalytic-xhausts/Catalytic_Converters_Direct_Fit.html)

The concentration of oxygen vacancies in the ceria lattice plays a very critical role in controlling diffusion rate and mobility of oxygen ions in the lattice. This therefore means that the concentration of oxygen ions in cerium oxide nanocrystals has a direct correlation with the oxygen storage capacity of the materials. The number of oxygen vacancies increases in ceria therefore increases with the ease at which oxygen can move within the lattice, hence allowing the ceria to reduce and oxidize molecules or co-catalysts on its surface. Studies have indicated that the catalytic activity of ceria is directly related to the number of oxygen vacancies in the crystal. In addition, due to the redox functionality of ceria, it can also be used as a co-catalyst or oxide support in several other reactions, such as the water-gas shift and steam reforming of ethanol or diesel fuel into hydrogen gas and carbon dioxide [1-8].

The redox functionality of CeO_2 and its ability to act as an oxygen storage material, however, is constrained to a narrow range of temperatures (~ 400-800 ^oC) in the absence of metal dopants or noble metal catalysts and its performance drastically reduces at temperatures below 300 ^oC due to lack to sufficient thermal energy to reduce oxygen ions from the ceria lattice [3-5]. In the present work, we have studied the effect of impregnating gold and platinum on different morphologies and sizes of CeO_2 and compared the performance of the two noble metals on the different morphologies of ceria, with more emphasis on low temperature reducibility and catalytic activity of the materials.

In order gain a deeper understanding on how engineering of oxygen vacancies and defects on the lattice structure of ceria, this thesis report addresses the synthesis and characterization of pure ceria nanocrystals with emphasis on morphology control. Thereafter, the catalytic effect of doping cerium oxide with other metals is studies using $Ce_{1-x}Zr_xO_2$ system as a case study. Here, synthesis parameters such as the effect of mechanical stirring (during synthesis) on morphology and size of the resulting nanocrystals were also of great concern. Lastly, the catalytic effect and synergism that comes as a result of using (size and morphology controlled) ceria nanocrystals with other catalysts such as gold and platinum was studied in depth. The last two studies showed in that there was improved catalytic performance of cerium oxide nanocrystals as a result of increased oxygen mobility, oxygen vacancies. As it will be discussed later, $Ce_{1-x}Zr_xO_2$ system proved to have better thermal stability and catalytic activity as compared to pure CeO_2. In addition, we also found that gold nanoparticles gave better catalytic performance as compared to platinum nanoparticles.

1.2 References

1. Bera, P. et al., *J. Phys. Chem. B.* **107**, 6122 (2003)
2. Agarwal, S., Lefferts, L., Mojet, B. L., *ChemCatChem*. **5**, 479 (2013)
3. Pinjari, D.V. et al., *Ultrason. Sonochem.* **18**, 1118 (2011)
4. Zhang, J. et al., *Nano Lett*. **11**,361 (2011)
5. Wenjuan, S., Hongjuan, G., Chang, L., Xiaonan, W., *J. Rare Earths*. **30**, [7] 665(2012)
6. Skorodumova, N.V. et al., *Physic. Rev. Lett*. **89**, 166601-3 (2002)
7. Goldsby, J. C., *J. Ceram*. **323018**, 1 (2013)
8. Lin, K.-S., Chowdhury, S., *Int. J. Mol. Sci*. **11**, 3226 (2010)

Chapter 2 Synthesis and Experimental Techniques

In this study, a one-pot hydrothermal technique was used to synthesize nanoparticles of pure CeO_2, Ce_{1-x} Zr_xO_2 solid solutions and Pt and Au impregnated CeO_2 nanocomposites. In this chapter therefore, hydrothermal technique is discussed first with emphasis on how different reaction parameters were affected by synthesis temperature. Secondly, the chemical reagents and synthesis procedures that were employed in the study are discussed. Lastly, characterization techniques that were employed in the study are presented.

2.1 Hydrothermal synthesis technique

Hydrothermal technique is a high temperature synthesis method in which aqueous reactants are allowed to react under "low" temperature and high pressure in a Teflon lined autoclave. It is one of the most effective ways of synthesizing morphologically controlled nanoparticles of high purity, high dispersion and narrow size distribution. As documented in literature, crystal nucleation and growth in hydrothermal reactions is primarily a function of the reaction temperature and pressure although other factors such as the choice of solvent or concentration of the precursor reactants also play a big role. The main advantage of this method is the ability to control particle size and shape of the nanoparticles by applying different reaction parameters. The main disadvantage of using this method however is the fact that acquisition of the required equipment such as autoclaves and a high temperature temperature-programmed box furnace is expensive in addition to the fact that reactions cannot be performed as quickly compared to other synthesis techniques such as chemical precipitation or thermal decomposition of metal

precursor salts. Figure 1 below shows the equipment needed to perform hydrothermal reactions [1-6].

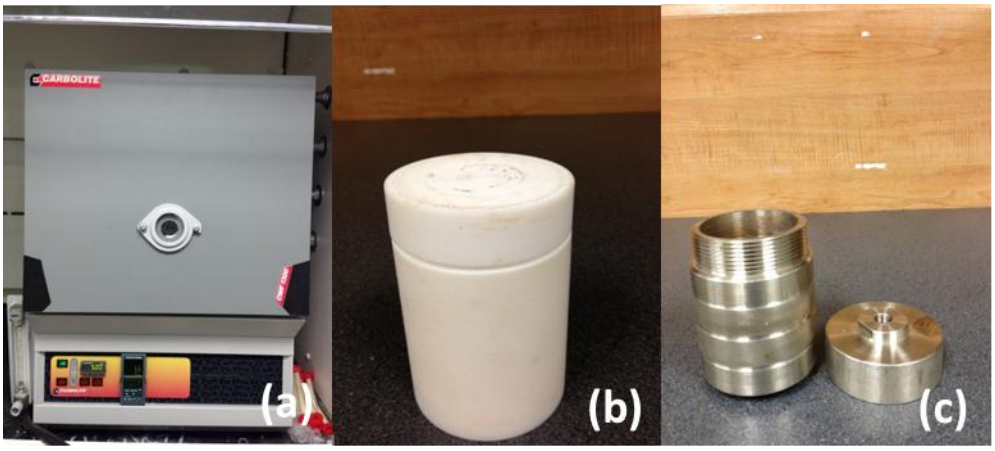

Figure 5: (a) Programmable box furnace (b) Teflon cup (c) Stainless steel Autoclave vessel

Given that synthesis temperature and reaction mixture volume (with respect to the total autoclave volume) are most important parameters in hydrothermal reactions, it was sought to understand how the volume of the solvent (water) varied/expanded with synthesis temperature during synthesis. Equation 1 below was used to show how solvent thermal expansion varied with reaction temperature.

$$\boldsymbol{dV = V_f - V_i = V_i\beta(T_f - T_i)} \quad \ldots\ldots \mathbf{1}$$

$where: dV = Change\ in\ solvent\ volume$

$V_f = final\ volume$

$V_i = initial\ volume$

$T_f = final\ temperature$

$T_i = initial\ temperature$

$\beta = volumetric\ temperature\ coefficient\ (1/^{o}C)$

In addition, considering that the expansion of any substance causes a decrease in its density, we also sought to understand how solvent density changed with increasing temperature during synthesis and. Equation 2 below was used to carry out the calculations.

$$\boldsymbol{\rho_f = \rho_i / [1 + \beta(T_f - T_i)]} \quad \ldots\ldots\ldots\ldots\ldots\ldots\ldots\ldots\ldots\ldots\ldots\ldots\ldots\ldots\ldots\ldots\ldots\ldots\ldots\ldots\ldots\ldots\ldots\ldots . \mathbf{2}$$

$where: \rho_f = final\ density$

$\rho_i = initial\ density$

$T_f = final\ temperature$

$T_i = initial\ temperature$

$\beta = volumetric\ temperature\ coefficient\ (1/^oC)$

During this study, all reaction mixtures ($Ce(NO_3)_3$ + NaOH solutions) were maintained at a volume of 120 mL with all the reactions being carried out in 200 mL autoclaves. Putting this into consideration, Equations 1 & 2 above were used to model how density and volume changes varied with synthesis temperatures that varied from 50 ^oC to 250 ^oC with an interval of 40 ^oC. Table 1 is a summary of the calculations. As can be seen from the calculated figures, solvent density decreases with increasing synthesis temperature while volume expansion increases as temperature is increased.

Table 1: Relationship between solvent volume expansion and change in its density

ρ_i (g/mL)	V_i (mL)	T_i (^oC)	β	T_f (^oC)	dV (mL)	V_f (mL)	ρ_f (g/mL)
0.99823	120	20	0.000214	50	0.7704	120.7704	0.991862
0.99823	120	20	0.000214	90	1.7976	121.7976	0.983497
0.99823	120	20	0.000214	130	2.8248	122.8248	0.975272
0.99823	120	20	0.000214	170	3.852	123.852	0.967183
0.99823	120	20	0.000214	210	4.8792	124.8792	0.959228
0.99823	120	20	0.000214	250	5.9064	125.9064	0.951402

Determining how the solvent expanded as a function of temperature was important in calculating the pressure of the air that was trapped in the autoclaves during synthesis, considering that only 60% of the autoclaves' volume was used each time, leaving the rest of the space occupied by air. At low temperatures i.e 50 ^oC and 90 ^oC, the vapor pressure of the solvent was found to be less than that of the compressed air, making it hard for the solvent to boil or reach its critical vaporization point. However, from 130 ^oC and above, the pressure of the compressed air was calculated to be lower than that of the reaction solvent, hence the internal pressure of the autoclaves was assumed to be equivalent to the vapor pressure of water at those temperatures. Equation 3 below was used to calculate the pressure of the enclosed air at the different synthesis temperatures as summarized in Table 2 below:

$$\frac{\boldsymbol{P_1V_1}}{\boldsymbol{T_1}} = \frac{\boldsymbol{P_2V_2}}{\boldsymbol{T_2}} \quad \textbf{3}$$

$where: P_1 = \ initial\ pressure$

$P_2 = \ final\ pressure$

$V_1 = \ initial\ volume$

$V_2 = final\ volume$

$T_1 = Initial\ temperature$

$T_2 = Final\ temperature$

Table 2: Relationship between temperature, volume and pressure of compressed air

P_1 (atm)	V_1 (mL)	T_1 (K)	V_2 (mL)	T_2 (K)	P_2 (atm)	P_2 (MPa)
1	80	293	79.2296	323	1.113108	0.1128
1	80	293	78.2024	363	1.267386	0.1284
1	80	293	77.1752	403	1.425771	0.1444
1	80	293	76.148	443	1.588428	0.1609
1	80	293	75.1208	483	1.755534	0.1779
1	80	293	74.0936	523	1.927274	0.1953

Clausius Clapeyron equation was then used to calculate the vapor pressure of the solvent at different temperatures as shown in Table 3 below [7-8]:-

$$\boldsymbol{ln\frac{P_2}{P_1} = \frac{\Delta H_{vap}}{R}\left(\frac{1}{T_1} - \frac{1}{T_2}\right)} \dots\dots\dots\dots\dots\dots\dots\dots\dots\dots\dots\dots\dots\dots\dots\dots\dots\dots\dots\dots\dots\dots\dots\dots\dots .. \boldsymbol{4}$$

$where: P_1 = initial\ pressure$

$P_2 = final\ pressure$

$\Delta H_{vap} = enthalpy\ of\ vaporization\ of\ water = 44000\ Jmol^{-1}$

$T_1 = initial\ temperature$

$T_2 = final\ temperature$

$R = Gas\ constant$

Table 3: Relationship between temperature and the vapor pressure of the solvent

ΔH_{vap} (Jmol^{-1})	R (J/mole.K)	T_1 (K)	T_2 (K)	$1/T_1$ (K^{-1})	$1/T_2$ (K^{-1})	P_1 (mmHg)	P_2 (mmHg)	P_2 (MPa)
44000	8.3145	293	323	0.003413	0.003096	17.5	93.66463	0.0125
44000	8.3145	293	363	0.003413	0.002755	17.5	569.6918	0.0760
44000	8.3145	373	403	0.002681	0.002481	760	2185.204	0.2913
44000	8.3145	373	443	0.002681	0.002257	760	7151.984	0.9535
44000	8.3145	373	483	0.002681	0.00207	760	19234.09	2.5643
44000	8.3145	373	523	0.002681	0.001912	760	44462.8	5.9278

Figure 2 below is a graphical interpretation of the above discussed four hydrothermal reaction parameters and how they are related to each other. From the schematic, it is clear that solvent volume expansion and vapor pressure increased sharply with increasing temperature. It is also clear that at 50 ^{o}C and 90 ^{o}C, the compressed air pressure dominates the vapor pressure of the solvent, meaning that the solvent exclusively remains in its liquid form throughout the reactions while at higher temperatures the solvent vapor pressure is dominant.

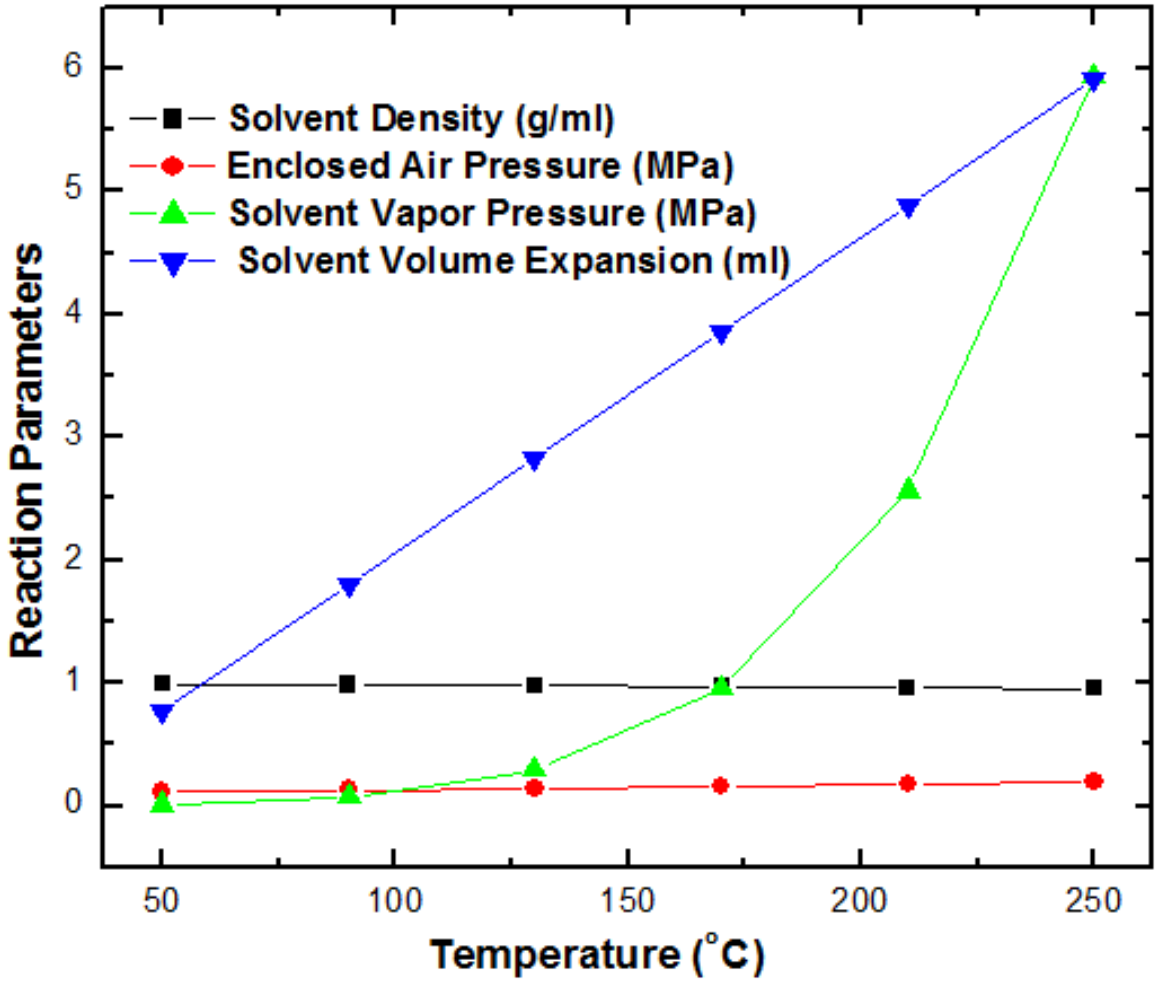

Figure 6: Variation of hydrothermal reaction parameters with temperature.

2.1.1 Experimental details

2.1.1.1 Hydrothermal synthesis of pure ceria nanoshapes

In this study, 0.1 M $Ce(NO_3)_3$ and 6 M NaOH were used as the Ce^{3+} ion and OH^- ion precursors respectively in all reactions that were performed towards synthesis of pure CeO_2. Constant stock solution concentrations and total reactant mixture volume were maintained throughout the study in order to be able to probe the effect of synthesis temperature on the size, shape and crystallinity of CeO_2 nanoparticles. All samples were synthesized using hydrothermal technique that was believed to occur in two major steps [8]

$$\boldsymbol{Ce(NO_3)_3(aq) + 3NaOH(aq) \rightarrow Ce(OH)_3(s) + 3NaNO_3(aq)} \quad \text{5}$$

$$\boldsymbol{4Ce(OH)_3(s) + O_2 \rightarrow 4CeO_2(s) + 6H_2O(l)} \quad \text{6}$$

The schematic, as shown in Figure 3 is a summary of how pure CeO_2 nanoparticles were synthesized. More details on synthesis and characterization of CeO_2 will be given in Chapter 3.

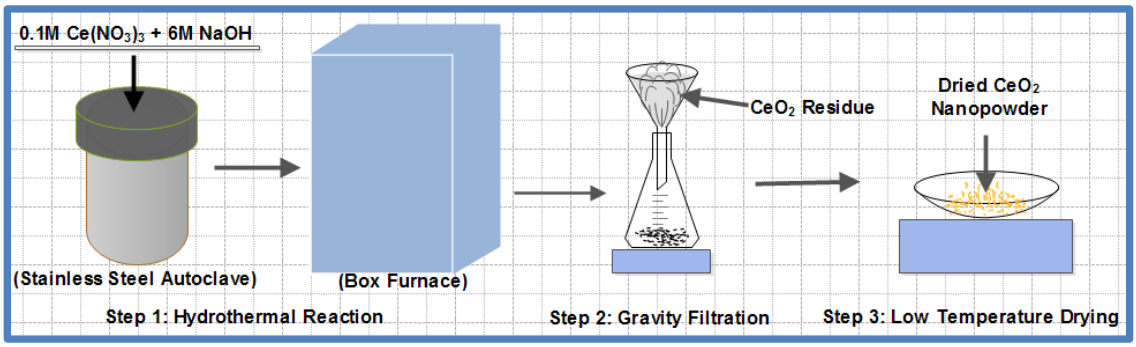

Figure 7: Steps involved in hydrothermal synthesis of pure CeO_2.

2.1.1.2 Precipitation assisted hydrothermal synthesis of $Ce_{1-x}Zr_xO_2$ solid solutions

By definition, chemical precipitation is the formation of a solid from a solution that occurs from a reaction between two or more soluble precursor reactants. In a typical

setup, a solid product separates out of an aqueous reaction mixture that contains soluble or suspended salts. This method enjoys the benefits of low temperature and low pressure nanoparticle nucleation and uniform particle growth and aging. The technique is relatively inexpensive and the reaction occurs fast as compared to other methods. The two main advantages of using precipitation over other methods is its capability to achieve very small particle sizes i.e. 1-5 nm and the fact that real time physical aspects of the reaction such as color changes or temperature can be monitored. On the other side, its main disadvantage is that the process of controlling morphology or particle dispersion is a big challenge because particle nucleation occurs very fast due to reasons that are attributable to reaction kinetics [9-12].

Ceria-zirconia solid solutions were synthesized using a precipitation assisted hydrothermal technique where specific volumes of $Ce(NO_3)_3$, $Zr(NO_3)_4$ and NaOH were mixed and vigorously stirred for 40 minutes before performing hydrothermal reaction at 150 ^oC for 48 hrs, shown in Figure 4. Stirring was done in order to increase crystal homogeneity and randomize the positions of zirconium ions in the crystal lattice of lattice. Different weight percentage of Zr was incorporated into ceria lattice in order to perform an extensive systematic study on the catalytic performance of such systems.

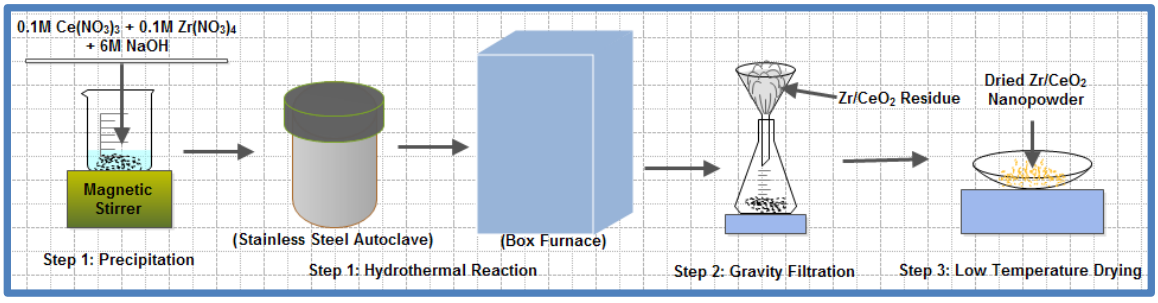

Figure 8: Steps involved in precipitation assisted hydrothermal synthesis of $Ce_{1-x}Zr_xO_2$ solid solutions

2.1.1.3 Hydrothermal synthesis of CeO_2 nanoshapes and the impregnation of noble metal catalysts

Different shapes of cerium oxide nanoparticles were synthesized using hydrothermal synthesis at two different temperatures and thereafter loaded with 1 wt. % platinum and gold nanocatalysts as shown in the schematic below in Figure 5. During impregnation process, all the noble metal solution solvent was evaporated at around 70 ^{o}C with constant stirring instead of filtering it in order to retain all noble metal ions in the cerium oxide nanosupport. More details will be presented in Chapter 5.

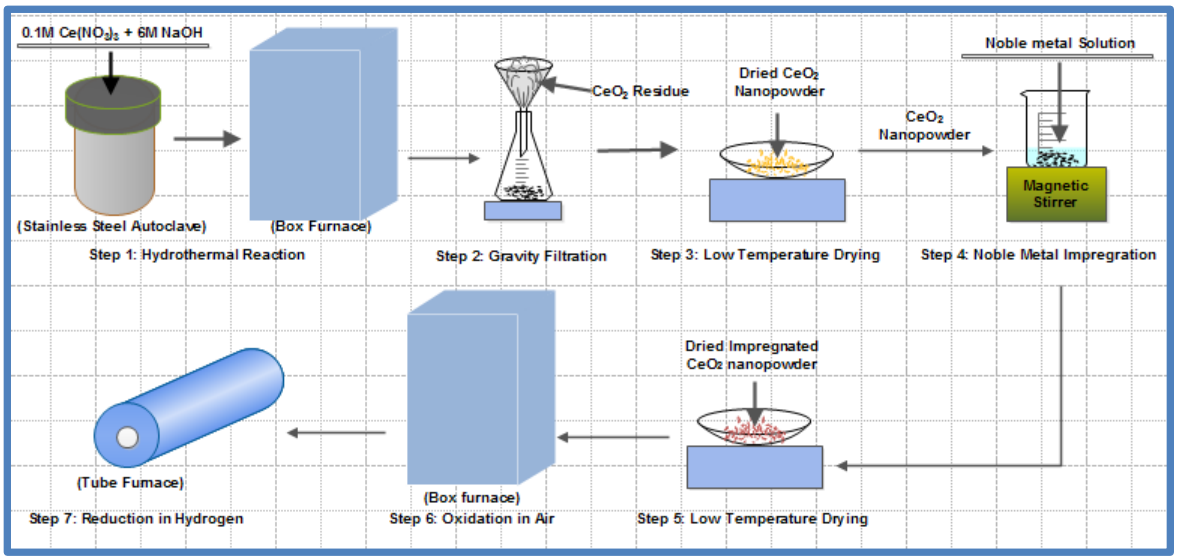

Figure 9: Steps involved in hydrothermal synthesis of CeO_2 nanoparticles and impregnation of noble metal nanocatalysts on the ceria nanosupport.

2.2 Characterization Techniques

Characterization techniques that were employed in this research included Powder X-ray Diffraction, Raman Spectroscopy, Transmission Electron Microscopy, BET-Surface Area analysis and Temperature Programmed Reduction. Below is a detailed description of these techniques.

2.2.1 Powder XRD

Powder X-ray diffraction (XRD) is an important technique that is applied in phase identification of crystalline solids and provides information about the unit cell of that material and its average particle size. An X-ray diffractometer basically consists of an X-ray tube, a sample holder, and an X-ray detector. X-rays are generated using a cathode ray tube in which a heated filament produces electrons that are then accelerated toward a metal target by applying a high voltage, such that the target is bombarded with electrons in order to produce X-rays. The produced X-rays are then collimated and directed towards the sample that sits on a rotating stage. The detector is also rotated such that constructive interference of the diffracted X-rays occurs at angles where the geometry between the sample and detector satisfies the Bragg equation. Whenever this condition is met, the detector records the signal while an attached computer converts it to a peak. During data processing and interpretation, the average crystallite size of the solid sample is approximated using the Scherrer`s equation that can be written as [1-18]:

$$\boldsymbol{d_{hkl}} = {}^{\boldsymbol{K\lambda}}/_{\boldsymbol{\beta_{hkl}\cos\Theta}} \ldots\ldots\ldots\ldots\ldots\ldots\ldots\ldots\ldots\ldots\ldots\ldots\ldots\ldots\ldots\ldots\ldots\ldots\ldots\ldots\ldots\ldots\ldots\ldots\ldots\ldots\ldots\ldots \mathbf{7}$$

$where\ d_{hkl} = d\ spacing$

$K = a\ constant\ related\ to\ the\ particle\ size\ and\ line\ indicies = 0.9$

$\lambda = wavelength\ of\ the\ incident\ X - rays$

$\beta_{hkl} = diffraction\ line\ width$

$\Theta = diffraction\ angle$

As far as this research is concerned, powder X-ray diffraction (XRD) analyses were done using the Rigaku Miniflex II Desktop X-ray Diffractometer applying a scanning range of 10^o to 90^o (2θ), and a sampling width of 0.020 with a scanning speed of

0.5 ^{o}/min. Data processing was then carried out using Jade software. Figure 6 below is a picture of the Rigaku Miniflex II Desktop X-ray Diffractometer.

Figure 6: Rigaku Miniflex II Desktop X-ray Diffractometer.

2.2.2 Raman spectroscopy

Raman spectrometry is a technique that is well founded on the inelastic scattering of light where an analyte sample is irradiated with intense monochromatic laser light after which the scattered light is analyzed for frequency shifts. The intensity of the scattered light is usually proportional to the amount of material present, therefore making it possible to perform both qualitative and quantitative measurements. The method is non-destructive hence making it ideal for investigating the physical properties of materials such as crystallinity, phase transitions and polymorphs. Raman spectroscopy usually operates at a wavelength that is independent of the vibrational modes of a sample and since the method measures the shift in frequency from that of the incident laser, it can be

used within a very wide range of frequencies. This makes Raman spectroscopy ideal for the study of inorganic materials that have vibrational frequencies in the far-infrared that are otherwise difficult to reach [18].

Raman spectra were obtained at room temperature using a Kaiser Optical Systems RXNI-785 that was equipped with a thermoelectrically cooled diode laser source that fluorescenced at a wavelength of 785 nm and a power of 400 mW. The spectrometer also was equipped with a CCD detector that was maintained at -40 ^{o}C in order to lower its background levels. The exposure time during data collection was adjusted according to the intensity of the Raman scattering. Figure 7 below is a picture of the Kaiser Optical Systems RXNI-785 Spectrometer.

Figure 7: Kaiser Optical Systems RXNI-785 Spectrometer.

2.2.3 Transmission Electron Microscopy

Transmission electron microscopy is a high end scientific imaging technique that uses a high energy beam of electrons to image objects on a very fine scale. The technique can

be used to give information about the topography (surface features), morphology (shape and size), composition (both qualitative and quantitative) and crystallographic information. Morphology characterization was an especially important aspect of this research, given that different synthesis techniques would lead to different particle shapes and sizes. Other information obtained from this technique was found important in fully understanding the correlation between particle dispersion and agglomeration and BET surface area analysis results that will be discussed elsewhere in this report. A JEOL2100 instrument that was equipped with an EDAX detector and an annular dark-field detector was used to collect microscopy data at an acceleration voltage of 200 kV. In a typical sample preparation procedure, the freshly prepared CeO_2 precipitate was lightly agitated for 30 seconds (while still in the Teflon cup) using a stirring rod in order to uniformly disperse the nanoparticles within the reaction solvent (H_2O). Immediately afterwards a holey carbon grid was dipped into the reaction mixture for two seconds before it was removed. Figure 8 below is a picture of the JEOL2100 TEM.

Figure 8: JEOL 2100 TEM Instrument.

2.2.4 Brunauer-Emmett-Teller (BET) Surface Area Analysis

The surface area of a catalyst is an important physical parameter that can determine its activity and stability. The most widely used technique for determining a material`s surface area, and also the one that was used in this research, is the BET method, where a material`s surface area is measured as a function of its ability to physi-adsorb gas molecules. In this work, BET surface area analyses were performed on a Micromeritics AutoChem^{TM} II 2920 where dry CeO_2 nanopowders were analyzed using liquid nitrogen gas at -196 ^{o}C. It is worthy to mention that the nanopowders were first degassed at 110 ^{o}C

for one hour before the measurements were carried out. Figure 9 below is a picture of the Micromeritics AutoChem™ II 2920.

Figure 9: Micromeritics AutoChem™ II 2920.

2.2.5 Temperature-Programmed Reduction (TPR)

Temperature-programmed reduction (TPR) is a method that is used in the fields of homogeneous and heterogeneous catalysts where optimization of the reduction conditions for a catalyst is investigated. TPR measurements were also carried out on a Micromeritics AutoChem™ II 2920 using 5% H_2 in Argon, from room temperature to 900 ^{o}C at a ramp rate of 10 ^{o}C per minute. All samples were also degassed at 110 ^{o}C for one hour before analyses were carried out.

2.3 References

1. Mai, H.X., et al., *J. Phys. Chem. B.* **109**, 24380 (2005)
2. Zhou, X. D., Huebner, W., Angerson, H. U., *Chem. Mater*. **12**, 378 (2003)
3. Masui, T., Hirai, H., Imanaka, N., Adachi, G., *J. Mater. Sci. Lett*. **21**, 489 (2002)
4. Tok, A.I.Y., Du, S.W., Boey, F.Y.C., Chong, W.K., *Mater. Sci. Eng., A*. **466**, 223 (2007)
5. Pan, C., Zhang, D., Shi, L., *J. Solid State Chem*. **181**, 1298 (2008)
6. Pan, C., Zhang, D., Shi, L., Fang, J., *Eur. J. Inorg. Chem*. **2429** (2008)
7. Tseng, C.H.T., et al., *Int. J. Adv. Manuf. Technol*. **64**, 579 (2013)
8. Izu, N. et al., *J. Ceram. Soc. Jpn.* **114**, [5] 418 (2006)
9. Zhou, X.-D, Huebner, W., Anderson, H.U., *Appl. Phys. Lett*. **80**, 3814 (2002)
10. Chen, Huey-Ing, Chang, Hung-Yi., *Ceram. Int.* **31**, 795 (2005)
11. Mohapatra, M., Anand, S., *Int. J. Engin, Sci. & Technol*. **2**, [8] 127 (2010)
12. Chen, H.I., Chang, H.Y., *Solid State Commun*. **133**, 593 (2005)
13. Chang, H.Y., Chen, H.I., *J. Cryst. Growth*. **283**, 457 (2005)
14. Chen, L., et al., *J. Phys. Chem. C.* **114**, 12909 (2010)
15. Pinjari, D. V., Pandit, A. B., *Ultrason. Sonochem.***18**, 118 (2011)
16. Lannone, M., *J. Chem. Edu*. **83**, [1] 97 (2006)
17. Miyamoto, T., Okano, S., Kasai, N., *Appl. Environ. Microbiol.* **75**, [15] 5058 (2009)
18. Chowdhury, M. B.I., Hossain, M. M., Charpentier, P. A., *Appl. Catal. A.: Gen.* **405**, 84 (2011)

Chapter 3 Synthesis and Characterization of Pure Ceria

3.1 Introduction

Ceria (CeO_2) based materials are considered important in the chemical industry due to their applications in optical films, polishing materials, gas sensors, fuel cells and more importantly in the field of catalysis. Ceria is one of the extensively used catalysts in the three way catalytic converters where combustion engine exhaust gases, such as CO, NO, H_xC_y, are efficiently converted to environmentally friendly gases [1 –5]. Bulk pure ceria however suffers from low thermal stability at high temperatures (e.g. >800^oC) and lower catalytic performance at low temperatures (e.g <400^oC). Doping of CeO_2 with various metal oxides therefore (e.g. praseodymium or zirconium or titanium-based oxides), have proven to generate metal oxide solid solutions that have higher thermal stability and low-temperature redox functionality or oxygen capacity [6], [7]. For example, nano-sized cerium based mixed oxides, such as $Ce_{1-x}Pr_xO_2$, $Ce_{1-x}Zr_xO_2$, and $Ce_{1-x}Ti_xO_2$, have higher catalytic performance as compared to pure cerium oxide nanoparticles; their high catalytic performance is in general agreeably attributed to their enhanced thermal stability and easier formation of oxygen vacancies in the CeO_2 cubic fluorite structure, hence leading to a higher oxygen ion mobility within the lattice structure [1-7]. Synthesis of unique morphologies of ceria at the nanoscale level has also proven to enhance the oxygen storage capacity and low-temperature activity of CeO_2 in particular nanoshapes. This observation has been attributed to the fact that different nanoshapes usually have different crystallographic facets that correspond to different oxygen vacancy formation energies on surface and in the lattice and of ceria nanoparticles. Owing to these disparities, understanding the consequences of morphology on the low-temperature activity and oxygen storage capacity of CeO_2 has been of major

concern in material science and engineering [1-10]. This chapter reports on a systematic study that was conducted on synthesis and characterization of CeO_2 nanorods and nanocubes through a facile hydrothermal method with key attention focused on understanding how variations on synthesis temperature and OH^- ion concentration influenced the morphology, size, low-temperature reducibility and the oxygen storage capacity of the nanoparticles.

3.2 Experimental

CeO_2 nanorods and nanocubes were synthesized using a facile hydrothermal method at different temperatures using $Ce(NO_3)_3$ as the Ce^{3+} precursor and NaOH as the base. In a typical setting, ceria nanoparticles were synthesized on a temperature range of range of 50 ^oC to 250 ^oC with intervals of 40 ^oC; a set of three different reactions were performed at each temperature as summarized in Table 1. All the reactions were performed in a box furnace that had been programmed to operate at a ramp rate of 10 ^oC/min with a dwell time of 48 hours. After the hydrothermal reactions had been carried out at the appropriate temperatures, the CeO_2 precipitates were recovered by gravity filtration and washed thoroughly using distilled water and absolute ethanol followed by low-temperature drying (~50 ^oC) in a box furnace for 24 hours. The samples were then crushed into fine powders and then exposed to different analysis techniques.

Table 1: Reaction details for a set of reactions that were performed at each temperature

	Reaction mixture contents					**Mole Rations**
Reaction identity	0.1M $Ce(NO_3)_3$	6M NaOH	Total volume	Moles of $Ce(NO_3)_3$	Moles of NaOH	Ce : OH
a	12.8 mL	1.2 mL	14 mL	0.00128	0.0072	8:45
b	11.6 mL	2.4 mL	14 mL	0.00116	0.0144	10:124
c	10.4 mL	3.6 mL	14 mL	0.00104	0.0216	4:83

3.3 Characterization

Characterization techniques that were employed in this study include Powder X-ray diffraction (XRD), Raman Spectroscopy, Transmission Electron Microscopy (TEM), and Hydrogen Temperature Programmed Reduction (H_2-TPR).

3.4 Results and Discussion

Phase purity of the CeO_2 samples was quantified using Powder X-ray diffraction. As shown in Figures 1-3, all diffraction peaks were indexed to the cubic fluorite structure (JCPDS card number 34-0394) confirming that all the samples that had been synthesized were pure CeO_2. The Shrerrer equation was used to estimate the particle size of the samples while the (hkl) Miller indices and d-spacing information were used to compute the lattice constants of the samples. Crystal size and lattice constant information are summarized in Table 2 below.

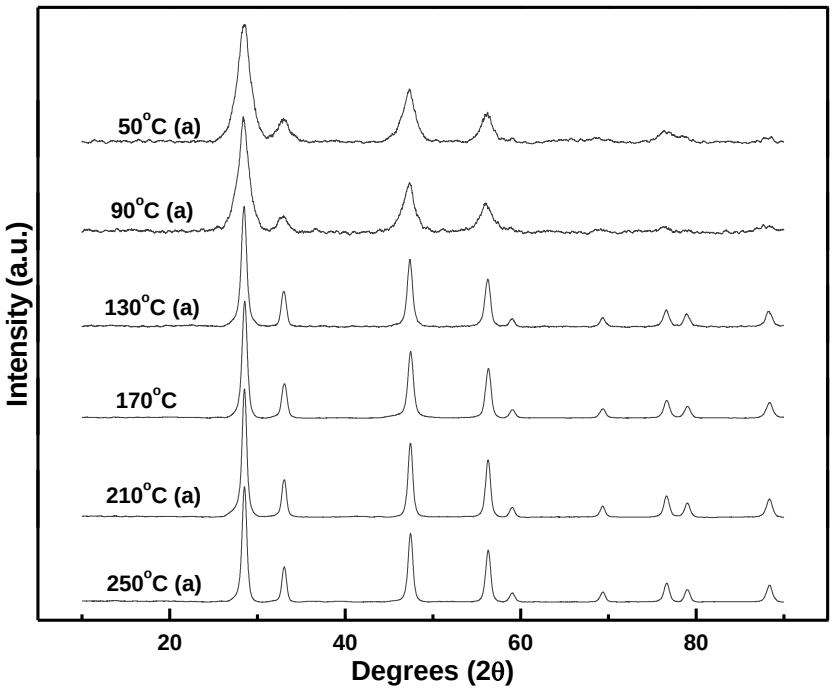

Figure 10: XRD data for set (a) samples.

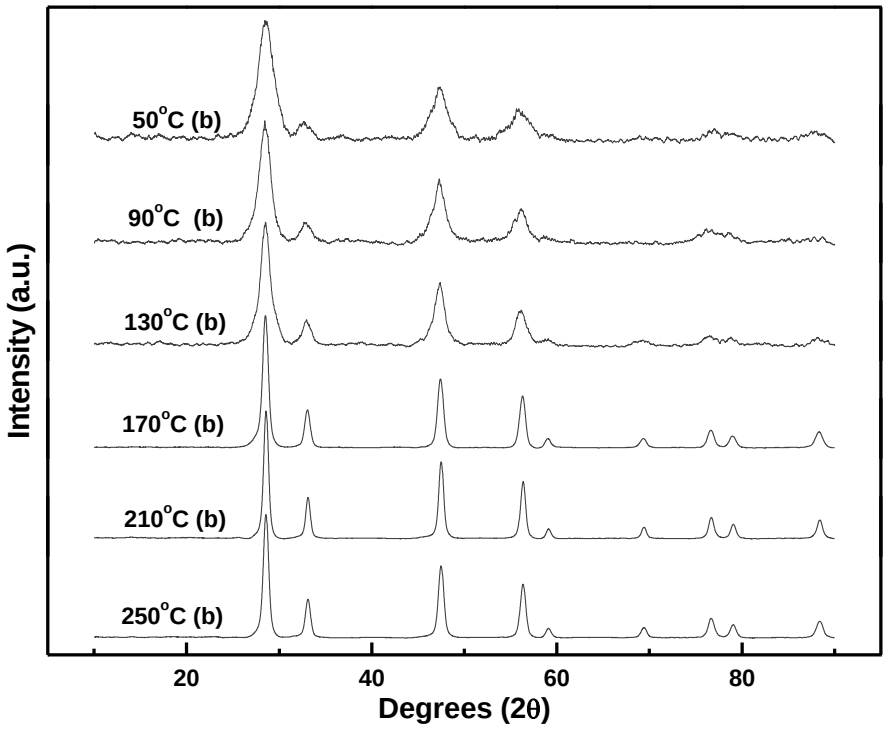

Figure 11: XRD data for set (b) samples.

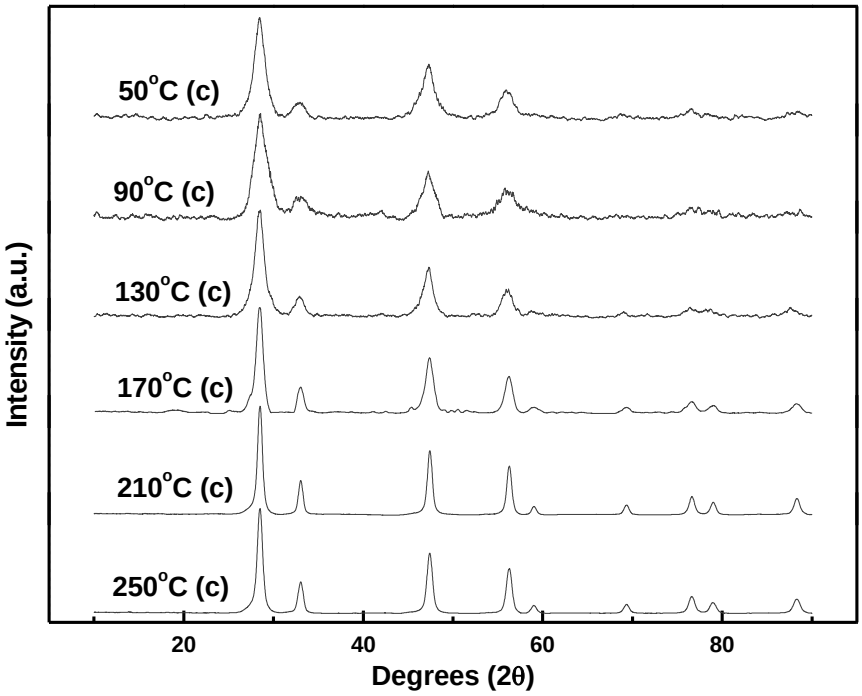

Figure 12: XRD data for set (c) samples.

Table 2 below is a summary of the calculated particle size and lattice constant information.

Table 2: Particle size and lattice constant information

Sample Identity	particle size (nm)	Lattice Constant (Å)
50°C (a)	7.54	5.43
50°C (b)	8.28	5.45
50°C (c)	6.06	5.44
90°C (a)	5.62	5.43
90°C (b)	5.65	5.43
90°C (c)	7.22	5.45
130°C (a)	13.61	5.42
130°C (b)	7.48	5.43
130°C (c)	5.83	5.45
170°C (a)	13.51	5.41
170°C (b)	14.08	5.42
170°C (c)	9.92	5.42
210°C (a)	15.32	5.42
210°C (b)	16.73	5.41
210°C (c)	16.11	5.42
250°C (a)	16.65	5.42
250°C (b)	15.32	5.41
250°C (c)	15.11	5.42

As was expected, different synthesis temperatures resulted to different CeO_2 sizes and morphologies with nanorods materializing at lower synthesis temperatures as compared to nanocubes. Such phenomena were also witnessed by Mai H.X. et al and were attributed to different hydrothermal pressures that were experienced at different synthesis temperatures [1]. As it has be seen shown in Figures 1-3, the absence or presence of and the resolution of the last four diffraction peaks that appeared between 68^o to 89^o can be used to qualitatively depict the extent of crystallinity in the different samples and hence can serve as a guide for speculating the probable crystal morphologies. Moreover, it is a known in solid state chemistry of CeO_2 that nanorods

tend to be less crystalline compared to nanocubes. It will be shown later in this study that the XRD profiles that had poorly missing or missing high angle diffraction peaks corresponded to CeO_2 nanorods while those that has well crystalline high angle peaks corresponded to CeO_2 nanocubes [1-3].

Also as it was expected, XRD peak broadening, peak shifting and intensity differences were consistent with sample particle sizes and lattice constant strains (compare Figures 1-3 with Table 2). The data presented here shows that higher synthesis temperatures resulted to higher peak intensities and larger particle sizes while lower temperatures resulted to smaller particle sized and lower peak intensities. It was therefore concluded that particle crystallinity and size played a major role in determining the shape, position and intensities of the XRD peaks. The differences in particles size and lattice constants were a consequence of the hydrothermal reaction parameters that included synthesis temperature and solvent pressure. Figures 4 and 5 illustrate how particle size and lattice constants varied with synthesis temperature, which is consistent with the results in the literature [1, 4].

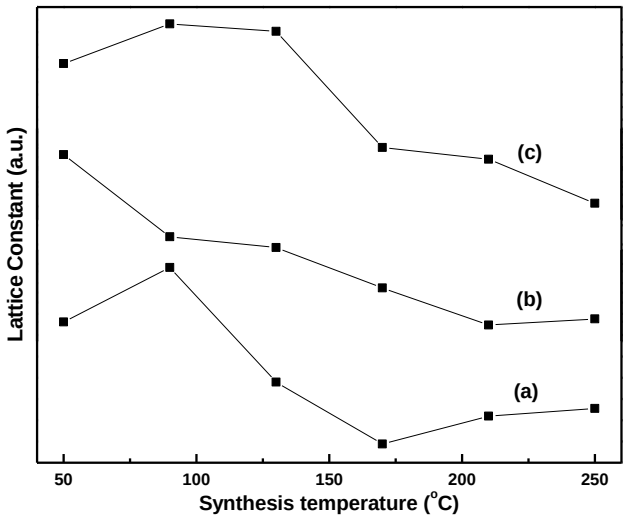

Figure 13: Variation of lattice constant with synthesis temperature.

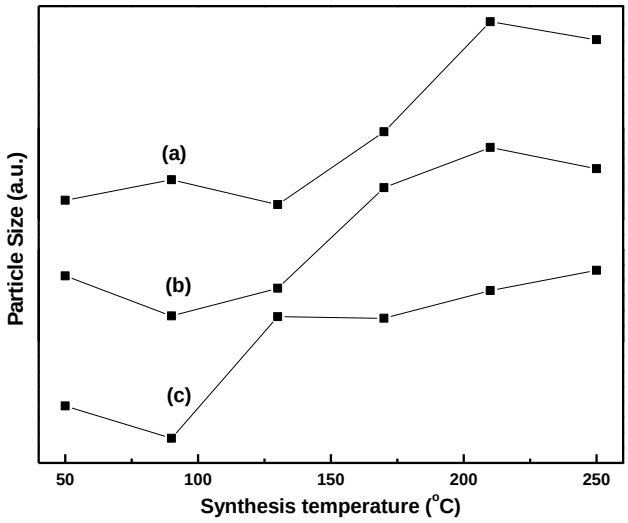

Figure 14: Variation of particle size with synthesis temperature.

Figures 6-9 show the Raman spectra of the pure ceria samples. The first order scattering peaks that appear at close to 450 cm^{-1} are an evidence of the symmetric vibrations of the F2g modes of the CeO_2 while the second order peaks that appear at close to 600 cm^{-1} can be ascribed to the extrinsic oxygen vacancies that were present in the samples. The scattering bands of the samples that were synthesized at 50 ^oC appeared at the lowest wavenumbers while the other samples showed a progressive peak shifting towards higher wave numbers as the synthesis temperatures were increased. This observation was consistent with the XRD data and implies that the lattice constants of the samples experienced a progressive lattice constant contraction with increasing particle size as indicated in Figures 4 and 5. This phenomenon was a result of increased oxygen vacancy concentrations and higher concentration of Ce^{3+} ions as the particle sizes decreased. In addition, increased oxygen vacancies and increased contents of Ce^{3+} ions lead also led to peak asymmetry and reduced peak intensities that were observed on CeO_2 nanorods. A closer probe into the Raman spectra also shows that the second order

scattering peaks for nanorods and nanocubes that occurred at around 600 cm^{-1} and 726 cm^{-1} respectively also had peak intensity disparities. These peak differences arose from differences in the oxygen vacancy concentrations of the samples. Findings in this study were consistent with other research groups` findings in which CeO_2 nanorods were found to have higher oxygen vacancies and low intensity asymmetric F2g scattering peaks as compared to CeO_2 nanocubes. [1, 4-6]

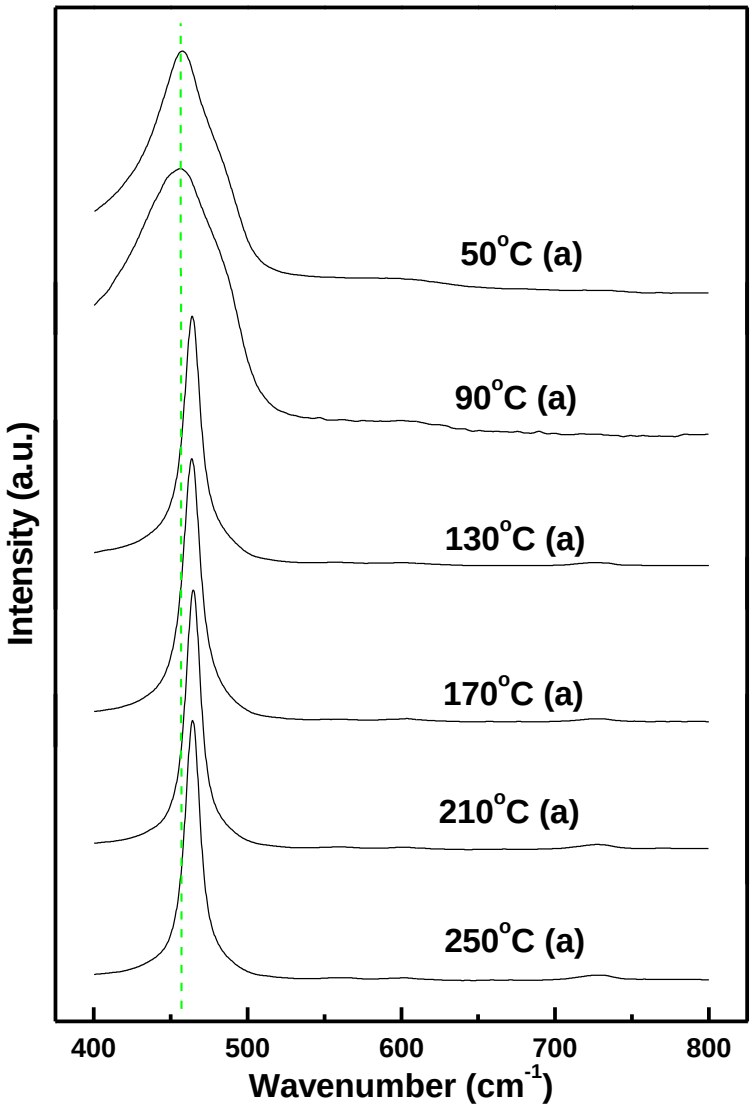

Figure 15: Raman peak shifting with increasing synthesis temperature (a = lowest OH^- ion concentration – see Table 1).

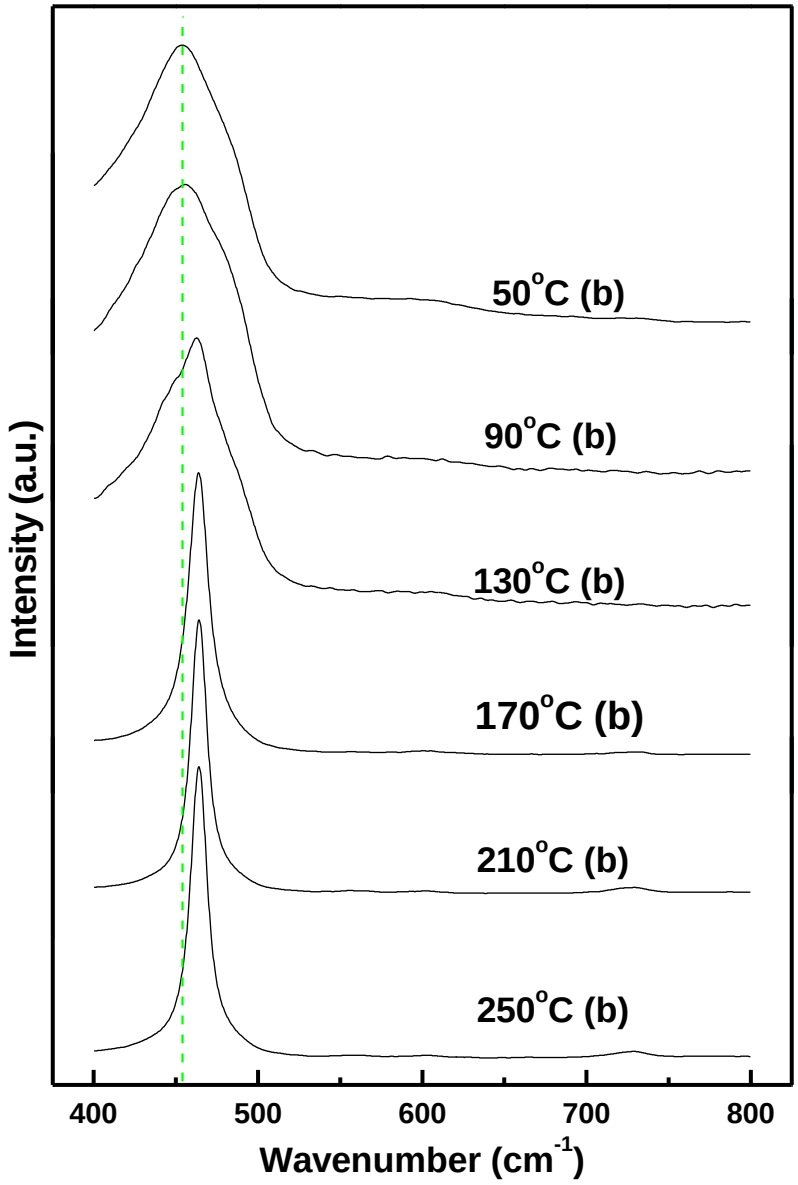

Figure 16: Raman peak shifting with increasing synthesis temperature (b = intermediate OH^- ion concentration – see Table 1).

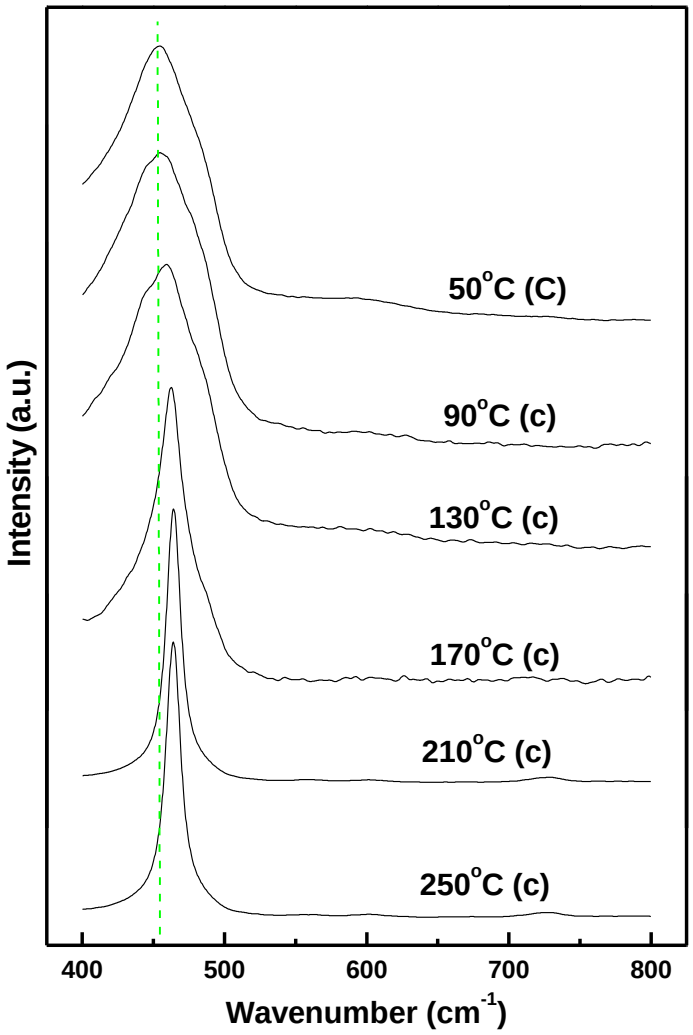

Figure 17: Raman peak shifting with increasing synthesis temperature (c = highest OH^- ion concentration – see Table 1).

The most interesting finding in this study however was the fact that increasing the concentration of OH^- ion during synthesis progressively deferred the formation of nanocubes as synthesis temperatures were increased. In addition, it was also noted that increasing the concentration of OH^- ion during synthesis of ceria nanoparticles increased the lattice strain of nanoparticles while maintaining the particle size and morphology. As

far as we are concerned, both of these phenomena are new findings (in the study of cerium oxide) and are found very relevant for applications in which one may anticipate to improve on or engineer the lattice strain and oxygen vacancies in CeO_2 nanoparticles (on a need basis) while retaining their size and morphology. The Raman spectra below show how OH^- ion concentration affected peak position and shape during synthesis. These findings were found particularly useful in the fundamental studies of CeO_2 especially considering that most of the studies that have been documented in the literature before only address the effect of temperature on the hydrothermal synthesis of ceria with very little information about how OH^- ion concentration could be used in need driven customized synthesis. The most infringing phenomenon in these findings was the fact that both oxygen vacancies and lattice constants could be adjusted within the same morphology and synthesis temperature [1, 4-7].

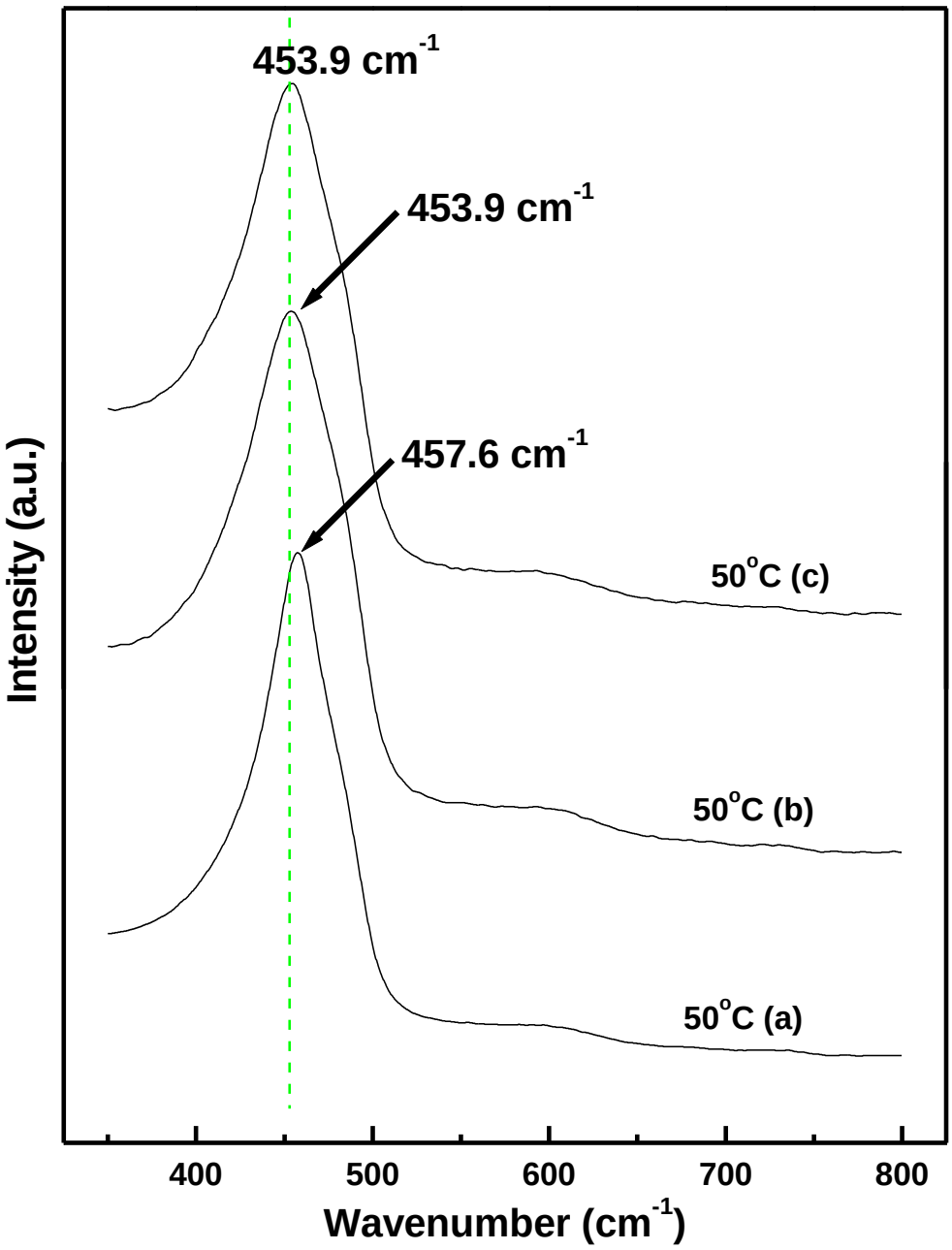

Figure 18: Raman peak shifting with increasing OH^- concentrations. Samples were synthesized at 50 °C.

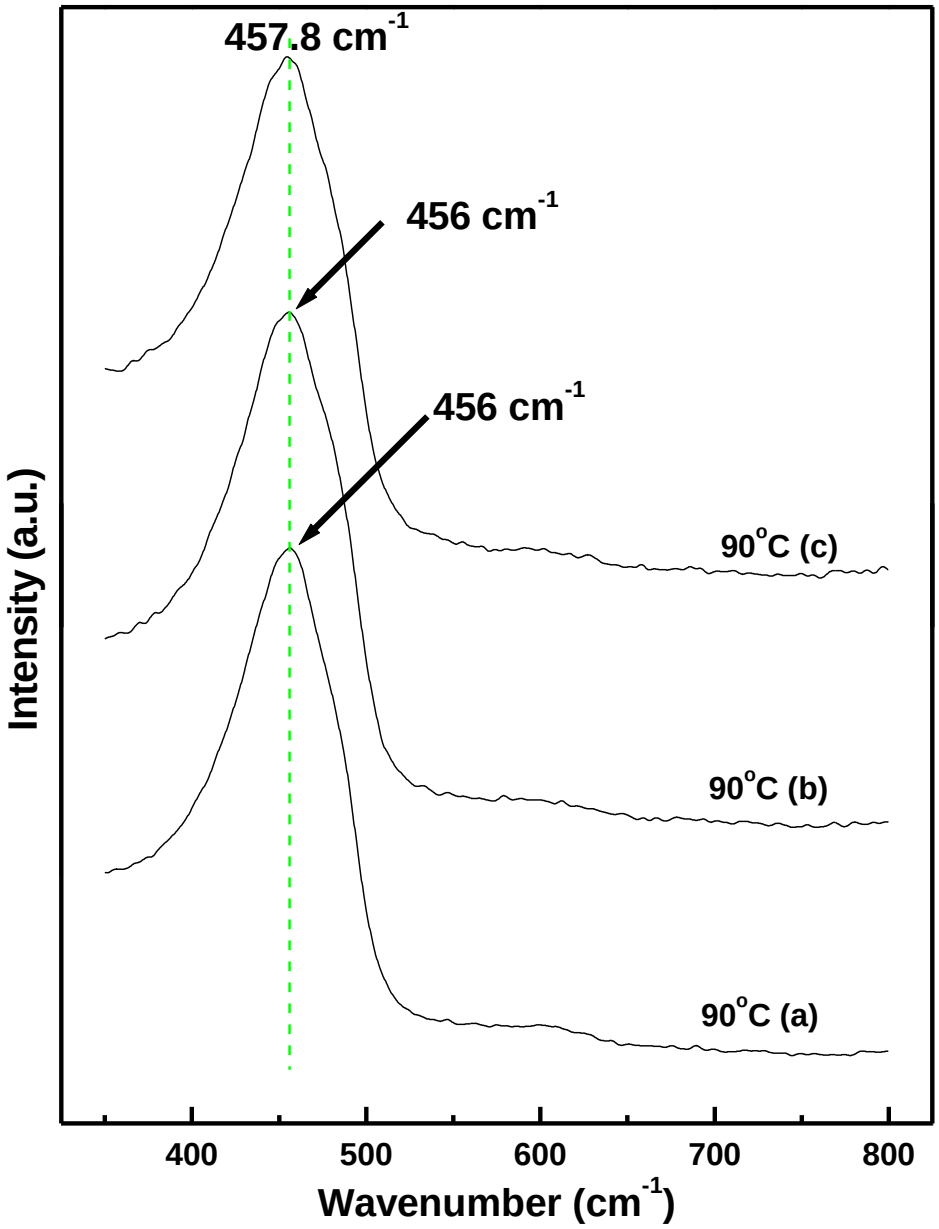

Figure 19: Raman peak shifting with increasing OH^- concentrations. Samples were synthesized at 90 °C.

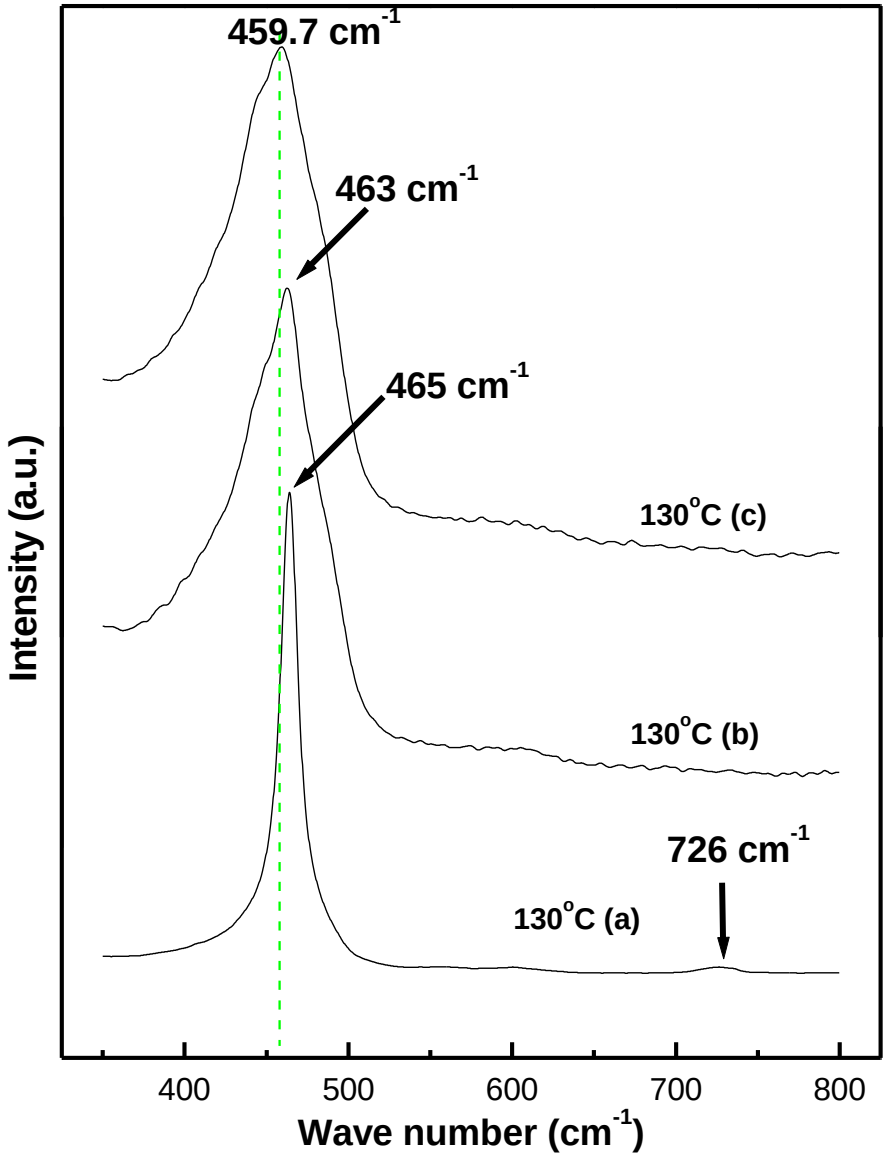

Figure 20: Raman peak shifting with increasing OH^- concentrations. Samples were synthesized at 130 ^oC.

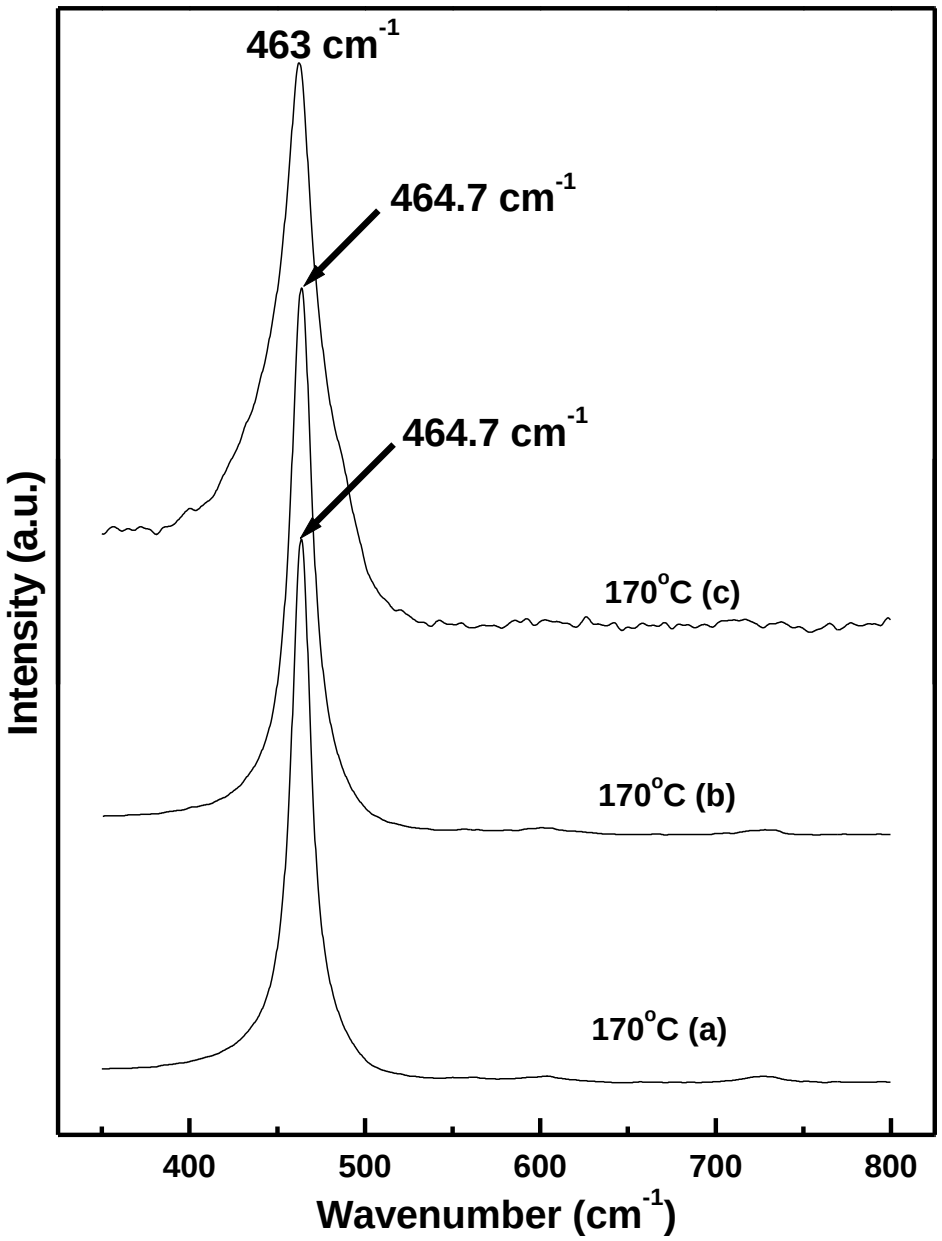

Figure 21: Raman peak shifting with increasing OH^- concentrations. Samples were synthesized at 170 ^oC.

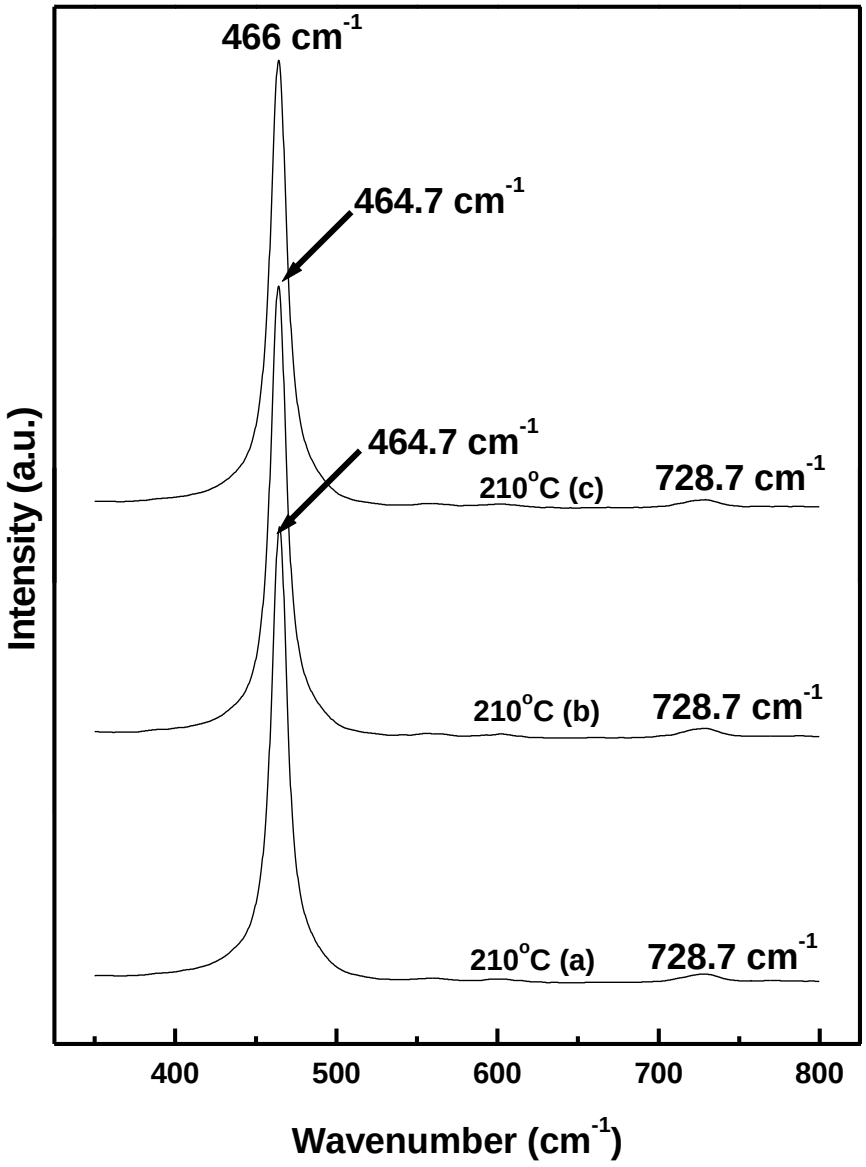

Figure 22: Raman peak shifting with increasing OH^- concentrations. Samples were synthesized at 210 ^oC.

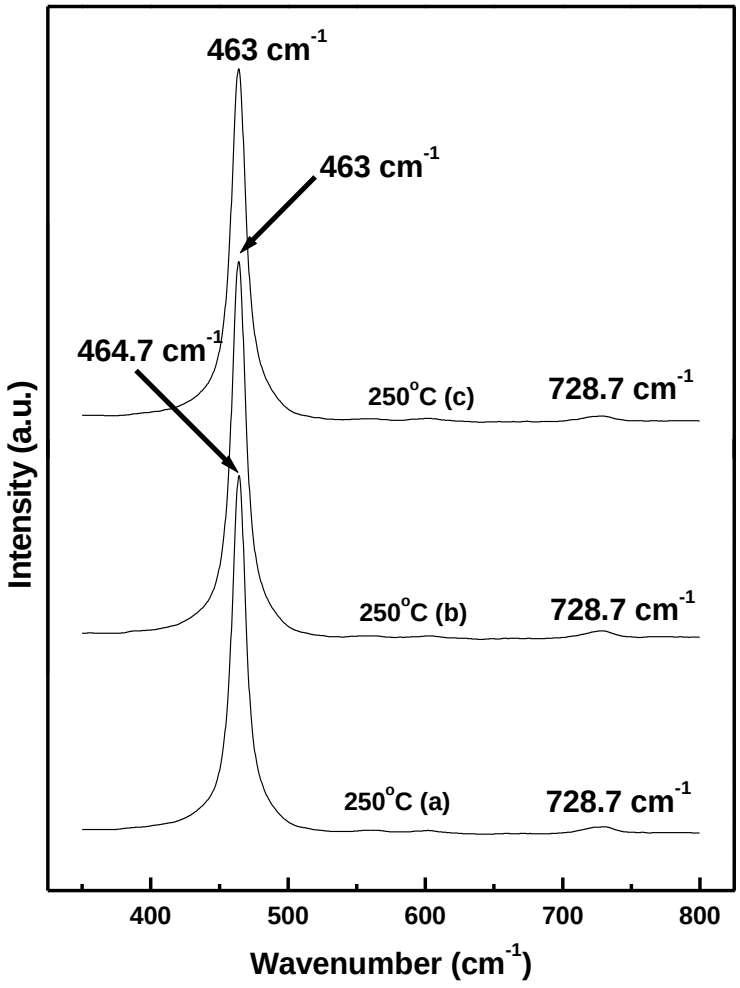

Figure 23: Raman peak shifting with increasing OH^- concentrations. Samples were synthesized at 250 ^oC.

H_2-TPR studies were conducted on the CeO_2 samples in order to determine how sample size, morphology and oxygen vacancies affected their surface and bulk reduction. It is clear from Figures 15-17 that the intensities and positions of the surface and bulk reduction bands were highly dependent on the morphologies and particle sizes of the samples. For instance, a careful inspection of the data reveals that CeO_2 nanorod samples exhibited high intensity surface and low intensity bulk reduction bands while CeO_2 nanocubes showed low intensity surface and high intensity bulk reduction bands. It is

also evident form our results that peaks that corresponded to CeO_2 nanorods were shifted towards lower reduction temperatures as compared to those of nanocubes. In addition, a qualitative comparison of Figures 1-3 and 15-17 shows a clear relationship between the absence and presence of the last four XRD peaks with the peak positions and intensities of the surface and bulk reduction bands. It is evident from the data that samples that had their last four XRD peaks missing or poorly resolved showed better low temperature catalytic activity as compared to those that showed all XRD diffraction peaks. This trend was also consistent with Raman data in that, samples whose scattering peaks were shifted towards lower wave numbers showed better catalytic acidity as compared to those whose Raman peaks appeared at higher wavenumbers. This observation was attributed to the nano-size effect and the fact that nanorods had more oxygen vacancies than nanocubes. One of the objectives of this study was therefore achieved by showing that both high crystallinity and large particle sizes in CeO_2 nanoparticles reduces their low temperature reducibility and activity by lowering their surface and bulk oxygen vacancies that in turn lower their surface and bulk oxygen mobility. Samples that showed high intensity surface reduction bands and low intensity bulk reduction bands indicated that most of their oxygen ions were accessible on their surface due to their higher concentrations of oxygen vacancies. On the other hand, samples that demonstrated low intensity surface reduction bands and high intensity bulk reduction bands revealed that most of their oxygen ions were not accessible on their surface and hence required higher activation energies in order for them participate in the H_2-indiuced reduction process. Figures 9-11 below are a compilation of the H_2-TPR [1, 8-13].

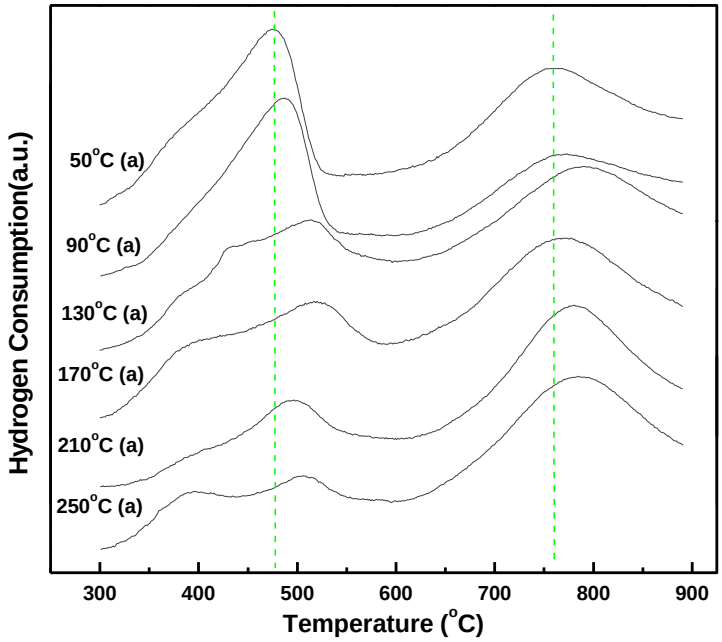

Figure 24: H_2-TPR peak shifting with increasing synthesis temperature (a = lowest OH^- ion concentration – see Table 1).

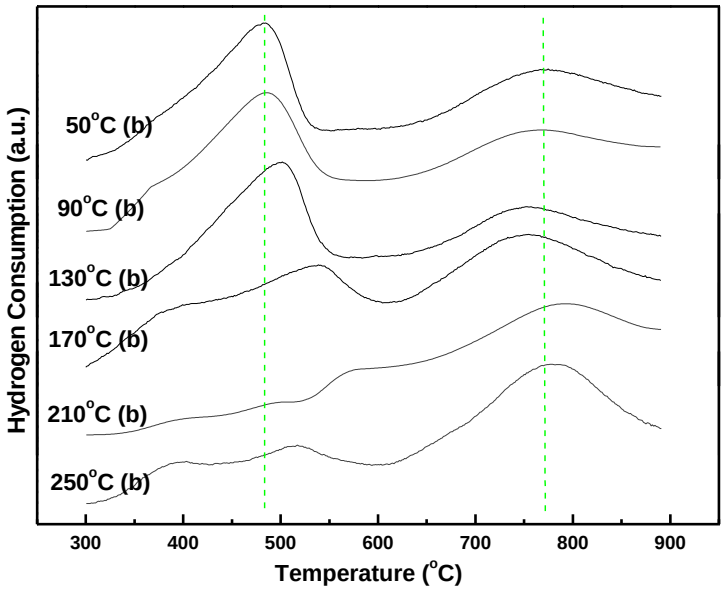

Figure 25: H_2-TPR peak shifting with increasing synthesis temperature (b = intermediate OH^- ion concentration – see Table 1).

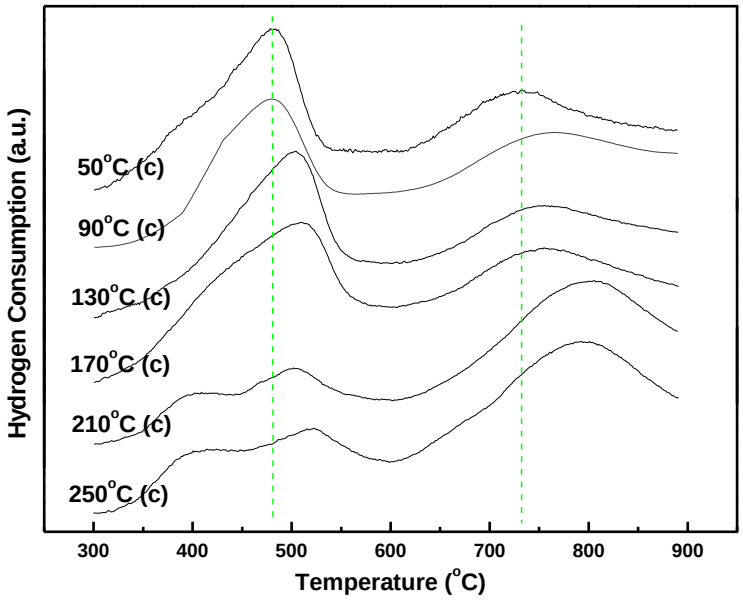

Figure 26: H_2-TPR peak shifting with increasing synthesis temperature (c = highest OH^- ion concentration – see Table 1)

3.5 Conclusion

We have shown that synthesis temperature plays a critical role in controlling the shape, morphology, oxygen vacancy concentration and low temperature reducibility in CeO_2 nanoparticles. We have also seen that OH^- ion concentration can play an important role in engineering the lattice constants and oxygen vacancy concentrations of ceria nanoparticles within the same particle morphology and synthesis temperature. As far as we are concerned, the latter is a new finding that must be explored further in engineering defects in CeO_2 systems.

3.6 References

1. Mai, H.X. et al., J. *Phys. Chem. B.* **109**, 24385 (2005)
2. Tok, A.I.Y., Boey, F.Y.C., Sun, X.L, *J. Mater. Process. Technol*. **190**,217 (2007)
3. Zagaynov, I.V., Kutsev, S.V. *Appl. Nanosci*. (2013)
4. Zhao, C. et al., *Nanoscale Res. Lett*. **8**, 172 (2013)
5. Zhang, F. et al., *Appl. Phys. Lett*. **80**, 1 (2002)
6. Maensiri, S. et al. *Cryst. Growth Des*. **7**, (5) 950 (2007)
7. Godinho, M.J., *Mater. Lett*. **61**, 1904 (2007)
8. Sohlberg, K., Pantelides, S.T., Pennycook, S.J., *J. Am. Chem. Soc*. **123**, 6609 (2001)
9. Kundakovic, L.J., Stephanopoulos, M.F., *J. Catal.* **179**, 203 (1998)
10. Kundakovic, L.J., Stephanopolos, M. F., *Appl. Catal. A. Gen*. **171**, 13 (1998)
11. Zhu, H. et al. *J., Catal*. **225**, 267 (2004)
12. Matolin, V et al., *Nanotech*. **20**, 215706 (2009)
13. Gayen, A. et al., *Appl. Catal*. *A: Gen*. **315**, 135 (2006)

Chapter 4 One-pot hydrothermal synthesis and high temperature thermal stability of $Ce_xZr_{1-x}O_2$ nanocrystals

4.1 Introduction

Cerium-based oxides are widely used in automotive three-way catalytic converters to reduce the emissions of CO, NO_x, and unburned hydrocarbons [1-3]. Mixing ceria (cerium oxide or CeO_2) with other oxides (i.e., ZrO_2, TiO_2, Al_2O_3, and transition metal oxides) to form solid solution or mixed oxide nanoparticles can enhance the low-temperature oxygen storage capacity (OSC), increase the thermal stability of the materials, and prevent sintering of nanoparticles at higher temperatures [4-8]. The mechanism by which the addition of other oxides enhances the low-temperature properties is not yet well understood, but it likely involves the creation and stabilization of oxygen vacancies in the ceria lattice. Synthesizing compositionally homogeneous cerium-based oxides, and understanding the solid solution process between ceria and other oxides and their influence on crystal structure, defect structures, and transport properties are critical to further enhance the performance of cerium-based oxide nanocatalysts in the catalytic converters and other applications.

Several known techniques have been selected for preparing compositionally homogeneous cerium-containing mixed oxides, including co-precipitation [9-10], sol-gel [10-11], wet-milling phase reaction [12], and spray pyrolysis [13]. Amongst these methods, co-precipitation is the most commonly used method. Co-precipitation of CeO_2-ZrO_2 mixed oxides from aqueous (Ce, Zr) metal containing solution can be achieved by the addition of base or, by addition to the base solution. However, phase separation with Ce-rich and Zr-rich phases is frequently observed when the co-precipitation conditions are not well controlled. Suda et al [12] reported a synthesis method of CeO_2-ZrO_2 solid

solutions by solid phase reaction via a wet milling process using CeO_2 and ZrO_2. CeO_2-ZrO_2 solid solution phases exhibit cubic (c-), monoclinic (m-), and tetragonal (t-) polymorphism with a number of metastable tetragonal form t′, t″, t‴ and t* etc. [14-15]. Due to the structural complexity, it is still very challenging to synthesize nanoscale compositionally homogeneous CeO_2-ZrO_2 mixed oxides, as the mixed oxides need to accommodate the discrepancy in crystal structure, ionic size, oxidation states, and oxygen-metal coordination numbers of cubic CeO_2 and monoclinic ZrO_2. In this paper, we report a facile one-step hydrothermal synthesis method to prepare compositionally homogeneous $Ce_xZr_{1-x}O_2$ ($0 \leq x \leq 1$) solid solutions and the thermal stability of the prepared nanocrystals under oxidation and reduction atmosphere at high temperatures.

4.2 Experimental section

High surface area $Ce_xZr_{1-x}O_2$ ($0 \leq x \leq 1$) samples were synthesized using a hydrothermal method. Typically, 0.1 M $Ce(NO_3)_3 \cdot 6H_2O$ (Alfa Aesa, 99.99%) and 0.1 M $ZrO(NO_3)_2 \cdot xH_2O$ (Alfa Aesa, 99.9%, x~2) solutions according to specific oxide ratios were mixed and stirred for 10 mins, and then 6 M NaOH solution was added. The suspension solutions were thoroughly mixed for 40 mins at room temperature, which is a critical step to prepare compositionally homogeneous oxide solid solutions as discussed in the following. The resulting suspension solutions were heated in 200 ml stainless steel Teflon-lined autoclaves (~50 % filled) at temperature between 50 ^oC to 220 ^oC (In this paper, the hydrothermal temperature used was 150 ^oC) with a dwell time for 48 hrs. At the end of reaction, the autoclaves were cooled to room temperature and the precipitates were separated, filtered and washed repeatedly using 500 ml distilled water, to remove the unreacted NaOH, and then washed with ethanol to avoid hard agglomeration between

the nanoparticles during drying. The resulting powders were then dried at 50 ^{o}C for 12 hrs. The thermal stability of the $Ce_{0.5}Zr_{0.5}O_2$ sample was tested in an alumina tube furnace from 900 ^{o}C to 1400 ^{o}C with the carrier-gas of 5%H_2/95%N_2 mixture and O_2 for the reduction and oxidation treatments, respectively. The dwell time for the heat treatments at each temperature was 5 hrs.

4.3 Characterization

Powder X-ray diffraction (XRD) analysis was performed on a Rigaku Miniflex II diffractometer using Cu Kα radiation with a wavelength of 1.5408 Å. The samples were loaded on an aluminum plate and the data were collected over a 2θ range of 10^{o}-90^{o} with a step size of 0.5^{o}/min. The recorded patterns were analyzed using JADE software to determine peak positions, lattice constant, and average crystalline sizes by use of Scherer's formula.

JEOL 2100 transmission electron microscope (TEM) was used for structural and chemical analysis of the nanocrystals at atomic level, operated at 200 kV and equipped with an EDAX detector for chemical composition analysis and annular dark-field detector. The chemical composition of individual nanocrystals was determined by energy dispersive X-ray spectroscopy (EDX) analysis in scanning transmission electron microscopy (STEM) mode with a focused electron probe. High resolution transmission electron microscopy (HRTEM) was used to determine the exposed crystal facets in individual $Ce_xZr_{1-x}O_2$ ($0 \leq x \leq 1$) nanocrystals. TEM samples were prepared by using dilute suspensions of the nanopowder samples. These solutions were obtained by ultrasonicating particles in ethanol for 10 min then dropping the suspension of the sample powders onto an ultrathin carbon film/holey carbon, 400 mesh copper grid (from Ted

Pella) and letting it air dry for several hours. X-ray fluorescence spectroscopy (XRF) was performed on an S2 Ranger X-Ray fluorescence spectrometer. Raman scattering was performed in a Kaiser Optical System (RXN1) with a 785 nm laser module and 10 second exposure time. All peak intensities and positions were obtained with Lorentzian fitting. The Raman scattering in the 100-3200 cm^{-1} region was collected.

Hydrogen temperature programmed reduction (H_2-TPR) was used to test the H_2 consumption during the reduction ($4CeO_2+H_2 \rightarrow 2Ce_2O_3+H_2O$) of the synthesized oxide nanopowders. H_2-TPR and single point BET surface area of the as-prepared $Ce_xZr_{1-x}O_2$ ($0 \leq x \leq 1$) nanocrystals in powder form were carried out in a Micromeritics AutoChem™ II 2920 chemisorption analyzer instrument. The samples were pretreated at 110 ^oC for 1 hr, and then they were cooled to room temperature. Following the pretreatment, the powder samples were heated at a rate of 10 °C/min from room temperature to 900 °C. A cold trap filled with a mixture of isopropanol, KCl, and ice was placed in the cold trap region of the instrument in order to trap water vapour from the exhaust gas line.

4.4 Results and discussion

4.4.1 One-pot hydrothermal synthesis of $Ce_xZr_{1-x}O_2$ ($0 \leq x \leq 1$)

Figure 1 shows the XRD patterns for a series of $Ce_xZr_{1-x}O_2$ ($0 \leq x \leq 1$) from pure CeO_2 and ZrO_2 to mixed oxides (or solid solutions) nanopowders, prepared via hydrothermal reactions at 150 ^oC with a dwell time 48 hrs. The diffraction peaks of pure CeO_2 and ZrO_2 were indexed as face-centered cubic fluorite structured CeO_2 (JCPDS file 34-0394) and monoclinic ZrO_2 (JCPDS 37-1484) with lattice parameters of a=5.156 Å, b=5.191 Å, c=5.304 Å, respectively. The XRD patterns of the mixed $Ce_xZr_{1-x}O_2$ ($0<x<1$) did not show any extra diffraction peaks due to the doping ZrO_2 component from x=0.9

up to x=0.2 but the presence of Zr in individual nanocrystals was evidenced by EDX analysis with a focused electron probe in STEM mode and XRF compositional analysis. The diffraction peaks in mixed oxides were indexed using cubic CeO_2, although the peak positions were shifted to higher diffraction angle when doping more ZrO_2, compared to standard cubic CeO_2. We attribute this shift to the difference in ionic size between Ce^{4+}(0.97 Å) and Zr^{4+}(0.84 Å), according to the Bragg's law ($2dsin\theta = n\lambda$, where d is the spacing between the planes in the atomic lattice, θ is the diffraction angle, n is an integer, and λ is the wavelength of incident X-ray wavelength). Since Zr^{4+} has a smaller ionic size compared to Ce^{4+}, doping with Zr^{4+} in CeO_2 lattice will result in a shrinked lattice (smaller d spacing and lattice constant). According to the Bragg's law, the diffraction angle θ will increase with the increasing ZrO_2 concentration in $Ce_xZr_{1-x}O_2$ ($0 \le x \le 1$). When ZrO_2 concentration is higher than 80% ($x<0.2$ in $Ce_xZr_{1-x}O_2$), phase separation appears for the $Ce_{0.1}Zr_{0.9}O_2$ sample which is consistent with CeO_2-ZrO_2 phase diagram [14-15].

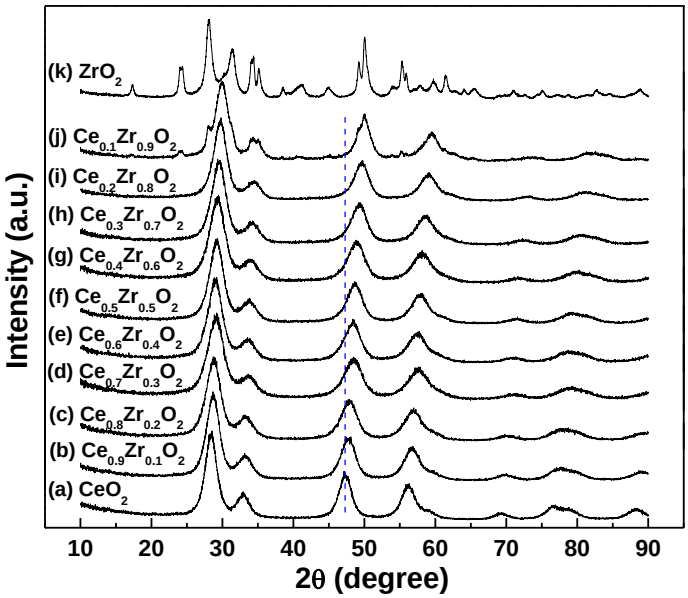

Figure 27: X-ray diffraction patterns of $Ce_xZr_{1-x}O_2$ ($0 \le x \le 1$) nanocrystals via a one-step hydrothermal reaction at 150 ^oC for 48 hrs.

Table 1 compares BET surface area, the crystalline size, and lattice parameter between pure CeO_2 or ZrO_2 and $Ce_xZr_{1-x}O_2$ ($0<x<1$) mixed oxides. Monoclinic ZrO_2 shows the lowest BET surface area, much higher crystallinity, and larger crystalline size. It is noted that the obtained ZrO_2 presents a monoclinic structure after hydrothermal processing at 150 ^oC without containing hydroxide phase (i.e, $Zr(OH)_4$) in the strong base solution environment (6 M NaOH), so no further decomposition step is necessary to form zirconium oxide (ZrO_2) nanocrystals. Direct formation of zirconium oxide is one of the advantages for hydrothermal reaction, in comparison with the initial formation of zirconium hydroxide in other chemical methods using a base solution ($NH_3 \cdot H_2O$ or NaOH). Also unlike other metal oxides (Al_2O_3, Fe_2O_3, Co_3O_4, NiO, PrO_2, TbO_2), hydroxides (γ-AlO(OH), FeO(OH), $Co(OH)_2$, $Ni(OH)_2$, $Pr(OH)_3$, $Tb(OH)_3$) forms preferably under strong base conditions during hydrothermal reaction. Therefore, the direct formation of ZrO_2 nuclei under hydrothermal reaction may facilitate the formation of $Ce_xZr_{1-x}O_2$ ($0<x<1$) as solid solution process between CeO_2 and ZrO_2 proceeds in a liquid phase environment under pressure. The highest BET surface area obtained is from pure CeO_2 (154 m^2/g), and the mixed oxides show a little lower BET surface area (108~143 m^2/g) which is higher than the reported values in other works using co-precipitation and sol-gel methods [9-11].The mixed oxides show on average a little smaller particle sizes than that of pure CeO_2. Table 1 also shows the relationship between ZrO_2 content and the lattice parameter of all $Ce_xZr_{1-x}O_2$ ($0\leq x\leq 1$) nanocrystals samples, calculated using the (111) peak. The calculated lattice parameters for the $Ce_xZr_{1-x}O_2$ ($0\leq x\leq 1$) nanocrystals follow the same trend with the XRD results, indicating a decreased lattice parameter and unit cell volume as the ZrO_2 concentration increases.

Table 3: BET surface area, crystalline size, and lattice parameters of the $Ce_xZr_{1-x}O_2$ ($0 \leq x \leq 1$) nanocrystals

Sample Composition	BET Surface Area (m^2/g)	Crystalline Size from XRD (nm)	Lattice Parameter (Å)
ZrO_2	24	20.2	a:5.156; b:5.191; c:5.304
$Ce_{0.1}Zr_{0.9}O_2$	108	3.7	a:5.196; b:5.196; c:5.237
$Ce_{0.2}Zr_{0.8}O_2$	112	4.0	5.249
$Ce_{0.3}Zr_{0.7}O_2$	108	3.7	5.278
$Ce_{0.4}Zr_{0.6}O_2$	121	3.5	5.299
$Ce_{0.5}Zr_{0.5}O_2$	113	3.5	5.318
$Ce_{0.6}Zr_{0.4}O_2$	119	3.7	5.362
$Ce_{0.7}Zr_{0.3}O_2$	120	3.3	5.381
$Ce_{0.8}Zr_{0.2}O_2$	115	3.7	5.416
$Ce_{0.9}Zr_{0.1}O_2$	143	3.9	5.430
CeO_2	154	4.6	5.446

The TEM images with the selected compositions ($Ce_{0.7}Zr_{0.3}O_2$, $Ce_{0.5}Zr_{0.5}O_2$, and $Ce_{0.3}Zr_{0.7}O_2$) are shown in Figure 2. The TEM analyses confirmed that the size of nanocrystals is in the range of 3-5 nm in diameter with single crystal characteristic. It seems that a morphological change of nanocrystals occurs from irregular shape with well-defined crystal facets to round shape as the ZrO_2 concentration increases. HRTEM image of the $Ce_{0.7}Zr_{0.3}O_2$ sample (Figure 2-a-2) clearly display a faceted surface terminated by the atomic-level lattice fringes. Due to the low scattering power of oxygen when compared with heavy cerium, the dark contrast (black spots) in the HRTEM images (Figure 2) is presumed to be a terminating layer of cerium cations. Analysis of the images showed that these facets/edges terminate in {111} and {200} planes, based on their d-spacing and the corresponding diffractogram. For the $Ce_{0.3}Zr_{0.7}O_2$ sample, the atomic-level surfaces are relatively rough and the particle morphology eventually changes to round shape, which is clear in the low-magnification image (Figure 2-c-1). This observation of morphology change might be related to the structure transformation from

cubic to tetragonal with the increased ZrO_2 concentration illustrated in the CeO_2-ZrO_2 phase diagram [14-15].

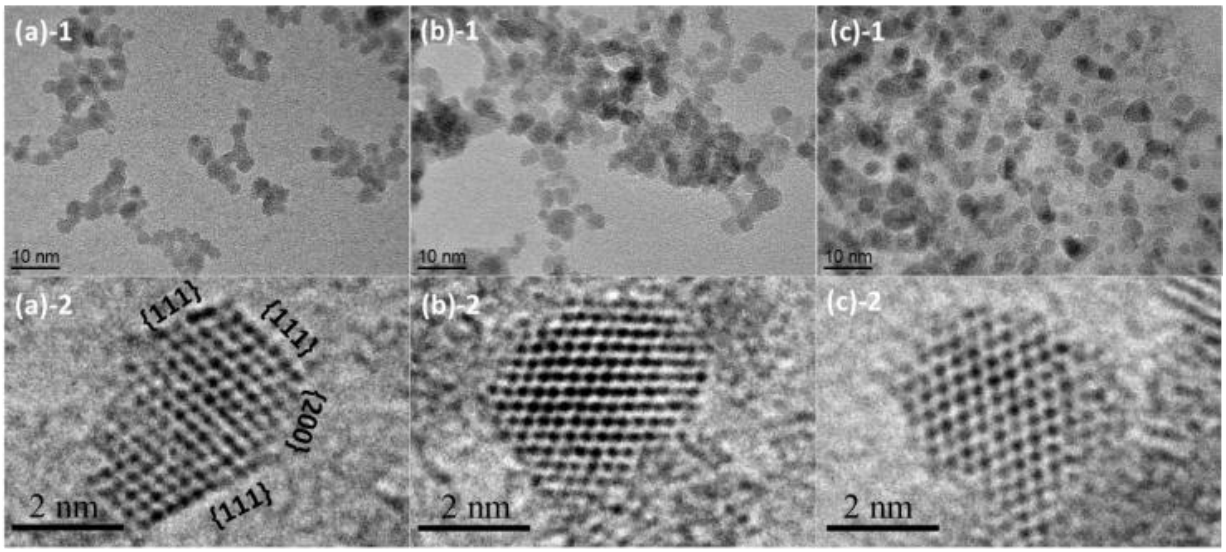

Figure 28: Representative TEM and HRTEM images of $Ce_{0.7}Zr_{0.3}O_2$ (a-1/2), $Ce_{0.5}Zr_{0.5}O_2$ (b-1/2), and $Ce_{0.3}Zr_{0.7}O_2$ (c-1/2) nanocrystals prepared by hydrothermal reaction at 150 ^oC for 48 hrs with a 40 mins stirring treatment in air.

It should be pointed out that all $Ce_xZr_{1-x}O_2$ ($0 \le x \le 1$) samples, reported in Figure 1 and Table 1, were stirred on a magnetic hot plate for 40 mins at room temperature before the hydrothermal reactions. It was found that the stirring step was playing a critical role in the control of compositional homogeneity, particle size, and morphology of final products. For example, for pure CeO_2, nanocubes with a size of 20 nm was obtained without initial stirring, but irregular shape nanocrystals with much smaller particle size (4~5 nm) were obtained if stirring the mixture of $Ce(NO_3)_3$ and NaOH for 40 mins before loading into the autoclave reactor, as shown in TEM images of Figure 3 (a-1 and b-1). HRTEM images and the corresponding fast Fourier transform (FFT) diffractograms are shown in Figure 3 a-2 and b-2 in order to study the detailed crystalline feature of such polyhedral nanocrystals. The inserted diffractorgrams confirm the cubic (or psudocubic)

structure and single crystal characteristics of nanocrystals, and the HRTEM images show the dominant {111} surface facets for irregular particles for the stirred samples and {200} surface facets for the nanocubes in the unstirred samples.

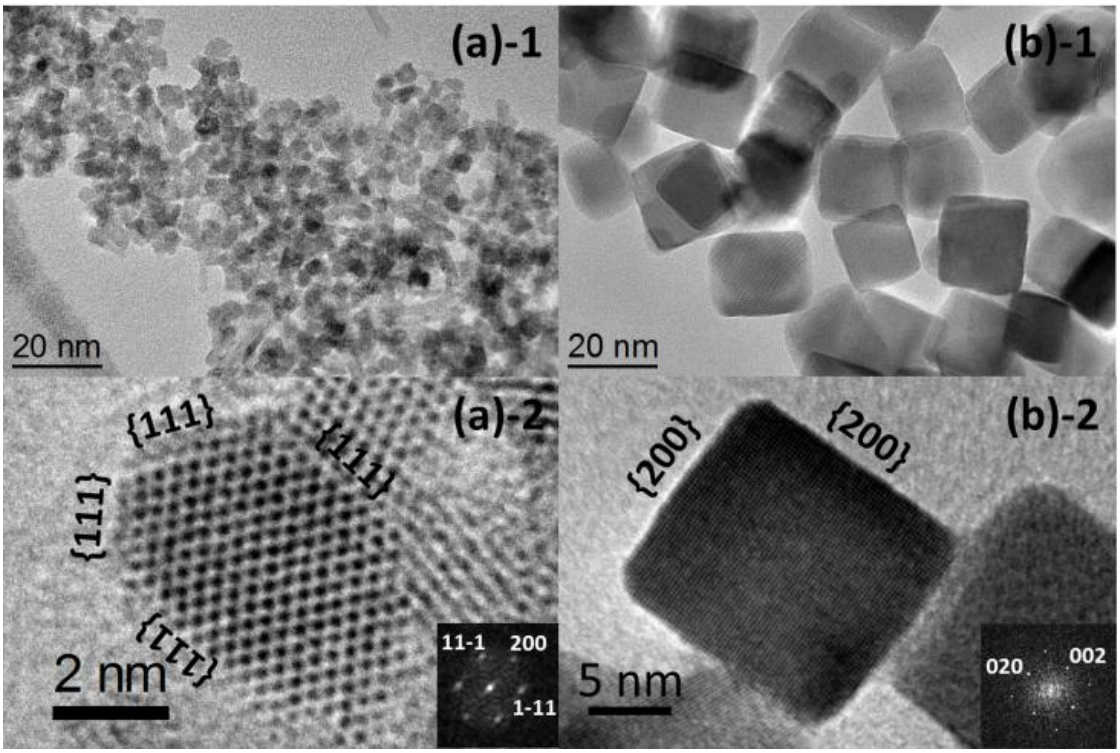

Figure 29: TEM images of CeO_2 nanocrystals prepared by hydrothermal reaction at 150 ^oC (a) with and (b) without stirring treatment.

4.4.2 Effect of stirring on the formation of solid solutions

Figure 4 compares the XRD results of the $Ce_{0.7}Zr_{0.3}O_2$, $Ce_{0.3}Zr_{0.7}O_2$ and $Ce_{0.5}Zr_{0.5}O_2$ samples with and without stirring treatment before loading to the autoclave for hydrothermal reaction. For the stirred samples, it is found that {111} diffraction peak at about 29^o in the patterns shifts to higher diffraction angle with increasing ZrO_2 concentration. This indicates a decrease in unit cell volume due to the incorporation of smaller Zr^{4+} ions into lattice positions. For the unstirred samples, the phase separation

occurs for the $Ce_{0.7}Zr_{0.3}O_2$, although $Ce_{0.3}Zr_{0.7}O_2$ and $Ce_{0.5}Zr_{0.5}O_2$ samples show an apparently compositional homogeneity.

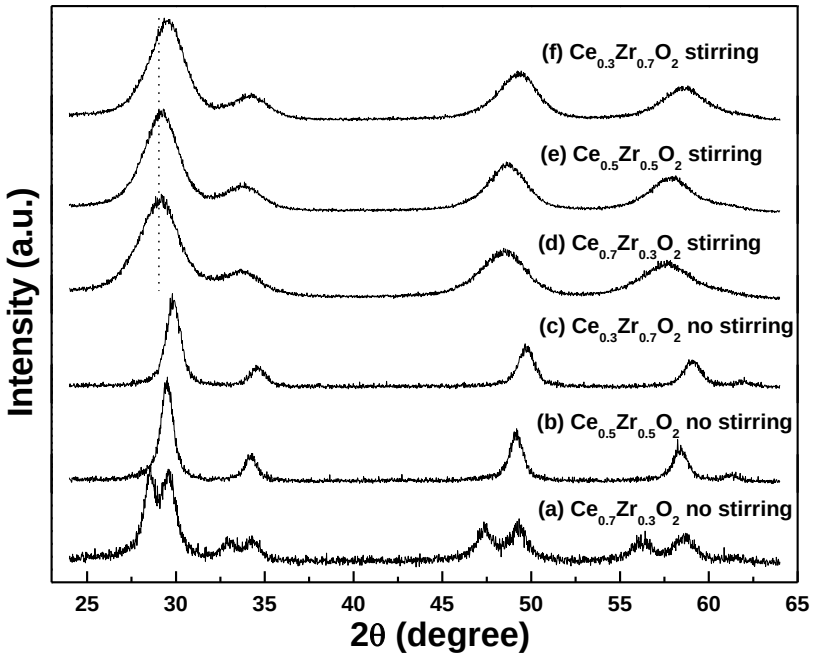

Figure 30: XRD patterns of $Ce_{0.3}Zr_{0.7}O_2$, $Ce_{0.5}Zr_{0.5}O_2$, and $Ce_{0.7}Zr_{0.3}O_2$ mixed oxides showing the effect of stirring treatment before hydrothermal reaction on the compositional homogeneity of final products.

To gain further insights into the role of the stirring on the synthetic process of CeO_2-ZrO_2 solid solutions, a possible formation mechanism of $Ce_xZr_{1-x}O_2$ ($0<x<1$) mixed oxides nanocrystals from metal nitrate solution and NaOH is proposed as follows: First, the hydrated metal ions are hydrolyzed to metal hydroxides (Step 1 and 2: $ZrO(OH)_2$ and $Ce(OH)_3$) when mixing metal nitrate with NaOH. The metal hydroxides are not stable under high pressure during the hydrothermal reaction at 150 ^oC. Then, metal hydroxides proceed to precipitate as metal oxides through dehydration and oxidation (Step 3).

$$ZrO(NO_3)_2 + 2NaOH \rightarrow 2NaNO_3 + ZrO(OH)_2 \quad (1)$$

$$Ce(NO_3)_3 + 3NaOH \rightarrow 3NaNO_3 + Ce(OH)_3 \qquad (2)$$

$$4(1-x)ZrO(OH)_2 + 4xCe(OH)_3 + xO_2 \xrightarrow{T,\ P} 4Ce_xZr_{1-x}O_2 + 2(x+2)H_2O \qquad (3)$$

It is interesting to compare the formation of Ce-rich ($Ce_{0.7}Zr_{0.3}O_2$) and Zr-rich ($Ce_{0.3}Zr_{0.7}O_2$) solid solutions from an aqueous solution. The observation shown in Figure 4 gives insight about the formation of the oxide solid solutions. For the unstirred samples, a compositionally homogeneous $Ce_{0.3}Zr_{0.7}O_2$ solid solution can form under hydrothermal reaction at 150 ^oC, but the phase separation occurred for the $Ce_{0.7}Zr_{0.3}O_2$ sample. This seems to indicate that high CeO_2 or $Ce(OH)_3$ concentration does not favor the formation of CeO_2-ZrO_2 solid solution. In other words, the result may suggest that ZrO_2 or $ZrO(OH)_2$ nuclei works as centers of solidification process, by Ce-rich component dissolving in Zr-rich component under hydrothermal reaction conditions. Without stirring, the solid solution process was limited, resulting in a phase separation for the high cerium concentration samples. When stirring was applied, the product obtained showed a compositional homogeneity for all three samples. This indicates that the stirring treatment promotes the "solid solution" formation, which could be due to the increased diffusion rate and collision between metal hydroxides nucleus by stirring.

This hypothesis seems to be supported by our TEM investigation, shown in Figure 5. Figure 5 shows the representative TEM images for the $Ce_{0.7}Zr_{0.3}O_2$, $Ce_{0.5}Zr_{0.5}O_2$, and $Ce_{0.3}Zr_{0.7}O_2$ nanocrystals prepared by hydrothermal reaction at 150 ^oC for 48 hrs without 40 mins pre-stirring in air. The $Ce_{0.5}Zr_{0.5}O_2$ and $Ce_{0.3}Zr_{0.7}O_2$ samples show uniform size and shapes of nanoparticles. The morphological heterogeneity was only found for the sample of $Ce_{0.7}Zr_{0.3}O_2$, with a mixed morphology of nanorods and

irregular shape nanoparticles. EDX analysis shows that the nanorods is a Ce-rich phase ($x>0.5$ in $Ce_xZr_{1-x}O_2$). Therefore an intimate and homogeneous contact of cerium and zirconium precursor is particularly important to form a homogeneous ceria zirconia solid solution, which is the reason we mixed all of solid solution precursors for 40 mins before the hydrothermal reactions in the systematic study of $Ce_xZr_{1-x}O_2$ ($0\leq x\leq 1$) (i.e., Figure 1, Figure 6 and Figure 7).

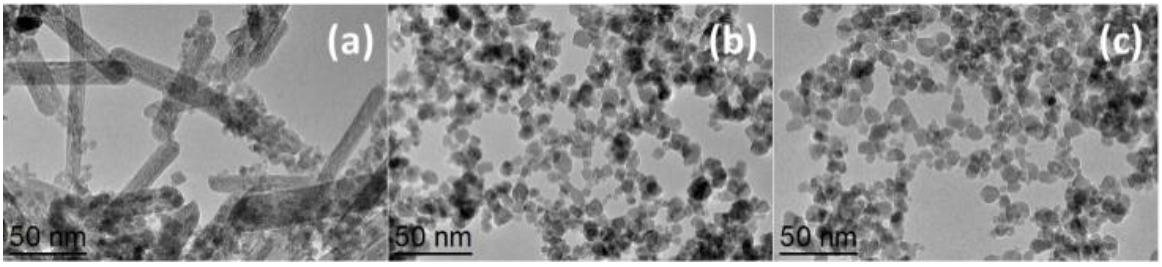

Figure 31: Representative TEM images of the $Ce_{0.7}Zr_{0.3}O_2$ (a), $Ce_{0.5}Zr_{0.5}O_2$ (b), and $Ce_{0.3}Zr_{0.7}O_2$ (c) nanocrystals prepared by hydrothermal reaction at 150 ^oC for 48 hrs without the 40-minute stirring treatment in air.

4.4.3 Raman spectroscopy study

The Raman spectra of $Ce_xZr_{1-x}O_2$ ($0\leq x\leq 1$) nanocrystals are compared in Figure 6. The Raman-active modes in pure CeO_2 are well characterized by the 458 and 605 cm^{-1} bands, and are attributed to a symmetrical stretching F_{2g} mode of the Ce-O8 vibrational unit. The Raman spectrum of pure monoclinic ZrO_2 exhibits ten prominent bands in the range of between 300 and 1000 cm^{-1}, including four major bands that are 347, 381, 476, and 614 cm^{-1}, and six weak bands at 306, 333, 504, 538, 558, and 631 cm^{-1}. The Raman bands at 306, 347, 476, 558, 631cm^{-1} are assigned to A_g mode, and the bands at 333, 381, 504, 538, 614 cm^{-1} are assigned to B_g mode in monoclinic ZrO_2 [18-19]. As the ZrO_2 concentration is increased from 0 to 1, the F_{2g} mode frequency exhibits a continuous shift

and approaches that of pure CeO_2. The vibration bands are increasingly broader as ZrO_2 composition increases in the $Ce_xZr_{1-x}O_2$ ($0 \leq x \leq 1$) nanocrystals. Raman spectroscopy has a high sensitivity to unit cell distortions and elemental coordination environments, and both ceria and ceria zirconia have been extensively characterized using this method [18-19]. Several researchers have employed Raman spectroscopy to study doped ceria/zirconia systems and it has been successfully used to determine the phase composition in the complex ceria zirconia system. Yashima et al. [14], for example, describe the phase diagram of the CeO_2-ZrO_2 system, determined from Raman and X-ray diffraction techniques in which cubic, monoclinic and tetragonal phases occur. Due to the size of the $Ce_xZr_{1-x}O_2$ ($0 \leq x \leq 1$) nanocrystals obtained, the bands are relatively broad in this study, however, on the other hand it may demonstrate the advantages of hydrothermal synthesis at such low temperature (150 ^oC) to prepare mixed oxides with superior compositional homogeneity.

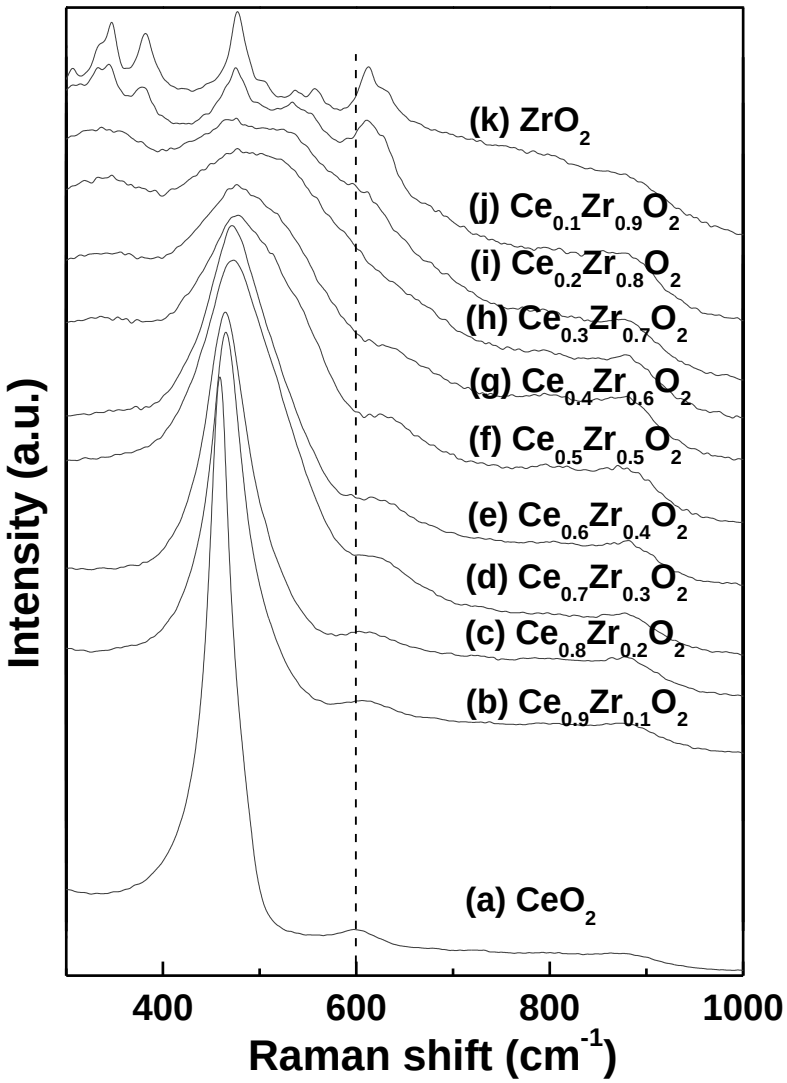

Figure 32: Raman spectra of $Ce_xZr_{1-x}O_2$ ($0 \leq x \leq 1$) nanocrystals.

4.4.4 H_2-Temperature programmed reduction (H_2-TPR)

Figure 7 shows H_2-TPR profiles of $Ce_xZr_{1-x}O_2$ ($0 \leq x \leq 1$) nanocrystals. In pure CeO_2, the H_2-TPR profile shows two major reduction peaks corresponding to the surface and bulk reductions, respectively, which are characteristics of reduction temperature and the distribution between the surface and bulk reduction percentage. The coordinately unsaturated surface capping oxygen ions can be easily removed in the low temperature region. However, bulk oxygen requires to be transported to the surface before their

reduction. Consequently, the bulk reduction takes place at higher temperature compared to the surface reduction. For pure ZrO_2 nanocrystal, the profile is relative flat, which indicates only a small quantity of H_2 was consumed or absorbed on pure ZrO_2.

Similar H_2-TPR results were obtained over $Ce_xZr_{1-x}O_2$ ($0<x<1$) mixed oxide nanocrystals. Unlike the two surface/bulk reduction peaks in pure CeO_2, only single H_2 consumption peak was observed for $Ce_xZr_{1-x}O_2$ ($0<x<1$) mixed oxides. This result clearly shows an improved low-temperature activity in $Ce_xZr_{1-x}O_2$ ($0<x<1$) compared to pure CeO_2. This is consistent with the literature that the reduction peak of CeO_2 shifted to lower temperature by zirconium addition [2]. One possible explanation for this is that oxygen defects are made in the CeO_2-ZrO_2 solid solution by the existence of zirconium and it is inferred that mobility of oxygen becomes higher, and then the rate of redox reaction becomes faster.

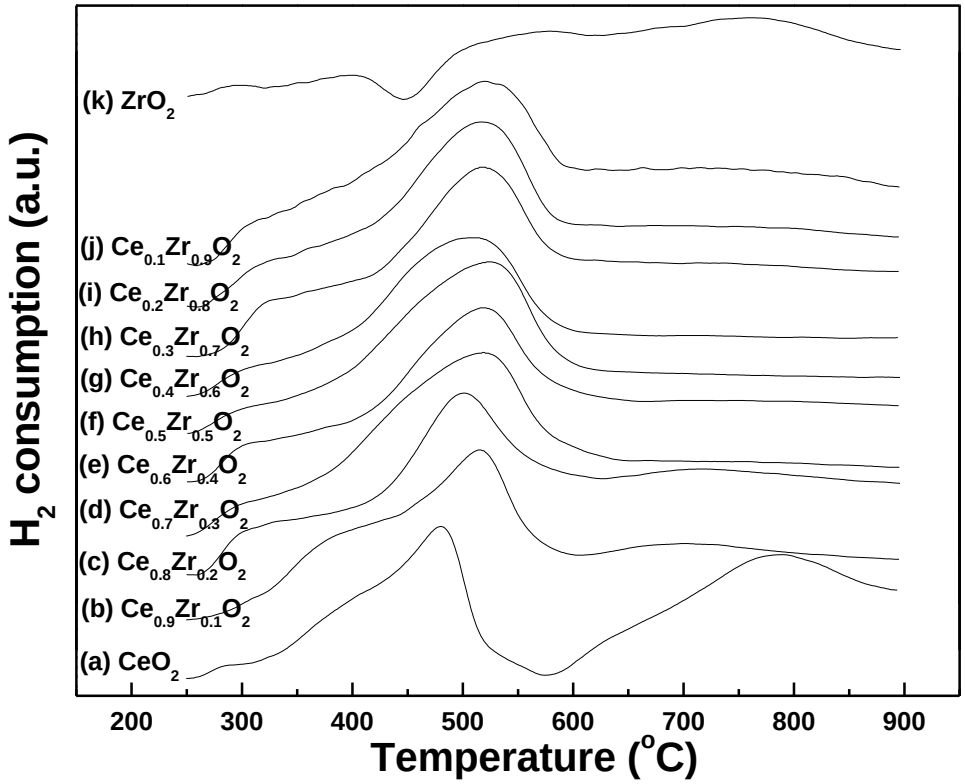

Figure 33: H_2-TPR profiles of $Ce_xZr_{1-x}O_2$ ($0 \le x \le 1$) nanocrystals

4.4.5 Thermal stability under reduction/oxidation conditions

Hydrothermal synthesis, which uses hot pressurized water for precipitation of oxides, is a low temperature and high pressure method. The reaction of the solid solution formation is not under a thermodynamic equilibrium condition, compared to the high temperature solid phase sintering method. In order to evaluate the thermal stability the nanoparticles obtained, Figure 8 shows the XRD patterns for the $Ce_{0.5}Zr_{0.5}O_2$ sample during the thermal treatments under oxidizing (in air) and reducing atmosphere ($5\%H_2/95\%N_2$) with an increasing temperature from 900^{o}C to 1400^{o}C. Under reducing atmosphere, at lower treatment temperatures (900^{o}C and 1000^{o}C), the XRD patterns shown in Figure 8 a and b exhibit all the characteristic reflections corresponding to the fluorite-type CeO_2 (JCPDS 34-0394), and the peaks grow narrower and sharper at higher temperatures, indicating crystallite size growth. As the temperature increased above 1100^{o}C, the extra diffraction peaks were observed suggesting that cation order occurs to form pyrochlore-type $Ce_2Zr_2O_{7+x}$ ($0 \leq x \leq 1$) phase, which is similar to our and others' observation [20-28]. Under oxidizing atmosphere, above 1200^{o}C, phase separation occur in which (200) (~32^o) and (220) (49^o) peak splitting can be found upon the formation of tetragonal phases. Figure 9 shows the schematic about the transformation from psudocubic to pyrochlore and the psudocubic to tetragonal structure under reduction and oxidation atmosphere, respectively.

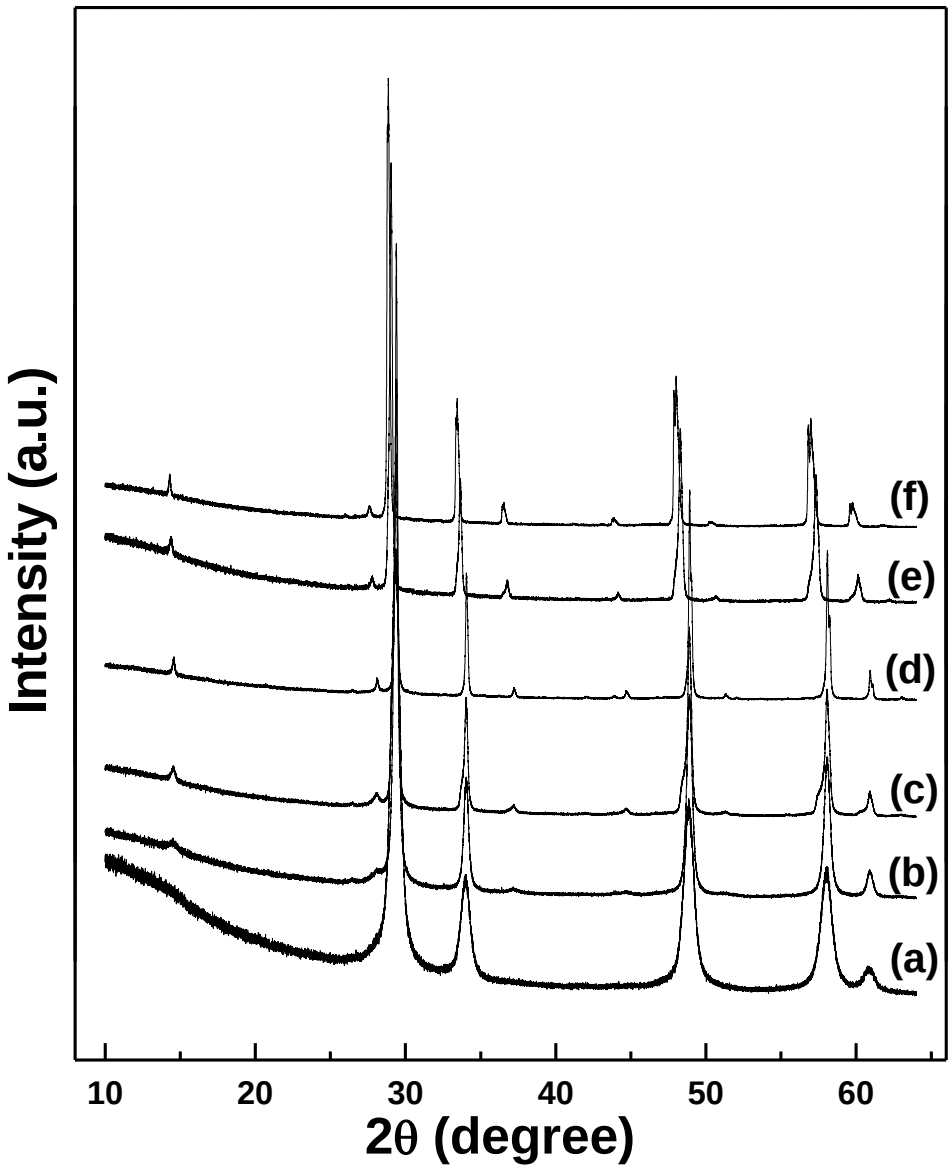

(A)

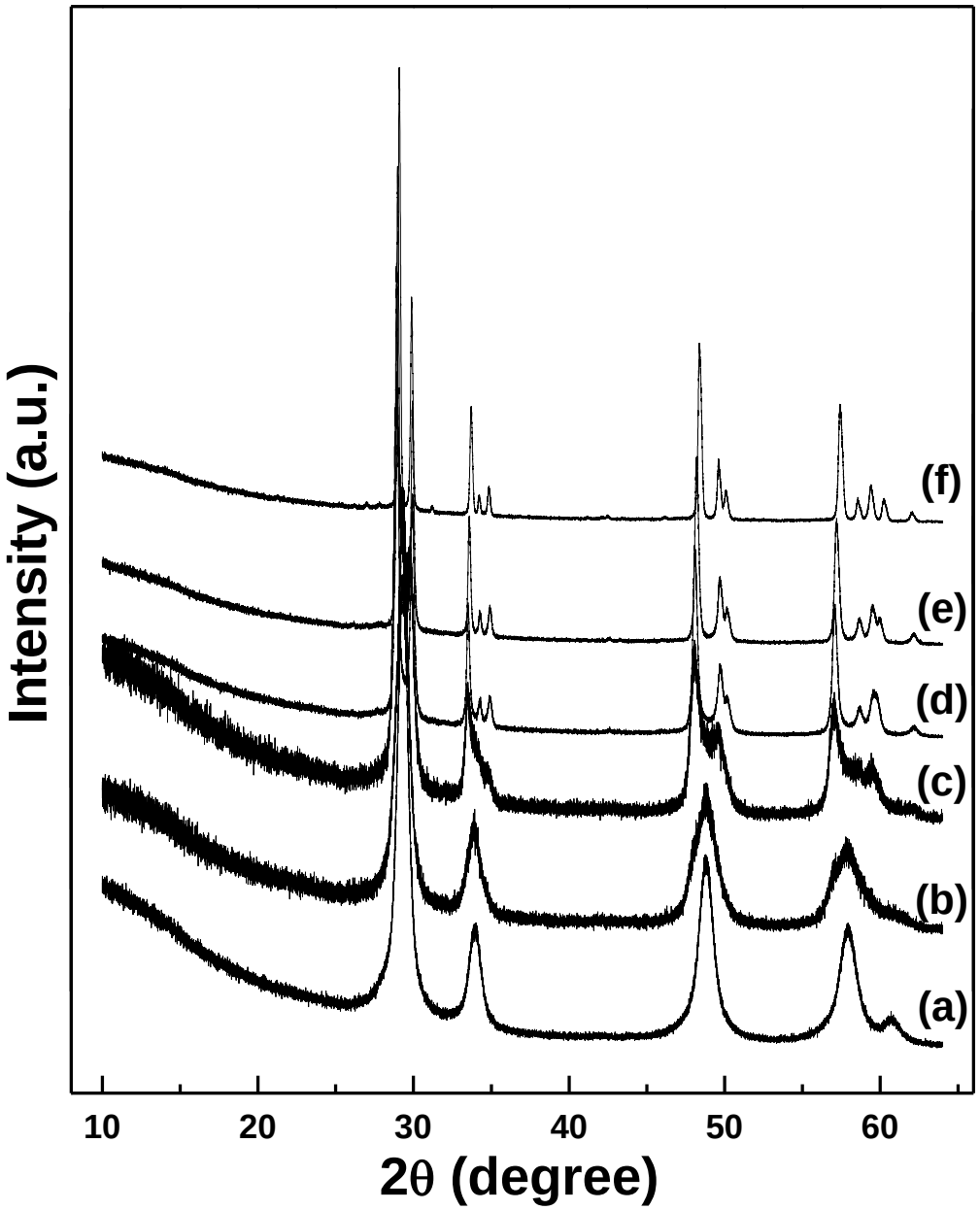

(B)

Figure 34: Effects of increasing thermal treatment temperature on the phase homogeneity of $Ce_{0.5}Zr_{0.5}O_2$ samples under oxidizing (A) and reducing atmosphere (B): (a) 900 ^oC; (b) 1000 ^oC; (c) 1100 ^oC; (d) 1200 ^oC; (e) 1300 ^oC; (f) 1400 ^oC.

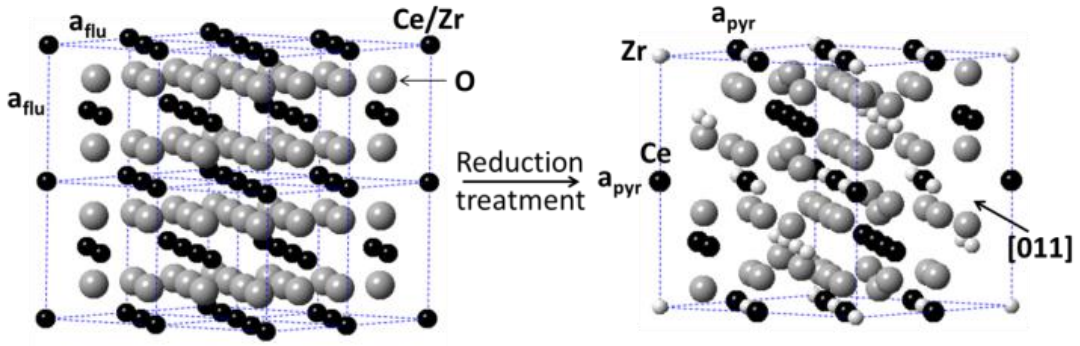

(a) under reducing atmosphere

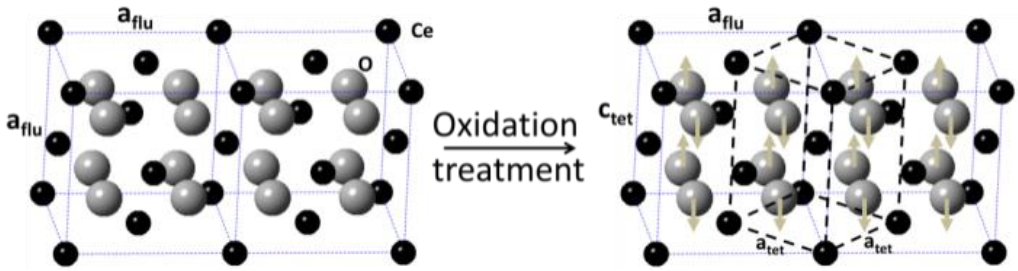

(b) under oxidizing atmosphere

Figure 35: Schematic of structural transformation in $Ce_{0.5}Zr_{0.5}O_2$ during high temperature thermal treatments under reducing and oxidizing atmospheres.

4.5 Conclusions

In summary, we have shown that hydrothermal synthesis is a facile one-step approach to prepared compositionally homogeneous $Ce_xZr_{1-x}O_2$ ($0 \leq x \leq 1$) nanocrystals, in which CeO_2-ZrO_2 mixed oxides present a superior low-temperature oxygen release capability compared to pure CeO_2. The synthesized $Ce_{0.5}Zr_{0.5}O_2$ shows good thermal stability up to 1000^{o}C under reducing and oxidizing atmosphere. Above 1000^{o}C, phase transformation occurs from psudocubic to cation ordered pyrochlore or tetragonal phase under reducing and oxidizing atmosphere, respectively. This method may be easily extended to other cerium-based mixed oxides or synthesis of analogous mixed oxides.

4.6 References

1. Trovarelli, A., *Catal. Rev. Sci. Eng.* **38(4)**, 439 (1996)
2. Kaspar, J., Fornasiero, P., Graziani, M., *Catal. Today*. **50(2)**, 285 (1999)
3. Shelef, M., McCabe, R.W., *Catal. Today*. **62**, 35 (2000)
4. Fornasiero, P., Balducci, G., DiMonte, R., Kaspar, J., Sergo, V., Gubitosa, G., Ferrero, A., Graziani, M., *J. Catal.* **164(1)**, 173 (1996)
5. Reddy, B.M., Khan, A., Yamada, Y., Kobayashi, T., Loridant, S., Volta, J.C., *J. Phys. Chem. B.* **107(22)**, 5162 (2003)
6. Casapu, M., Krocher, O., Elsener, M., *Appl. Catal. B-Environ.* **88(3-4)**, 413 (2008).
7. Tang, C.W., Kuo, C.C., Kuo, M.C., Wang, C.B., Chien, S.H., *Appl. Catal. A – General*, **309(1)**, 37 (2006)
8. Wang, Y., Zhu, A.M., Zhang, Y.Z., Au, C.T., Yang, X.F., Shi, C., *Appl. Catal. B-Environ.* **81(1-2)**, 141 (2008)
9. Letichevsky, S., Tellez, C.A., Avillez, R.R., Silva, M.I.P., Fraga, M.A, Appel ,L.G., *Appl. Catal. B-Environ.* **58(3-4)**, 203 (2005)
10. Rossignol, S., Madier, Y., Duprez, D., *Catal. Today.* **50**, (2) 261 (1999)
11. Alifanti, M., Baps, B., Blangenois, N., Naud, J., Grange, P., Delmon, B. *Chem. Mater.* **15**, (2) 395 (2003)
12. Suda, A., Kandori, T., Terao, N., Ukyo, Y., Sobukawa, H., Sugiura, M., *J. Mater. Sci. Lett.* **17**, 89 (1998)
13. Stark, W.J., Maciejewsk, M., Madler, L., Pratsinis, S.E., Baiker, A., *J. Catal.* **220**, (1) 35 (2003)

14. Yashima, M., Arashi, H., Kakihana, M., Yoshimura, M., *J. Am. Ceram. Soc.* **77,** (4) 1067 (1994)

15. Kang, Z.C., *J. Alloys Compd.,* **408-412**, 1103 (2006)

16. Choi, H.J., Moon, J., Shim, H.B., Han, K.S., Lee, E.G., Jung, K.D., *J. Am. Ceram. Soc.* **89,** 1, 343 (2006)

17. Wang, J., Ee, L.S., Ng, S.C., Chew, C.H., Gan, L.M., *Mater. Lett.* **30**, 119 (1997)

18. Siu, G.G., Stokes, M.J., Liu, Y., *Phys. Rev.*, **59, (4)** 3173 (1999)

19. Yashima, M., Takashina, H., Kakihana, M., Yoshimura, M., *J. Am. Ceram. Soc.* **77**, 1869 (1994)

20. Wang, R., Fang, M.H., *J. Mater. Chem.* **22**, 1770 (2012)

21. Montini, T., Bañares, M.A., Hickey, N., Di Monte R., Fornasiero, P., Kašpar, J., Graziani, M., *Phys. Chem. Chem. Phys.* **6**, 1 (2004)

22. Yeste, M.P., Hernandez, J.C., Trasobares, S., Bernal, S., Blanco, G., Calvino, J.J., Perez-Omil, J.A., Pintado, J.M. , *Chem. Mater.* **20**, (15) 5107 (2008)

23. Sasaki, T., Ukyo, Y., Kuroda, K., Arai, S., Saka, H., *J. Electron Micros.* **52**, (3) 309 (2003)

24. Sasaki, T., Ukyo, Y., Kuroda, K., Arai, S., Muto, S., Saka, H., *J. Ceram. Soc. Jap.* **112**, (8) 440 (2004)

25. Sasaki, T., Ukyo, Y., Suda, A., Sugiura, M., Kuroda, K., Arai, S., Saka, H., *J. Ceram. Soc. Jap.***111**, (6) 382 (2003)

26. Suda, A., Ukyo, Y., Yamamura, K., Sobukawa, H., Sasaki, T., Nagai, Y., Tanabe, T., Sugiura, M., *J. Ceram. Soc. Jap.* **112**, (11) 586 (2004)

27. Arai, S., Muto, S., Sasaki, T., Tatsumi, K., Ukyo, Y., Kuroda, K., Saka, H., *Solid State Commun.***135**, 664. (2005)

28. Yashima, M., Sekikawa, T., Sato, S., Nakano, H., Omoto, K., *Cryst. Growth Des.* **13**, (2) 829 (2013)

Chapter 5 Catalytic activity of shape-controlled ceria-supported Pt and Au nanocatalysts

5.1 Introduction

Ceria continues to be of interest in material science and engineering due to its widespread applications in the fields of optical films, polishing materials, gas sensors, fuel cells and, more importantly, in the field of three-way catalysis and green chemistry [1-2]. An increased need for a global green economy in the energy and transportation sectors has made these last two applications particularly relevant hence leading to the adoption and strict enforcement of energy policies to reduce greenhouse gas emissions. In turn, demand for modern technologies and devices which can efficiently lower the levels of pollutant gases and/or convert them to environmentally harmless products has risen. Good examples of such devices are the three-way catalytic convertors that rapidly convert CO and C_xH_y to H_2O and CO_2 and simultaneously reduce NO_x to molecular nitrogen even in highly fluctuating emission concentrations. However, in the absence of dopants or noble metal catalysts, the redox functionality of CeO_2 along with its ability to act as an oxygen storage material is constrained to a narrow range of temperatures (~ 400-800 ^oC). Not only that, but its performance drastically falls at temperatures below 300 ^oC due to lack of sufficient thermal energy to remove oxygen ions from the ceria lattice [1-7]. In this chapter, we demonstrate morphologically dependent properties of ceria through an analysis of ceria nanorods and nanocubes. These properties include oxygen storage capacity, reduction temperature, oxygen vacancies, and sample color. In addition, the effect of impregnating these rods and cubes with gold and platinum has been explored with particular emphasis on improved reductive activity at low temperatures.

5.2 Experimental

The CeO_2 nanorods and nanocubes were synthesized by using a facile hydrothermal method at 90 ^oC and 170 ^oC respectively for 48 hours. In a typical setting, 110 mL of 0.1 M $Ce(NO_3)_3$ solution were poured into a 200 mL Teflon lined autoclave at room temperature followed by 10 mL of 6 M NaOH with slight stirring before being transferred into a programmable box furnace where the reactions were performed. After the hydrothermal reactions had been carried out at the respective temperatures, the precipitates were recovered by gravity filtration and washed thoroughly using distilled water and absolute ethanol followed by low-temperature drying in a box furnace. 1 wt. % platinum and 1 wt. % gold were now impregnated on the synthesized nanosupport material using platinum (IV) chloride and gold (III) chloride aqueous solutions respectively. After impregnation, the samples were calcined at 400 ^oC for 5 hours in air and thereafter reduced at 400 ^oC for 5 hours in 5% H_2 gas.

5.3 Characterization

Characterization techniques that were employed in this study included the following: Powder X-ray diffraction (XRD) was employed in collecting crystallographic information about the synthesized samples and was performed using a Rigaku Miniflex II, applying a scanning range of 10^o to 90^o (2θ), and a sampling width of 0.020^o with a scanning speed of 0.5 ^{o}/min. On the other side, Raman Spectroscopy was conducted at room temperature using a *Kaiser* Optical Systems *RXNI-785* that was equipped with a thermoelectrically cooled diode laser source that fluorescenced at a wavelength of 785 nm and a power of 400 mW. The spectrometer also was equipped with a CCD detector that was maintained at -40 ^oC in order to lower its background levels. An exposure time

of 10 sec. was used during data collection. TEM data was collected using a JEOL2100 instrument that was equipped with an EDAX detector and an annular dark-field detector at an acceleration voltage of 200 kV. In a typical sample preparation procedure, freshly prepared CeO_2 precipitate was lightly agitated for 30 seconds after which a holey carbon grid was dipped into the reaction mixture for two seconds before it was removed and dried. Finally, BET-surface area and Hydrogen Temperature Programmed Reduction (H_2-TPR) were performed using a Micromeritics AutoChem™ II 2920.

5.4 Results and Discussion

5.4.1 Pure Ceria

Phase purity of the CeO_2 samples was quantified using Powder X-ray diffraction (as mentioned in the experimental section). As shown in Figure 1, all diffraction peaks were indexed to the cubic fluorite structure (JCPDS card number 34-0394) confirming that the two samples were pure CeO_2. The diffraction peaks corresponding to nanocubes were slightly shifted to higher angles while those corresponding to nanorods were slightly shifted to lower angles (this observation is highlighted by the green dotted lines in Figure 1 below). This phenomenon indicated that the crystal planes of the nanocubes had shorter d-spacing and a smaller lattice constant while those of nanorods had a larger d-spacing and larger a lattice constant. To proof this mathematically, the Shrerrer equation was used to estimate the particle size of the samples where nanorods (CeO_2-90 ^oC) were found to have a size of 8.2 nm while nanocubes were found to have a size of 20.3 nm. On the other size, the (hkl) miller indices and d-spacing information were used to compute the lattice constants of the samples. Calculations revealed that nanorods and nanocubes had lattice constants of 5.429 Å and 5.413 Å respectively, meaning that the lattice constant

decreased with increasing particle size and as it will be discussed shortly, it was also believed that lattice constant changes were also attributable to lattice strain that must have been caused by the formation of Ce^{3+} from the induction of both surface and lattice oxygen vacancies [6]. The differences in particle size, morphology and lattice constants were primarily attributed to the hydrothermal reaction parameters that included synthesis temperature and solvent pressure [7]. XRD peak broadening and intensities were also found to be in good agreement with the above mentioned calculations. It is for the same reasons that a closer look at the data reveals that the (331), (420) and (222) diffractions peaks corresponding to nanorods were poorly resolved as compared to those of nanocubes. In the overall, it was concluded that crystallinity and particle size of the samples played a major role in determining the shape, position and intensities of the XRD peaks. Table 1 below gives a summary of how the particle sizes of the two samples varied with their lattice constants and BET surface area. [8-9].

Table 4: Particle size and lattice constant data for pure ceria samples

Sample Identity	Particle Size (nm)	Lattice Constant (Å)	BET Surface Area
CeO_2-90^oC	8.246	5.429	79
CeO_2-170^oC	20.344	5.413	38

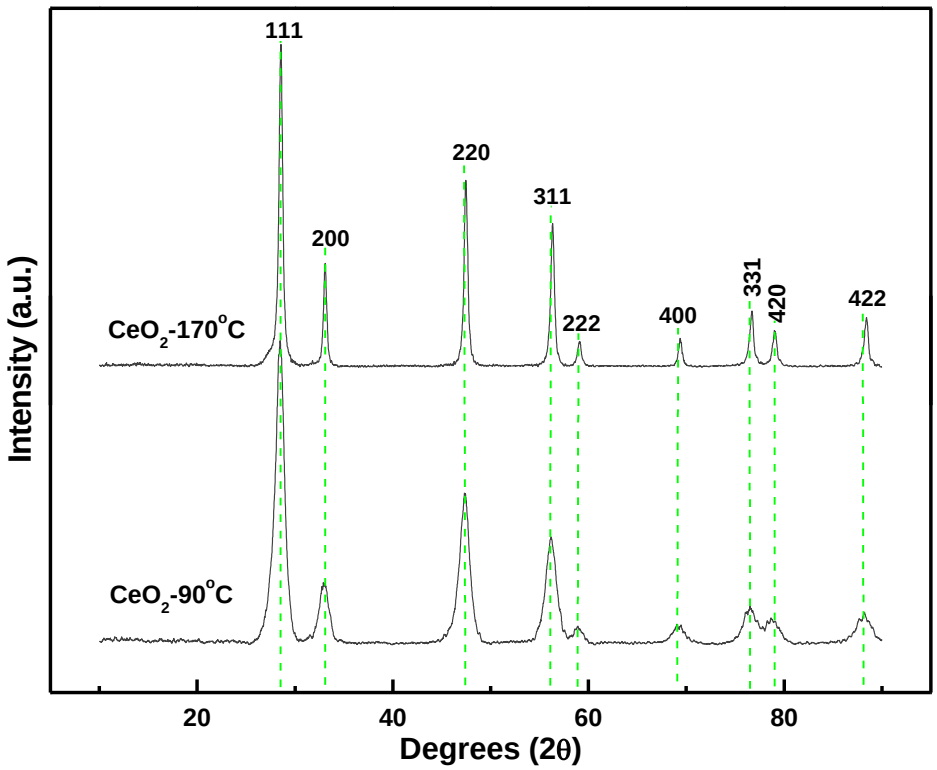

Figure 36: Powder XRD profiles for pure CeO_2 samples. The green dotted lines were included in order to aid in visualizing peak shifting.

As shown in Figure 2, the nano-powders of the two samples assumed different colors regardless of the fact that they had been synthesized in the same manner and belonged to the same chemical composition. This observation was attributed to changes in the unit cell volume (due to lattice constant variations), crystal size, shape and morphology. This phenomenon (as was described by other research groups) is referred to as the Localized Surface Plasmon Resonance (LSPR) and becomes more pronounced with decreasing particle size. As indicated in the schematic below, the color of ceria nanorods turned out to be yellow while that of nanocubes was between beige and light beige. It was therefore concluded that cerium oxide nanorods of high oxygen vacancy concentration and rough surface morphologies (as will be discussed in the Raman Spec.

and TEM sections) would assume a yellow color while smooth surfaced and highly crystalline nanocubes would assume a beige-light to beige color. This observation was also consistent with other CeO_2 studies that were conducted in our group but not mentioned in this report [10-12].

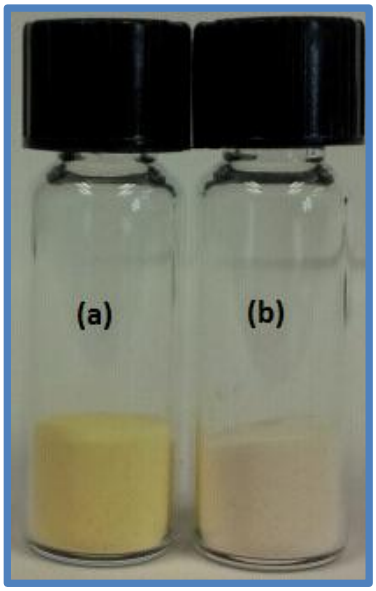

Figure 37: Nanopowders for (a) nanorods and (b) nanocubes.

Figure 3 shows the Raman spectra of pure Ceria samples. The 1st order scattering peaks that appear at 454 cm^{-1} and 464 cm^{-1} were attributed to the symmetric vibrations of the F2g modes of the CeO_2 while the low intensity 2nd order scattering peaks that appear at 600 cm^{-1} and 726 cm^{-1} were associated to the extrinsic oxygen vacancies that were present in the samples. It is important to note that the scattering band that appeared at 726 cm^{-1} was of comparatively lower intensity than the one that appeared at 600 cm^{-1}, implying that the ceria nanorods had a higher oxygen vacancy concentration per unit cell volume compared to the nanocubes. Peak shifting was strongly attributed to particle size and lattice constant strain. We concluded that the main reasons behind peak broadening

and asymmetry of the low energy scattering band that occurred at 454 cm^{-1} included the nano-size effect, lattice strain and higher oxygen vacancies [13-16].

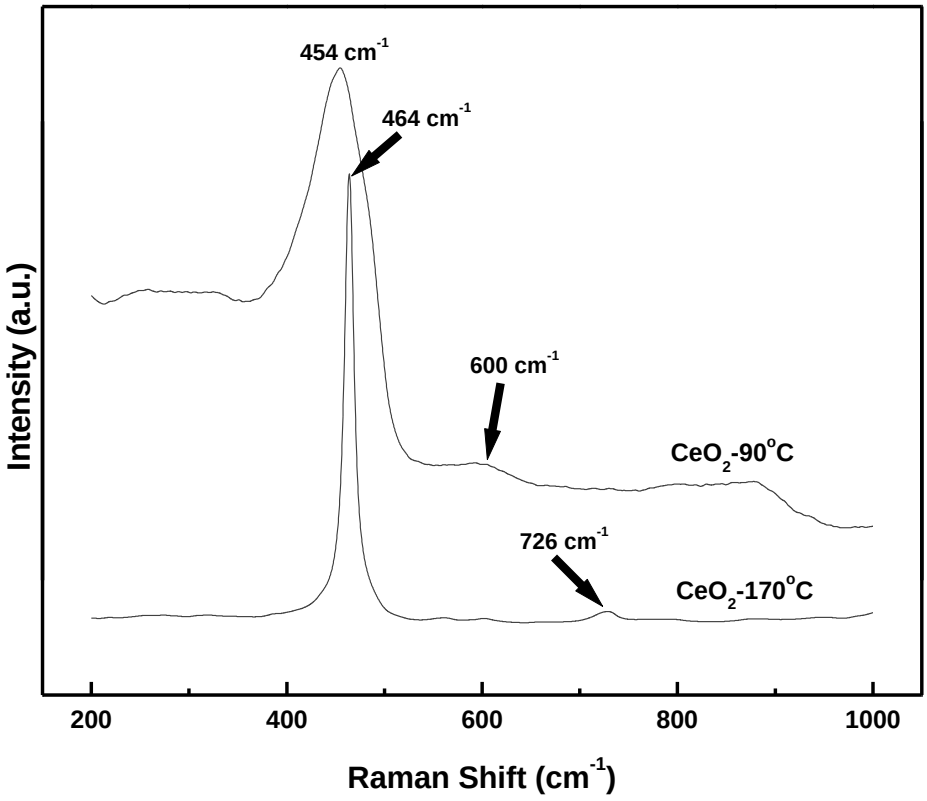

Figure 38: Raman spectroscopy data for pure ceria samples

Figure 4 is a compilation of low magnification TEM images of the CeO_2 samples that have been discussed above. From the images, it is clear that the CeO_2-90^oC sample had a nanorod morphology while the other sample had a nanocube morphology. Nanoparticles in both samples were well dispersed with negligible agglomeration. A close inspection of Figures 4 and 6 shows that the nanocubes were highly isotropic and single crystals of roughly 20 nm in length, while the nanorods were made of multiple (small) crystals that were randomly oriented with reference with each other and with a

total length of roughly 50nm and a width of less than 5 nm. It was believed that the nanorods were anisotropic especially given the facts that they had a rough surface and were composed of multiple small crystals. It is paramount to note that the crystal size and dispersion of the two samples were consistent with the BET surface area measurements as was shown in Table 1 above [17-18].

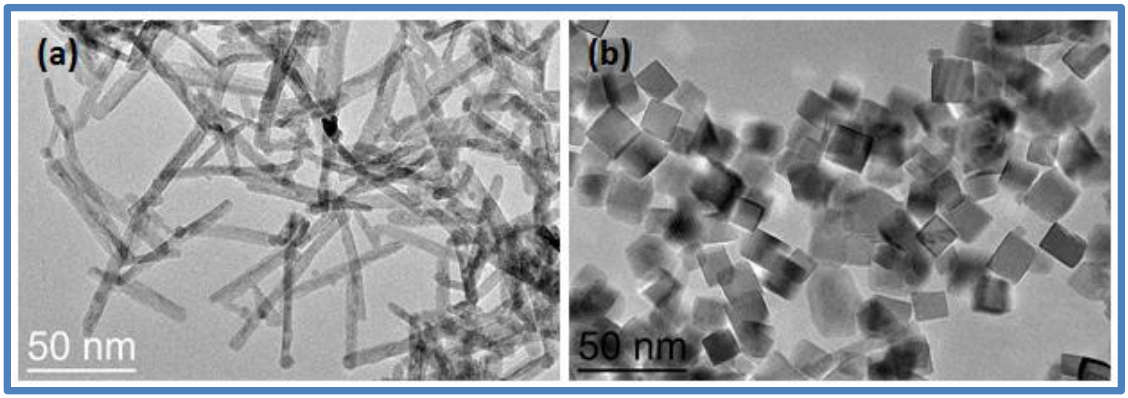

Figure 39: Low magnification TEM images of pure ceria samples (a) CeO_2-90 ^oC, (b) CeO_2-170 ^oC.

Figure 5 represents the H_2-TPR profiles for the two pure ceria samples. As can be observed from the data, ceria nanords were characterized by three distinct reduction bands; the reduction bands that occurred at 56.88 ^oC and 476.45 ^oC represented the surface and subsurface oxygen reduction while the intermediate intensity peak that occurred at 775.40 ^oC represented bulk or lattice oxygen reduction. Ceria nanocubes on the other hand were characterized by two overlapped low intensity surface reduction bands at 396.53 ^oC and 500.53 ^oC and a higher temperature bulk reduction peak at 784.75 ^oC.

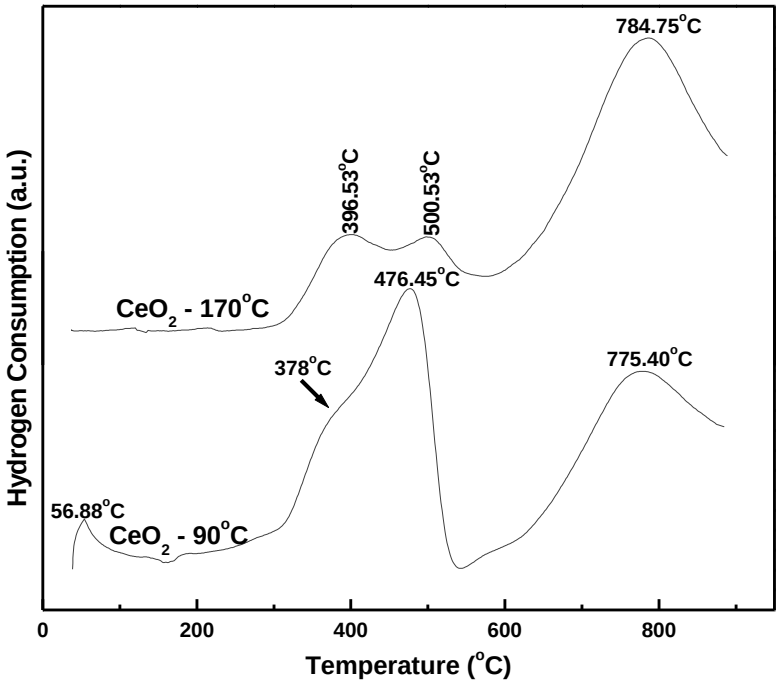

Figure 40: TPR profiles for the nanorods and nanocubes.

Qualitatively speaking, ceria nanorods had higher low temperature activity as compared to nanocubes based on the intensities of the surface reduction bands of the two samples. This was even more evidenced by the fact that nanorods showed a low temperature reduction band at 56.88 ^{o}C while nanocubes did not show any signs of getting reduced between room temperature and 350 ^{o}C. It was concluded that nanorods required the least amount of activation energy in order to donate surface oxygen. As far as the extent of reducibility of the two samples at different temperatures was concerned, it is clear from the data that nanorods had higher surface reducibility and lower bulk reducibility while the nanocubes had lower surface reducibility and higher bulk reducibility. These observations were attributed to the fact that nanorods had higher dispersion with respect to the number of atoms that were exposed to the surface, while

nanocubes has lower dispersion because most of their atoms were encapsulated in the bulk part of the nanocrystals. Another major reason for this observation was the fact that nanorods had more crystallographic facets exposed on their surfaces hence having higher chances of having oxygen terminated facets as compared to the nanocubes. Theoretical studies have shown that the oxygen vacancy formation energy for different CeO_2 surfaces follows the {110} < {100} < {111} order. In order to determine if this theory was consistent with our data, high resolution TEM analyses were performed on the two samples as a means of investigating which crystallographic facets were exposed on the different morphologies. After carrying out the analyses, we found that out that our H_2-TPR data was consistent with theoretical calculations because as it can be seen from Figure 5 below, nanorods were {200},{220}, and {111} terminated while nanocubes were {100} and {111} [19-20].

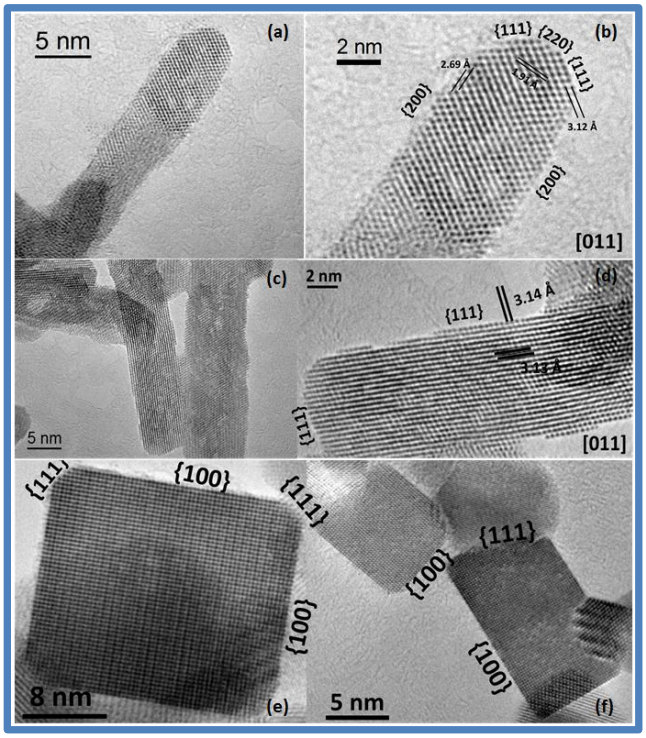

Figure 41: HRTEM images for ceria nanorods and nanocubes

Oxygen Storage Capacity (OSC) estimations were carried out using H_2-TPR peak area to mass ratios calculations. A constant mass of 0.810 g CeO_2 naorods and nanocubes was used during H_2-TPR measurements while the total peak areas corresponding to nanorods and nanocubes were calculated to be 4.084 and 5.8825 respectively. From these data, it was concluded that CeO_2 nanocubes had higher oxygen storage capacity compared to CeO_2 nanorods, based on the fact the nanocubes consumed more hydrogen gas during H_2-TPR experiments regardless of the fact that the sample masses had been maintained constant. This observation was in agreement with other research findings that were published by Hao-Xin Mai and his co-researches. Comparison of Figure 5 and Table 1 indicates clearly that the intensities of the surface reduction bands of the samples were directly correlated to their BET surface area. This interesting phenomenon was attributed to the tendency of higher surface area species to have more lattice edges and corners that might trigger the formation of higher concentrations of surface, lattice, line and plane defects hence causing a lowering of the oxygen vacancy formation energy and leading to an improved oxygen mobility in the materials [2,21] . In order to theoretically correlate the low temperature reducibility and of the CeO_2 nanorods and nanocubes to their exposed crystallographic facets, we constructed theoretical models of CeO_2 nanorods and nanocubes that showed different growth orientations in order to understanding which crystallographic facets could have been oxygen or cerium terminated considering that oxygen terminated facets would theoretically require less amount of activation energy to donate oxygen as compared of cerium terminated facets. Figure 7 shows different growth orientations of CeO_2 nanorods.

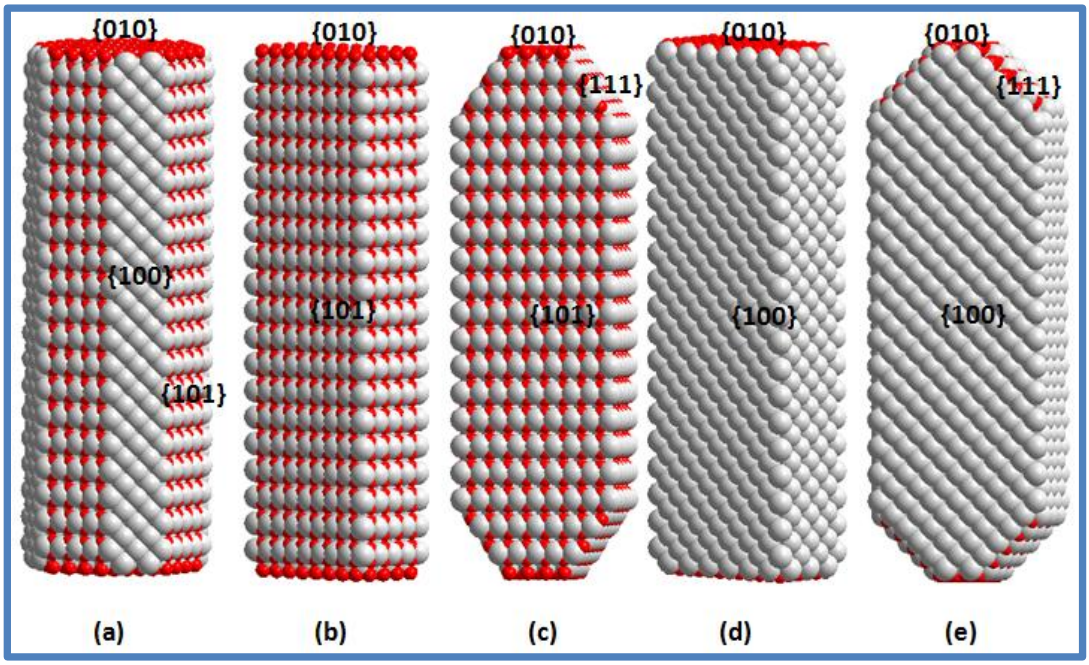

Figure 42: Different growth orientations of CeO_2 nanorods. The red balls represent oxygen while the white ones represent cerium.

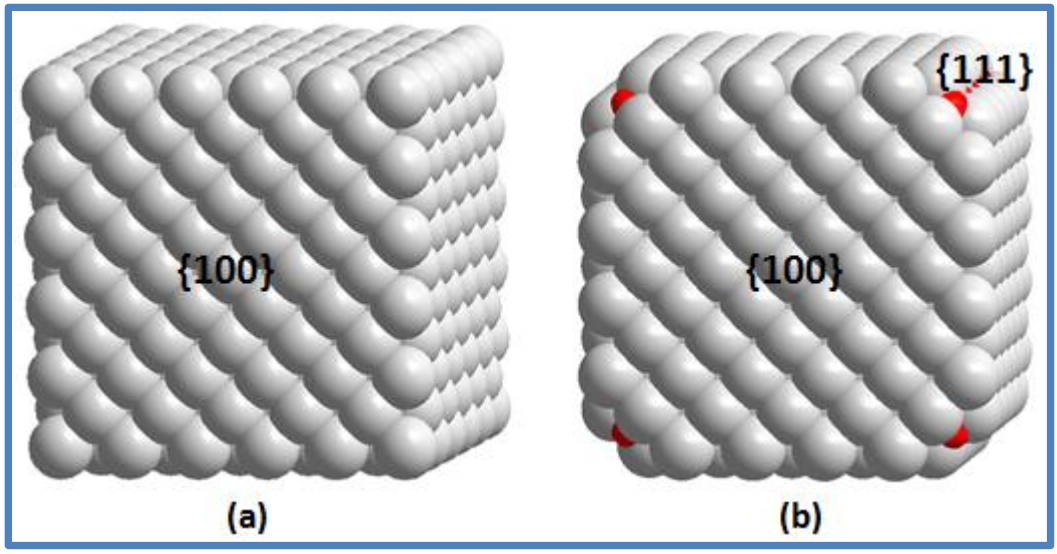

Figure 43: Different growth orientations of CeO_2 nanocubes. The red atoms represent oxygen while the white ones represent cerium.

5.4.2 Noble Metal-Cerium nanocomposites

Figure 9 shows the XRD data for the ceria-noble metal nanocomposites. From our calculations, it was found that Pt-Ceria nanorods and the Pt-Ceria nanocubes had particle sizes of 9.5 nm and 18.9 nm respectively, with lattice constants of 5.430 Å and 5.421 Å respectively while the Au-Ceria nanorods and Au-Ceria nanocubes had particle sizes of 8.860 nm and 20.33 nm with lattice constants of 5.424 Å and 5.420 Å respectively. From this crystallographic information, it was noted that lattice constant shrinking occurred with increasing particle size that must have led to a decrease in oxygen vacancies per unit cell. The same trend was observed in pure Ceria samples as was discussed in the Raman spectroscopy section [22]. Another interesting observation that we noted was that the incorporation of noble metal nanoparticles on the surface of CeO_2 nanocrystals significantly suppressed their growth during thermal treatment. This was evidenced by the fact that the particle sizes of pure CeO_2 that had been thermal-treated at 300 ^oC for 5 hours were very close to the size of the noble metal-CeO_2 nanocomposites regardless of the fact that the nanocomposites had been thermal treated at 400 ^oC for a total of 10 hours (during calcination and reduction processes). Almost unnoticeable peaks corresponding to the (111), (220) and (220) Au facets were observed on the CeO_2-170 ^oC/Au nanocomposite while CeO_2-90 ^oC/Au sample only showed a (111) Au peak. Pt peaks on the other side were not observed at all on the two Pt-CeO_2 nanocomposites meaning that gold nanoparticles on CeO_2 nanoparticles had a lower dispersion and larger particle sizes while Pt nanoparticles were atomically dispersed on the CeO_2 nanoparticles. [7, 13, 23, 31].

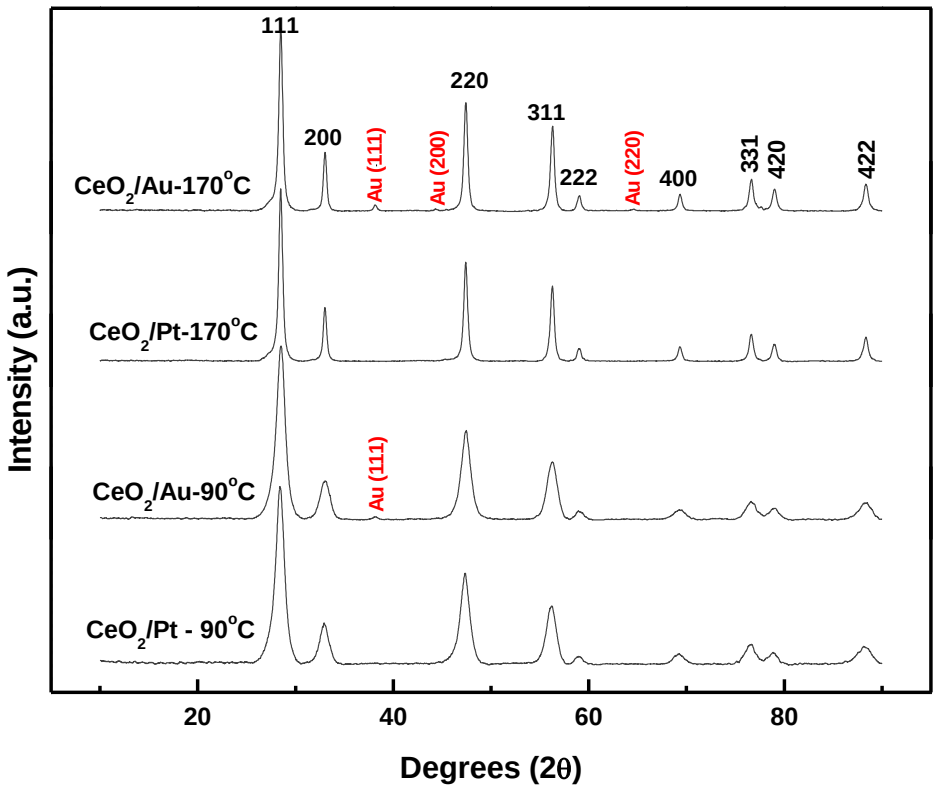

Figure 44: XRD data for CeO_2-Noble metal nanocomposites.

Figures 10 and 11 are comparisons of pure ceria and metal-impregnated ceria nanorods and nanocubes. An inspection of the two sets of data shows that the diffraction profiles of both ceria and metal-ceria nanocomposites for both nanorods and nanocubes occurred at almost the same angles with very negligible peak shifting and were of the same intensities due to their closeness in particle size and crystallinity [7, 23, 28, 31].

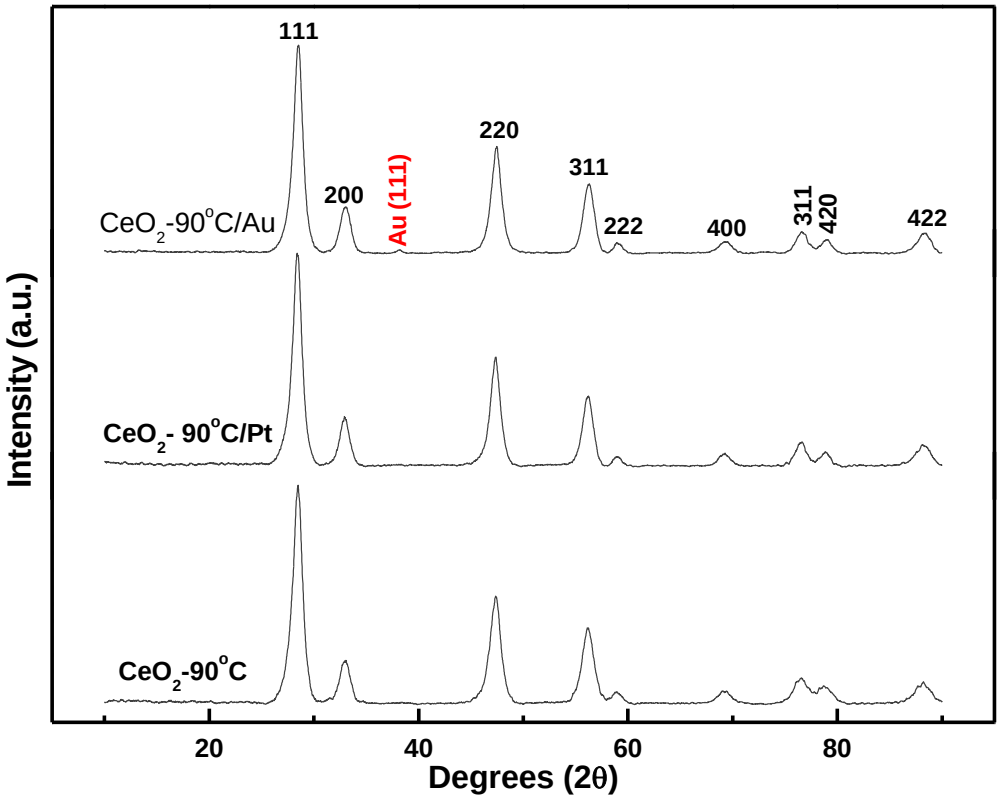

Figure 45: Comparison of the XRD data for pure ceria nanorods and metal impregnated ceria nanorods.

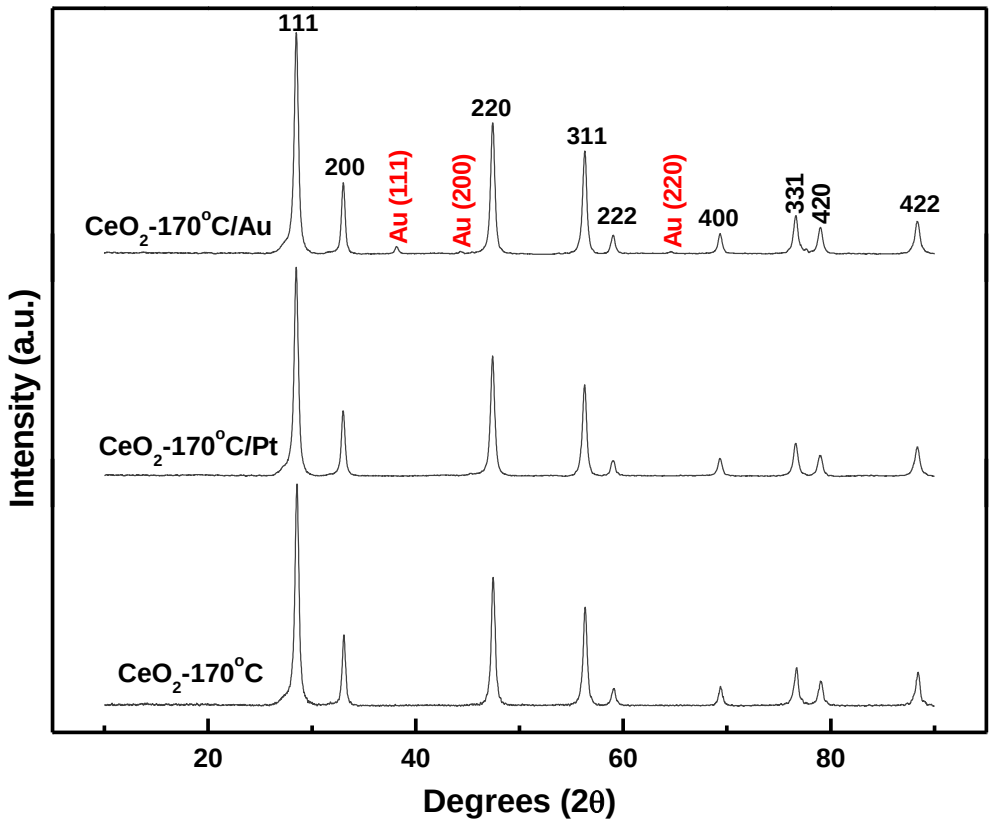

Figure 46: Comparison of the XRD data for pure ceria nanocubes and metal impregnated ceria nanocubes.

Figure 12 is a compilation of the H_2-TPR data for the six samples that have been discussed above (profiles corresponding to pure CeO_2 nanorods and nanocubes were only included here for comparison purposes only). It is paramount to mention in advance that the main focus of this study was to master and compare the surface and bulk reduction temperatures of the pure and noble metal impregnated CeO_2 nanoparticles with key emphasis on drawing solid conclusions concerning their low temperature activity, reducibility, and the effect of shape and size on their catalytic activity. The ultimate goal of the study was to determine which between the two noble metals (Pt and Au) showed a higher catalytic activity in the chemical oxidation of molecular hydrogen. As it will also

be noted from the discussion, the oxygen storage capacity of the materials was another important concern in the study. Qualitative inspection of Figure 12 indicates clearly that the intensities of the surface reduction bands of all the metal-impregnated ceria samples were directly correlated to their BET surface area. This trend was also seen in pure CeO_2 samples as discussed earlier and was attributed to the fact that high surface area species must have had more crystal defects, corners and edges hence having more active sites on their surface as compared to the low surface area species [2-5, 7, 21-22].

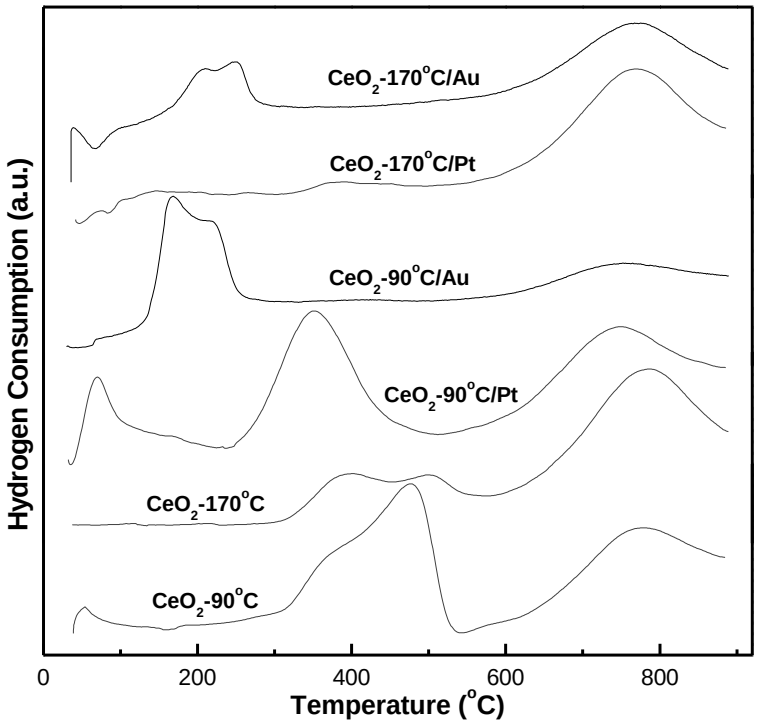

Figure 47: TPR data for pure and metal-impregnated ceria.

Another interesting observation that is clear from the data is that the bulk reduction bands corresponding to the metal-impregnated ceria nanocomposites occurred almost at the same positions where the bulk reduction bands of pure ceria occurred

implying that the activity of the noble metal nanoparticles was only beneficial during surface oxygen reduction but not during the lattice or bulk oxygen reduction of the materials. Lastly, it was noted that the intensities of the surface reduction bands of both pure and metal impregnated nanorods were higher than those of bulk reduction while for pure and metal-impregnated nanocubes; surface reduction band intensities seemed to be lower than those of bulk reduction [17, 24-25, 26]. In order to exhaustively analyze the above presented H_2-TPR data with regards to low temperature activity and oxygen storage capacity and to give specific reasons as to why some of the above mentioned observations were noted, discussions were narrowed down to three major effects that were of interest in this study.

5.4.2.1 The effect of using different CeO_2 morphologies as support for the same noble metal catalyst

(i) CeO_2 Nanorods

The figure below compares the surface and bulk reduction bands of pure ceria nanorods with those of Pt, and Au-impregnated CeO_2 nanorods. As it can be seen from the data, both pure CeO_2 and Pt-CeO_2 nanorods nanocomposites were characterized by three distinct reduction regions, with the first and second regions occurring at temperatures <100 ^oC and between 300^oC-500 ^oC respectively. These two regions were considered to represent the surface oxygen reduction while the third region that occurred between 740 ^oC to 780 ^oC was considered to represent the lattice oxygen reduction. On the other side, the Au-ceria nanorods nanocomposite was characterized by two major reduction regions with the surface reduction band occurring at 166.89 ^oC with a shoulder at 225.54 ^oC and the bulk reduction band occurring at 753.35 ^oC. Generally speaking, Pt-

CeO_2 nanorods nanocomposite had higher activity at less than 100 ^oC and had an improved low-temperature surface reduction as compared to the pure ceria nanorods. This can be confirmed by noting that the surface reduction band corresponding to the Pt-CeO_2 nanocomposite appeared 120 ^oC below the surface reduction band of pure ceria [17, 27, 31].

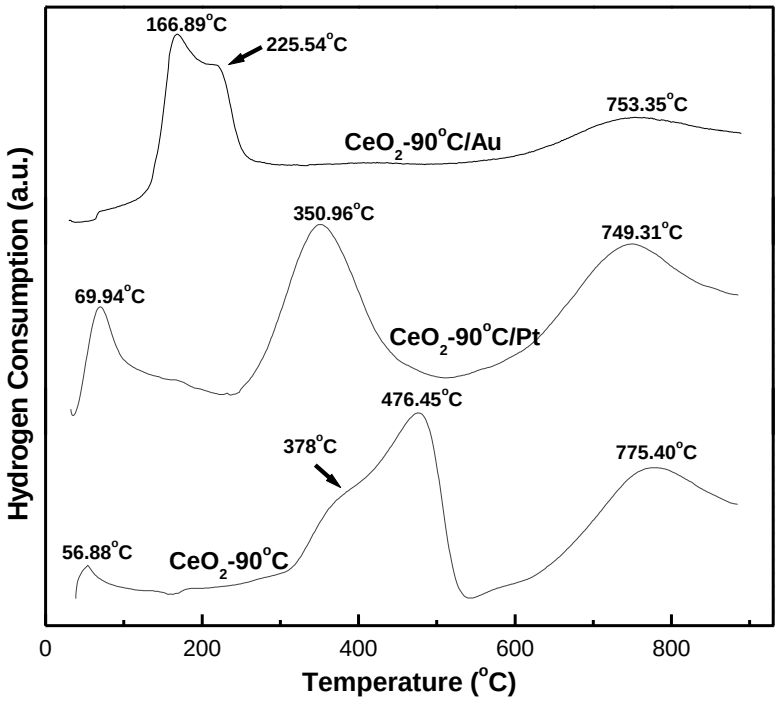

Figure 48: Comparison of pure ceria nanorods with Pt-CeO_2 nanorods and Au-CeO_2 nanorods

The ability of the Pt-CeO_2 nanorods to be reduced at <100 ^oC with a higher intensity as compared to pure ceria nanorods was particularly considered interesting and of great significance in the catalytic oxidation of molecular hydrogen at low temperatures. It was concluded that the incorporation of Pt nanoparticles on the surface of ceria nanorods improves their intrinsic capability to donate oxygen at very low

temperatures. This assumption was evidenced by considering that the reduction band that occurred at 69.94 ^{o}C was of a higher intensity as compared that the one that occurred at 56.88 ^{o}C. From our analysis, we also concluded that both Pt and Au nanoparticles helped in lowering the surface reduction temperature of pure ceria nanorods, with Pt being a better catalyst for extremely low temperature hydrogen oxidation. Au on the other side was noted to a have better temperature selectivity compared to Pt based on the fact that the temperature spread on the reduction bands of Au-ceria nanorods was smaller compared to the same in the reduction bands of Pt-ceria nanorods [17, 27, 31].

(ii) CeO_2 Nanocubes

Figure 14 below compares the surface and bulk reduction bands of pure ceria nanocubes with those of Pt, and Au-impregnated CeO_2 nanocubes. From the data, it is evident that both pure CeO_2 and Pt-CeO_2 nanorods nanocomposites were characterized by two distinct reduction regions, with the first one occurring between 350 ^{o}C-550 ^{o}C (surface reduction) and the second one occurring between 760 ^{o}C to 780 ^{o}C (bulk reduction). On the other side, the Au-CeO_2 nanocubes were characterized by three distinct reduction regions where the first two representing surface oxygen reduction occurred at 39.33 ^{o}C and 250 ^{o}C with a shoulder at 205 ^{o}C, while the high temperature bulk reduction peak occurred at 770 ^{o}C. It is easy to note from the data that Pt-Ceria nanocubes were reduced slowly and continuously from room temperature until a very low intensity peak occurred at 383 ^{o}C while the high intensity band occurred at 769 ^{o}C. According to the data, Au was more temperature selective than Pt and that Au turned out to be a stronger catalyst on CeO_2 nanocubes than Pt. This was confirmed by noting that the intensity of the reduction bands corresponding to surface reduction on Au-CeO_2

nanocubes were higher than the one that corresponded to the surface reduction of Pt-CeO_2 nanocubes. Although Pt-CeO_2 did not show any high intensity surface reduction peaks at <400 ^oC, it was still believed that Pt-CeO_2 nanocubes had a higher activity than pure CeO_2 nanocubes considering that the latter showed continuous reduction from room temperature all the way to 900 ^oC. We also conclusion that both Pt and Au CeO_2 nanocomposites had higher activity than pure CeO_2 nanocubes and that Au was a better catalyst on CeO_2 as compared to Pt due to the above discussed reasons [27].

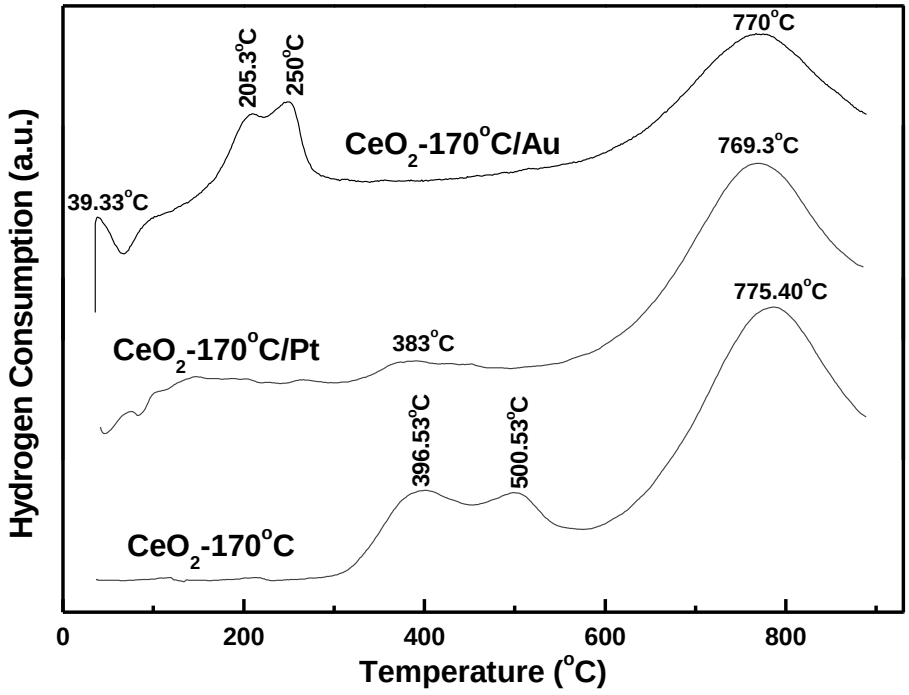

Figure 49: Comparison of pure ceria nanocubes with Pt-CeO_2 nanocubes and Au-CeO_2 nanocubes

5.4.2.2 The effect of using different noble metals on the same CeO_2 morphology

(i) Gold

Figure 15 below is a comparison of the catalytic activity of pure ceria nanorods and nanocubes with those of Au-impregnated nanorods and nanocubes. As far as low temperature reducibility of the materials is concerned, it is clear from the schematic that

the Au-impregnated nanorods and nanocubes performed better than pure ceria nanorods and nanocubes, with a deeper probe into the data showing that Au-CeO_2 nanorods had a higher reducibility at low temperature as compared to the Au-CeO_2 nanocubes. This was confirmed by the fact that the intensity and peak area of the reduction band that occurred at 166.89 ^oC were higher than those of the reduction band that occurred at 250 ^oC. This observation was attributed to the fact that CeO_2 nanorods could have had stronger interactions with Au nanoclusters compared to CeO_2 nanocubes, given that there was a higher probability of CeO_2 nanorods boding with Au nanoclusters along their diverse terminating crystallographic facets as was revealed by our HRTEM studies. Nevertheless, this conclusion should not overshadow the fact that Au-CeO_2 nanocubes showed a low intensity reduction band at 39.33^oC that was not witnessed in Au-CeO_2 nanorods, indicating that the Au-CeO_2 nanocubes could be useful in the catalytic oxidation of molecular hydrogen at less than 50 ^oC while Au-CeO_2 nanorods might not be fit for such an application [24-25, 27-28, 31].

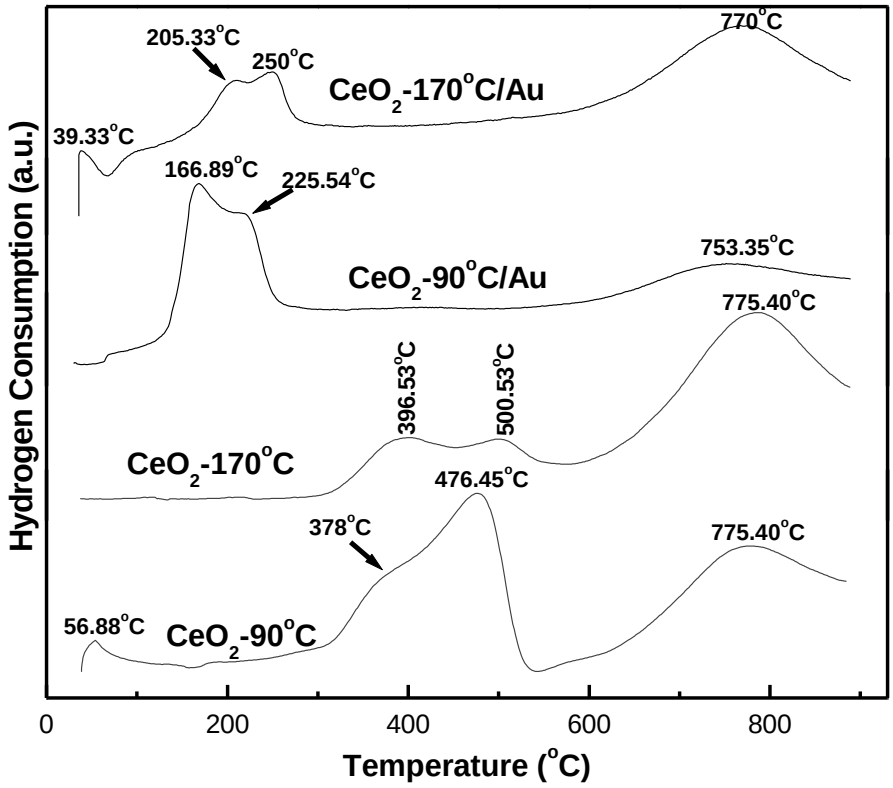

Figure 50: Comparison of pure CeO_2 with Au-impregnated CeO_2.

(ii) Platinum

Figure 16 below compares the catalytic activity of pure ceria nanorods and nanocubes with those of Pt-impregnated nanorods and nanocubes. According to the data, it can be said that the Pt-impregnated nanorods and nanocubes had better low temperature reducibility as compared to those of pure ceria nanorods and nanocubes. We arrived at this conclusion based on the fact that Pt-CeO_2 nanocubes showed unceasing and progressive reduction from room temperature all the way to 900 ^oC, a phenomenon that was not witnessed in the reduction CeO_2 while the Pt-CeO_2 nanorods showed two distinct surface reduction bands at lower temperatures compared to the surface reduction of pure CeO_2. Another observation that was noted from the data was that Pt-CeO_2 nanorods had a

higher reducibility at low temperature as compared to the Pt-CeO_2 nanocubes based on the fact that the intensity and peak area of the reduction bands that occurred at 69.94 ^oC and 350 ^oC were higher than those of the reduction band that occurred at 383 ^oC. As was mentioned above, we attributed this observation to the fact that CeO_2 nanorods could have had stronger interactions with Pt nanoclusters compared to CeO_2 nanocubes, given that there was a higher probability of CeO_2 nanorods boding with Pt nanoclusters along their diverse terminating crystallographic facets as was revealed by our HRTEM studies. Nevertheless, this conclusion should not overshadow the fact that Au-CeO_2 nanocubes showed a low intensity reduction band at 39.33 ^oC that was not witnessed in Au-CeO_2 nanorods, indicating that the Au-CeO_2 nanocubes could be useful in the catalytic oxidation of molecular hydrogen at less than 50 ^oC while Au-CeO_2 nanorods might not be fit for such an application [17, 26, 27-30].

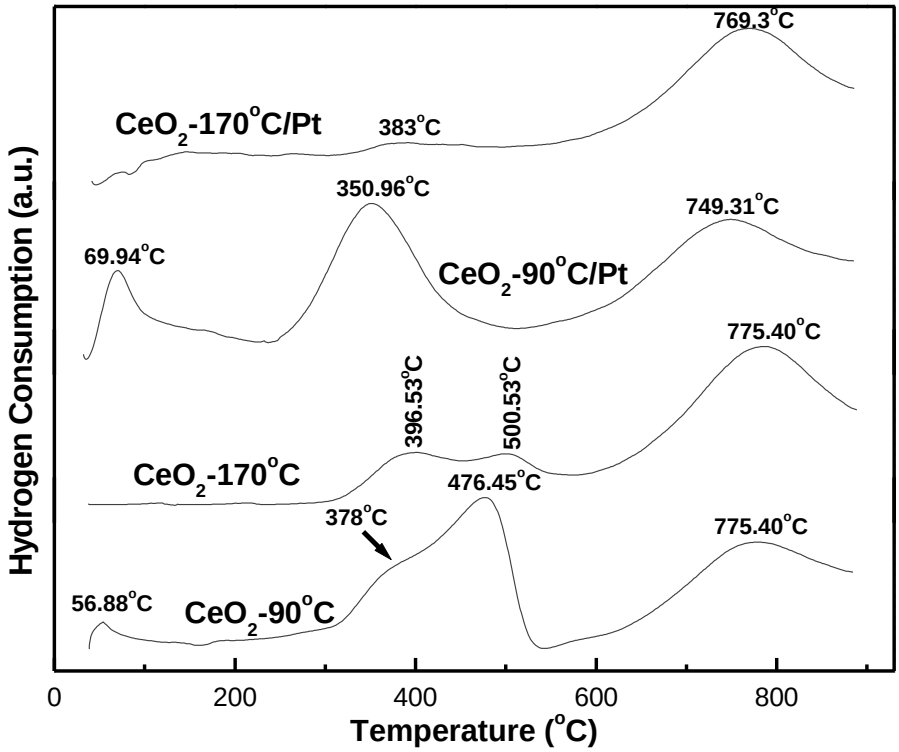

Figure 51: Comparison of pure CeO_2 with Pt-impregnated CeO_2.

5.4.2.3 Oxygen storage capacity measurements

Oxygen Storage Capacity (OSC) measurements were carried out using H_2-TPR peak area to mass ratio calculations as summarized in Table 2 and in Figures 17-19. A probe into the data revealed that both Au-impregnated CeO_2 nanorods and nanocubes had superior oxygen storage capacity compared to both Pt-impregnated CeO_2 nanorods and nanocubes. This observation was attributed to the possibility of Au nanocrystals interacting more strongly with CeO_2 nanocrystals compared to amorphous Pt, hence becoming more effective in the spillover mechanism where oxygen is believed to migrate from the surface of CeO_2 to the surface of the noble metal nanoparticles or where hydrogen could be transferred from the noble metal surface to the surface of CeO_2. It was

concluded that the purported stronger interactions between Au and CeO_2 nanocrystals originated from the nature of growth and orientation of the Au nanoclusters on the surface of CeO_2 nanocrystals especially when considering the fact that Au diffraction peaks were seen on our XRD profiles (as was discussed before) while the presence of crystalline Pt nanoclusters was not be confirmed from the same. This major difference in XRD data advocated for a possible epitaxial growth of Au nanocrystals on CeO_2 nanoparticles hence justifying why both could have has a stronger interaction compared to Pt-CeO_2 interactions. It was easy to conclude from our XRD data Pt was atomically dispersed on CeO_2 nanocrystals hence not being able to form any crystals that could have interacted epitaxially with CeO_2 nanocrystals, and therefore not being able to participate effectively in the spill over mechanism. On the other side, Pt and Au- impregnated nanorods proved to have higher oxygen storage capacity compared to Pt and Au-impregnated nanocubes. As was discussed before, this difference must have been due to the fact that nanorods had more crystallographic facets exposed on their surfaces e.g the {110}, {200}, {111} and {311} as compared to nanorods that has only {100} and {111} hence having more crystallographic defects that could help improve the strength of the noble metal-ceria surface interactions, and therefore promoting the extent of reducibility and hence the oxygen storage capacity of the materials (this is evident from Figures 17 & 18). Fig. 19 shows that the bulk or high temperature reducibility and the oxygen storage capacity of Pt and Au-impregnated nanorods and nanocubes is identical to that of pure CeO_2 nanorods and nanocubes as shown in the first two columns of Figure 17. This observation was consistent with the fact that the beneficial effect of Pt and Au nanoparticles of the reducibility and oxygen storage capacity of the materials is only

realized during surface reduction but is not useful in high temperature or bulk reduction processes [27, 31-32].

Table 5: A summary of Oxygen storage capacity measurements

Sample	Low temp. (<550°C) peak area/mass	High temp. (>550°C) peak area/mass	Total area/mass ratio	Ratio of Low:High Temp.
CeO_2 nanorods pure	26.54	23.83	50.37	1.11
CeO_2 nanocubes	27.16	45.43	72.59	0.6
1% Pt CeO_2 nanorods	30.72	34.64	65.36	0.89
1% Pt CeO_2 nanocubes	17.22	40.74	57.84	0.42
1% Au CeO_2 nanorods	92.28	77.72	170	1.19
1% Au CeO_2 nanocubes	77.16	81.23	158.5	0.95

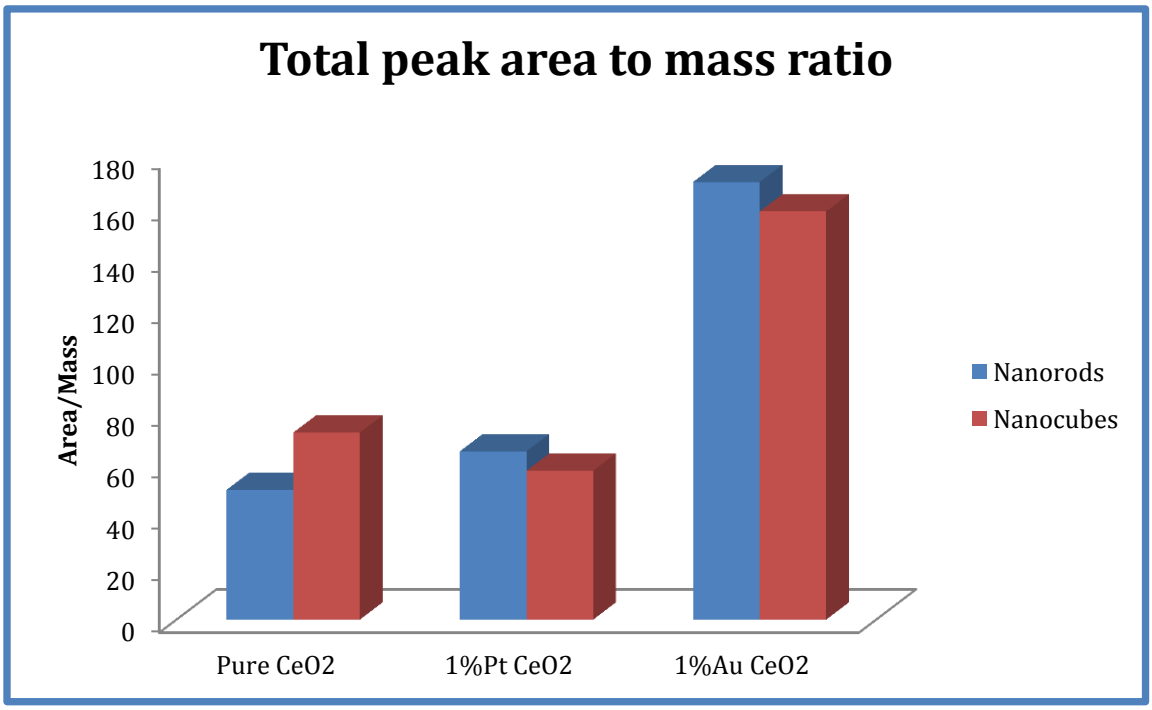

Figure 52: Total peak area to mass ratio.

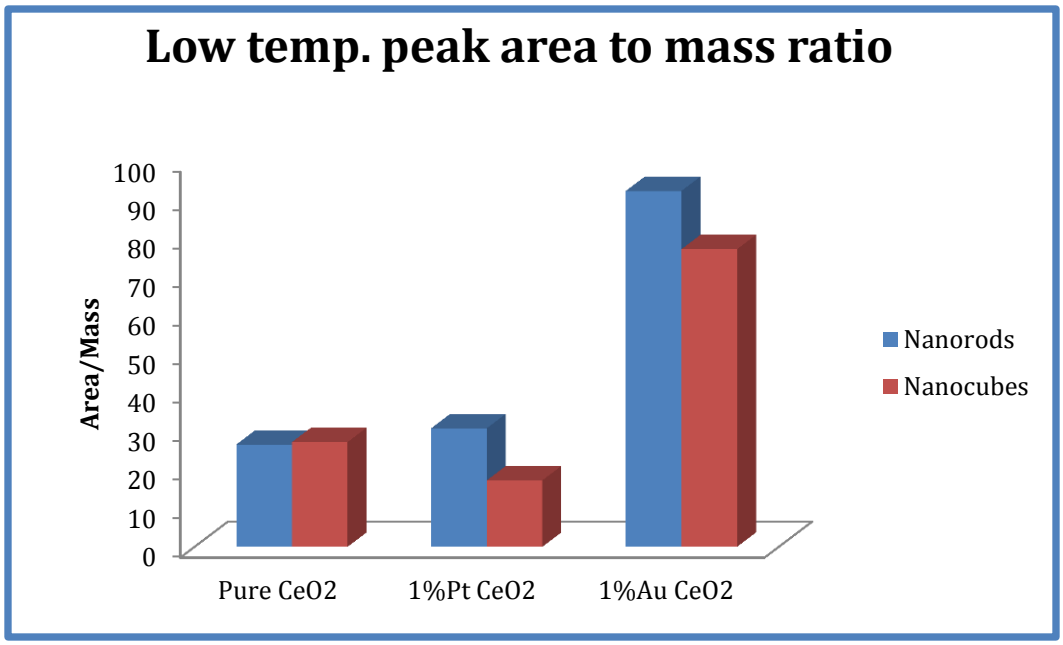

Figure 53: Low temperature peak area to mass ration

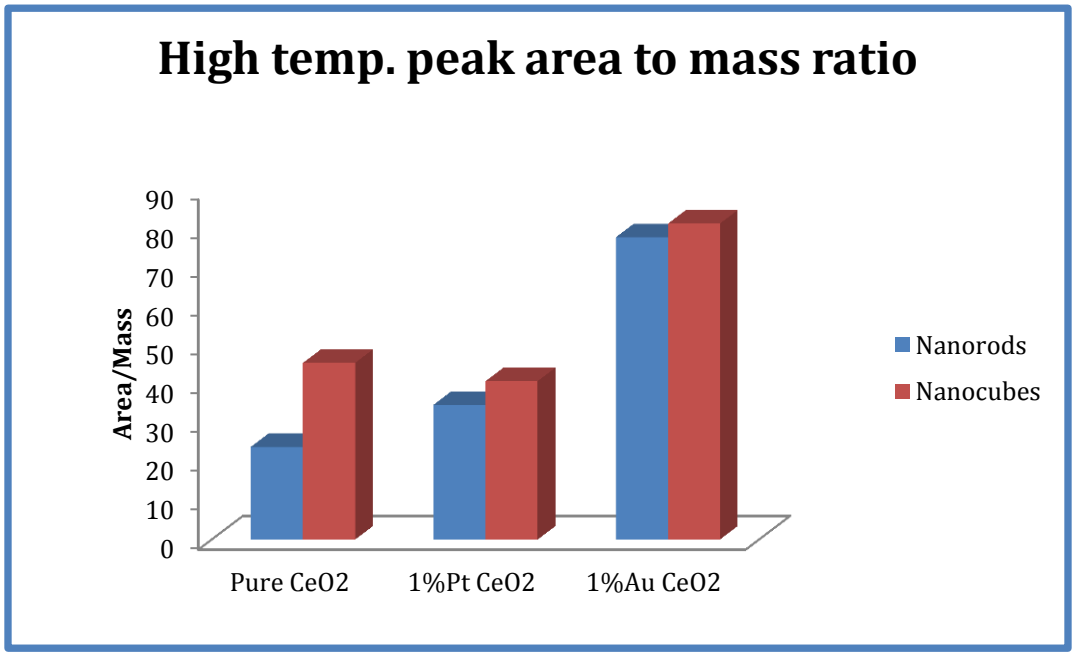

Figure 54: High temperature peak area to mass ratio

5.5 Conclusion

We have shown using Hydrogen-Temperature Programmed Reduction (H_2-TPR) studies that the impregnation of 1 wt. % platinum and gold on CeO_2 nanorods and on nanocubes causes an acute reduction on their surface reduction temperatures with negligible effect on their bulk reducibility. We have also shown that both pure and impregnated CeO_2 nanorods have a lower surface reduction temperature compared to that of pure and impregnated CeO_2 nanocubes and that the intensities of the low-temperature reduction bands of pure CeO_2 nanoparticles, and hence their low temperature reducibility, had a direct correlation to their BET-surface area. We have also demonstrated that gold nanoparticles proved to have a higher catalytic performance in oxidizing molecular hydrogen at low temperatures as compared to platinum nanoparticles.

5.6 References

1. Zhang, J et al., *Nano Lett*. **11**, 361 (2011)
2. Wenjuan, S, Hongjuan, G, Chang, L., Xiaonan, W., *J. Rare Earths.* **30**, [7] 665 (2012)
3. Hegde, M.S., Madras, G., Patil, K.C., *Accounts of Chem. Res*. **42**, [6] 707 (2009)
4. Jiang, L. et al., *CrysEngComm*. **15**, 3739 (2013)
5. Yang, Y., Jin, Y., He, H., Y,e Z., *CystEngComm*. **12**, 2663 (2010)
6. Deshpande, S., et al., *App. Phys. Letts*. **87**, 133133 (2005)
7. Mai, H.X., et al., *J. Phys. Chem*. B **109**, 24380 (2005)
8. Wu, L.et al., *Phys. Rev. B*. **69**, 125415 (2004)
9. Pan, C., Zhang, D., Shi, L., Fang, J., *Euro. J. Inorg. Chem*. **15**, 2429 (2008)
10. Ghosh, S. K., Pal, T., *Chem. Rev*. **107**, 4797 (2007)
11. Kominami, H., Tanaka, A., Hashimoto, K., *Chem. Comm*. **46**, 1287 (2010)
12. Clark, A., Zhu, A., Sun, K., Petty, H. R., *J. Nanopart Res*. **13**, 10, 5547 (2011)
13. Layek, K.et al., *Green Chem*. **13**, 2878 (2011)
14. Spanier, J. E. et al., *Physical Review B*. **64**, 245407 (2001)
15. Inguanta, R., Piazza, S., Sunseri, C., *J. Electrochem. Soc.* **159**, [8] D493 (2012)
16. Hamlaoui, Y. et al., *Mat. Chem & Phys*. **113**, 650 (2009)
17. Feng, L.et al., *Nano Rest.* **4**, (1) 61 (2011)
18. Godinho, M.et al., *J. Mater Sci*. **45**, 593 (2010)
19. Si, R., Stephanopoulos, M. F., *Angew. Chem. Int. Ed*. **47**, 2884 (2008)
20. Fronzi, M.et al., *J. Chem. Phys*. **131**, 104701 (2009)
21. Zhang, F.et al., *Appl. Phys. Lett*. **80**, (1) 127 (2002)

22. Mingjuan, S., Guojun, S., Shan, X., Xiaolai, W., *Chinese J. Catal*. **33**, (8) 1318 (2012)

23. Fu, Q., Weber, A., Stephanopoulos, M. F., *Catal. Lett.* **77**, (1-3) 87 (2001)

24. Kim, H. Y., Henkelman, G., *J. Phys. Lett*. **4**, 216 (2013)

25. Kim, H. Y., Lee, H. M., Henkelman, G., *J. Am. Chem. Soc*. **134**, 1560 (2012).

26. Monyanon, S.et al., *J. Power Sources* **163**, 547 (2006)

27. Yi, G., et al., *Chem. Phys. Letts*. **479**, 128 (2009)

28. Komai, S., Yazawa, Y., Satsuma, A., Hattori, T., J. *Jpn. Petrol. Inst*. **48**, 3 (2005)

29. Zhu, X., Hoang, T., Lobban, L. L., Mallinson, R. G., *Appl. Cat. B: Environ.* **94**, 311 (2010)

30. Acerbi, N. et al., *J. Phys. Chem. C*. 116, 13569 (2012)

31. Huang, P.X. et al., *J. Phys. Chem. B*. 109, 19169 (2005)

32. Skoda, M., Cabala, M., Matolinova, I., Veltruska, K., Matolin, V., *WDS`09 Proceedings of Contributed Papers*, Part III, 157 (2009)

Chapter 6 Conclusions and Future Work

It has been shown in this thesis report that synthesis temperature plays a critical role in controlling the shape, morphology, oxygen vacancy concentration and low temperature reducibility in CeO_2 nanoparticles. We have also seen that OH^- ion concentration can play an important role in engineering the lattice constants and oxygen vacancy concentrations of ceria nanoparticles within the same particle morphology and synthesis temperature. As far as we are concerned, the latter is a new finding that must be explored further in engineering defects in CeO_2 systems.

Secondly, we have shown that hydrothermal synthesis is a facile one-step approach to prepared compositionally homogeneous $Ce_xZr_{1-x}O_2$ ($0 \leq x \leq 1$) nanocrystals, in which CeO_2-ZrO_2 mixed oxides present a superior low-temperature oxygen release capability compared to pure CeO_2. The $Ce_{0.5}Zr_{0.5}O_2$ system proved to have good thermal stability up to 1000 ^oC under reducing and oxidizing atmosphere. We have also seen that at above 1000 ^oC, phase transformation occurs from psudocubic to cation ordered pyrochlore or tetragonal phase under reducing and oxidizing atmosphere, respectively. This method may be easily extended to other cerium-based mixed oxides or synthesis of analogous mixed oxides.

Lastly, we have demonstrated (by using Hydrogen-Temperature Programmed Reduction (H_2-TPR) studies) that the impregnation of 1 wt. % Platinum and Gold on CeO_2 nanorods and on nanocubes causes an acute reduction on their surface reduction temperatures with negligible effect on their bulk reducibility. We have also shown that both pure and impregnated CeO_2 nanorods have a lower surface reduction temperature compared to that of pure and impregnated CeO_2 nanocubes and that the intensities of the

low-temperature reduction bands of pure CeO_2 nanoparticles, and hence their low temperature reducibility, had a direct correlation to their BET-surface area. We have also demonstrated that Gold nanoparticles proved to have a higher catalytic performance in oxidizing molecular hydrogen at low temperatures as compared to Platinum nanoparticles.

More research needs to be done on pure cerium oxide crystal growth and nucleation so that there can be a full understanding of why morphology changes occur with chaging reaction conditions. Specifically, it would be of interest to understand why high sodium hydroxide concentrations favor the formation of ceria nanorods with least priority given to nanocubes. It would also be a good idea to correlate the different morphologies of ceria with therir electronic properties.

It would also be important to study more perform more studies on of $Ce_{1-x}Zr_xO_2$ systems and understand invent a way of controlling crystal morphology without having to lose crystallographic homogeneity as was seen in the $Ce_{0.3}Zr_{0.3}O_2$ that was synthesized without stirring. Understanding how the electronic structure of these systems varies with different doping concentrations would be worth studying further in the future.

The biggest challenge in heterogenous catalyst has been to undersand how noble metals interact with nanoceria support on a molecular lever. It would be therefore be important to perform high resolution TEM experiments on Pt and Au nanocomposites in order to determine how they interact with different crystal sizes and morphologies of cerium oxide.